Atmospheric Observations and Models of Greenhouse Gas Emissions in Urban Environments

Atmospheric Observations and Models of Greenhouse Gas Emissions in Urban Environments

A dissertation presented

by

Kathryn McKain

to

The School of Engineering and Applied Sciences

in partial fulfillment of the requirements

for the degree of

Doctor of Philosophy

in the subject of

Engineering Sciences

Harvard University

Cambridge, Massachusetts

May 2015

Dissertation Advisor: Steven C. Wofsy Kathryn McKain

Atmospheric Observations and Models of Greenhouse Gas Emissions in Urban Environments

Abstract

Greenhouse gas emission magnitudes, trends, and source contributions are highly uncertain, particularly at sub-national scales. As the world becomes increasingly urbanized, one potential strategy for reducing these uncertainties is to focus atmospheric greenhouse gas measurements in urban areas, where a multitude of emission processes occur, imposing a strong and persistent gradient in the local atmosphere, and contributing a significant fraction of global anthropogenic greenhouse gas emissions.

This thesis explores the capabilities and requirements for characterizing and quantifying greenhouse gas fluxes in urban environments using atmospheric measurements and models. The first chapter uses an existing dataset of atmospheric carbon dioxide measurements from Salt Lake City, Utah to assess the capacity of an atmospheric measurement and modeling framework to detect changes in emissions from a city in the context of an emissions verification framework. The results of this work are then used to explore an alternative or complementary measurement strategy of atmospheric column measurements for urban emissions detection, which would be less sensitive than point measurements to the large variability present in urban atmospheres, but would also have more stringent accuracy requirements.

The second chapter describes the development and maintenance of a network of greenhouse gas measurement stations in the Boston urban region, which has been continuously

running since 2012 and has generated high-quality atmospheric carbon dioxide and methane data that can be used to explore their fluxes across the urban region. The third chapter applies the Boston network data to investigate the magnitude of methane emissions from natural gas infrastructure in the urban region. We find that the natural gas loss rate in 2012-13 was 2.7 ± 0.6 %, two to three times larger than that reported by industry and government. Our findings suggest that natural gas consuming regions may be larger sources of methane than previously thought, and have implications for local and national policies that aim to reduce methane emissions and promote energy-use efficiency. The work presented in this thesis explores general methodological strategies for urban atmospheric measurements and models, and offers example applications of such methods to directed and societally-relevant investigations of urban greenhouse gas emissions.

Table of Contents

Acknowledgements

I am grateful to many people for their help, advice, and support throughout my graduate school experience. My advisor, Steve Wofsy, offered me unparalleled opportunities to learn and grow as an atmospheric scientist. Steve's energy and enthusiasm for research are infectious, and his fearlessness and innovation in science is inspirational. I am particularly grateful for his sustained interest in my work, excellent feedback throughout graduate school, and support of me pursuing my interests, even when they did not fit within the paradigm of the field or the traditional expectations of a graduate student. I am also grateful to him for always pushing me to stand up front.

I am indebted to Bruce Daube for sharing with me his philosophies on how to make robust high-quality greenhouse gas measurements, and for patiently answering my sometimes endless questions. I am especially indebted to John Budney whose sustained logistical support made the Boston network possible. Lucy Hutyra at Boston University offered a great deal of leadership on the topic of urban atmospheric research, from which I have benefited and learned. Thomas Nehrkorn and, the late, Janusz Eluszkiewicz at Atmospheric and Environmental research have been enthusiastic collaborators and made integral contributions to the modeling work presented in this thesis. The group of experts involved in the Environmental Defense Fund program to investigate methane emissions from natural gas, and the Climate Change Division staff at the Environmental Protection Agency, helped me understand the many nuances and complexities of the natural gas-methane issue.

The Earth and Planetary Sciences Department and atmospheric science communities at Harvard made me feel at home. In particular, I am grateful to my graduate student peers for

creating a challenging and exciting learning environment, offering advice on how to successfully get through graduate school, and for their camaraderie.

Finally, my greatest thanks go to my husband, Tom, for his unquestioning and limitless love and support; I could not ask for anything more.

Citations to Previously Published Work

Chapters 1 and 3 have previously appeared as the following papers:

McKain K, Wofsy SC, Nehrkorn T, Eluszkiewicz J, Ehleringer JR, Stephens BB (2012) Assessment of ground-based atmospheric observations for verification of greenhouse gas emissions from an urban region, Proceedings of the National Academy of Sciences of the United States of America, 109 (22), 8423-8428, doi: 10.1073/pnas.1116645109.

McKain K, Down A, Raciti SM, Budney J, Hutyra LR, Floerchinger C, Herndon SC, Nehrkorn T, Zahniser MS, Jackson RB, Phillips N, Wofsy SC (2015) Methane emissions from natural gas infrastructure and use in the urban region of Boston, Massachusetts, Proceedings of the National Academy of Sciences of the United States of America, 112 (7), 1941-1956, doi: 10.1073/pnas.1416261112.

Introduction

Atmospheric measurements of greenhouse gases have traditionally been made in remote locations in order to quantify and track changes in globally-representative mixing ratios and infer large-scale flux processes. There is increasing interest in applying atmospheric techniques to investigate questions of greenhouse gas fluxes at regional and local scales, such as in urban environments. This is because, converse to remote background measurements, regional and urban scale studies have the potential to offer new insights on the attribution of emissions to specific source types and processes, and to evaluate the efficacy of specific mitigation actions.

A great deal of progress has been made in this burgeoning area of research in recent years. Kort et al. (2013) used a modeling framework to explore the relative ability of different atmospheric observational network designs to constrain greenhouse gas fluxes in the Los Angeles basin. Breon et al. (2015) assessed the capability of an atmospheric observation-modeling framework to constrain carbon dioxide (CO_2) emissions in Paris and found that an emission inventory for the region was significantly overestimated. Mays et al. (2009) and Cambaliza et al. (2015) used an aircraft mass-balance approach to estimate methane (CH_4) emissions and the relative contribution of different source types in Indianapolis. Lauvaux et al. (2013) made atmospheric greenhouse gas measurements in Davos during the World Economic Forum in 2012 and showed that emissions dropped by ~35% due to traffic bans during the meeting. Kort et al. (2012) demonstrated the capability of satellite measurements to detect column-integrated CO_2 enhancements over urban areas and quantitatively estimated the change in emissions that could be detected, using GOSAT observations over Los Angeles and Mumbai as examples.

Beyond emissions quantification and characterization, urban greenhouse gas measurements and models could also be used in public health studies of human exposure to primary pollutants at higher space and time resolutions through their coupling with combustion CO_2 emissions. Another exciting application will be to assess the capability of the recently-launched OCO2 satellite to detect gradients in CO_2 column abundances created by urban emissions through direct comparison of ground-based and OCO2 column observations of specific cities. This information will be especially valuable for translating the insight we gain through intense study of a handful of cities to other cities in developing countries where emissions are rapidly changing and highly uncertain, but where ground-based observational capabilities are limited.

This thesis explores methodological requirements, and potential capabilities and applications, in the growing research area of urban atmospheric greenhouse gas measurements and models for flux characterization and quantification. Early motivation for this work derived from a 2010 National Research Council (NRC) report which recommended extending the atmospheric greenhouse gas sampling network to a representative sample of cities as one strategy, among others, to independently verify self-reported emissions in the context of a global climate treaty.

Chapter One characterizes atmospheric CO_2 levels in an urban environment using an existing dataset of surface observations from Salt Lake City. In this work, we tested the concept proposed by the NRC (2010) report that continuous, longterm, urban atmospheric measurements could be used to verify reported emissions and track changes in emissions within a quantified uncertainty level, depending on the capability of atmospheric transport models to reproduce urban observations. Based on the findings of this pilot project in Salt Lake City, we proposed

that measurements of the column-integrated enhancements of greenhouse gases in urban environments are a promising complementary or alternative strategy to ground-based point observations because they are insensitive to small-scale emission and atmospheric circulation processes, although the accuracy requirements would be more demanding.

Chapter Two describes the measurement network that we set up to measure CO_2 and CH_4 in the atmosphere of the Boston urban region, which has been running continuously since 2012. We describe the measurement methods and strategy to promote robust, reliable, remote operation, and lessons learned from running the network. We explore measurement error and describe general features of the resulting dataset.

Chapter Three uses the Boston network data, and a comprehensive modeling framework, to quantify the flux of CH_4, specifically from natural gas, in the urban region over one year. We find that CH_4 emissions from natural gas are two to three times higher than expected based on industry and government reporting, and we propose several possible reasons for this finding. This chapter is an example of the potential use of urban atmospheric greenhouse gas observations to investigate currently unconstrained emission magnitudes and processes from multiple scientifically and societally-relevant perspectives.

References

Breon FM, Broquet G, Puygrenier V, Chevallier F, Xueref-Remy I, Ramonet M, Dieudonne E, Lopez M, Schmidt M, Perrussel O, Ciais P (2015) An attempt at estimating Paris area CO_2 emissions from atmospheric concentration measurements, Atmospheric Chemistry and Physics, 15: 1707 – 1724.

Cambaliza MOL, Shepson PB, Bogner J, Caulton DR, Stirm B, Sweeney C, Montzka SA, Gurney KR, Spokas K, Salmon OE, Lavoie TN, Hendricks A, Mays K, Turnbull J, Miller BR, Lauvaux T, Davis K, Karion A, Moser B, Miller C, Obermeyer C, Whetstone J, Prasad K, Miles N, Richardson, Elementa, 3: 37.

Committee on Methods for Estimating Greenhouse Gas Emissions (2010) Verifying greenhouse gas emissions: methods to support international climate agreements, National Research Council, National Academy Press, Washington, DC.

Kort EA, Frankenberg C, Miller CI, Oda T (2012) Space-based observations of megacity carbon dioxide, Geophysical Research Letters, 39: L17806.

Kort EA, Angevine WM, Duren R, Miller CE (2013) Surface observations for monitoring urban fossil fuel CO_2 emissions: Minimum site location requirements for the Los Angeles megacity, Journal of Geophysical Research: Atmospheres, 118: 1-8.

Lauvaux T, Miles NL, Richardson SJ, Deng A, Stauffer DR, Davis KJ (2013) Urban emissions of CO_2 from Davis, Switzerland: The first real-time monitoring system using an atmospheric inversion technique, Journal of Applied Meteorology and Climatology, 52: 2654-2668.

Mays KL, Shepson PB, Stirm BH, Karion A, Sweeney C, Gurney KR (2009) Aircraft-based measurements of the carbon footprint of Indianapolis, Environmental Science and Technology, 43: 7816-7823.

Chapter 1

Assessment of ground-based atmospheric observations for verification of greenhouse gas emissions from an urban region

Abstract

International agreements to limit greenhouse gas emissions require verification to ensure that they are effective and fair. Verification based on direct observation of atmospheric greenhouse gas concentrations will be necessary to demonstrate that estimated emission reductions have been actualized in the atmosphere. Here we assess the capability of ground-based observations and a high-resolution (1.3 km) mesoscale atmospheric transport model to determine a change in greenhouse gas emissions over time from a metropolitan region. We test the method with observations from a network of CO_2 surface monitors in Salt Lake City, Utah, USA. Many features of the CO_2 data were simulated with excellent fidelity, although data-model mismatches occurred on hourly time scales due to inadequate simulation of shallow circulations and the precise timing of boundary layer stratification and destratification. Using two optimization procedures, monthly regional fluxes were constrained to sufficient precision to detect an increase or decrease in emissions of approximately 15% at the 95% confidence level. We argue that integrated column measurements of the urban dome of CO_2 from the ground and/or space are less sensitive than surface point measurements to the redistribution of emitted CO_2 by small-scale processes and thus may allow for more precise trend detection of emissions from urban regions.

Introduction

Agreements to limit anthropogenic greenhouse gas (GHG) emissions will have major economic and political consequences. Compliance will be demonstrated primarily with self-reported emission inventories derived from activity data and generalized conversion factors (Eggleston et al. 2006, NRC 2010), but associated uncertainties may exceed the magnitude of emission reduction targets (NRC 2010, Gregg et al. 2008, Peylin et al. 2011, Marland 2008). Therefore, measurement, reporting, and verification (MRV) will be critical elements of any international climate treaty, as emphasized by a recent National Research Council (NRC) report (2010), a related study by the JASON scientific advisory group (2011), and by the Intergovernmental Panel on Climate Change (Eggleston et al. 2006). Verification procedures based on direct atmospheric observations can provide independent constraints on reported emissions and are necessary to ensure that emission reductions are actualized in the atmosphere.

The NRC report on MRV (2010) highlighted the potential utility of atmospheric observations and models for detecting trends in emissions from strong localized source regions, such as urban areas, where enhancements in GHG concentrations are readily detectable in the atmosphere. A large fraction of a country's emissions likely emanate from such regions and results from several representative cities over time could provide strong tests of claimed emission reductions at national or regional scales. But the NRC (2010) estimated that current uncertainties in this approach exceed 100%, far too large to detect emission changes mandated by treaties or national policies. This imprecision is attributable to a dearth of research on the concept and the committee (2010) speculated that near-term efforts could lead to substantial improvements, perhaps allowing for the detection of a change in emissions of 10-25% in 1 year and of 10% or less over 10 years.

The present study addresses the problem posed by the NRC (2010) by assessing the current capability for using atmospheric observations to determine trends in GHG emissions at the scale of an urban region. We develop a high-resolution, urban-scale, observation-model framework, whereby observed GHG concentrations and presumed emissions are quantitatively related with an atmospheric transport and dispersion model (ATDM), and regional surface fluxes are estimated via an optimization procedure (Ciais et al. 2010). Input data consist of measurements that define atmospheric concentration enhancements relative to air advected from outside the source region, plus an emissions inventory that prescribes the presumed spatial and temporal distributions of surface fluxes.

We apply the observation-model framework to a test case of Salt Lake City (SLC), Utah, leveraging a unique, long term, publicly available dataset of urban atmospheric carbon dioxide (CO_2) concentrations (http://co2.utah.edu). We quantify the precision of the method for detecting changes in monthly emissions from this urban region, and assess how statistical properties of urban CO_2 concentrations and features of current state-of-the-art models limit trend detection capabilities. Finally, we suggest how the framework might be improved, through both alternative measurement strategies and enhanced model capabilities.

Previous studies of urban CO_2

Many studies (e.g. McRae and Graedel 1979, Bergeron and Strachan 2011, Gratani and Varone 2005) have described near-surface CO_2 concentrations and fluxes in a variety of urban environments and attributed observed variability to both atmospheric dynamics and local emission patterns. City-scale fluxes have been derived with mass-balance approaches using surface data from Krakow, Poland (Zimnoch et al. 2011) and aircraft data from Indianapolis, Indiana, USA (Mays et al. 2011). Ratios of carbon monoxide (CO) and CO_2 from a site near

Beijing, China were used to define trends in combustion efficiency (Wang et al. 2010). None of the approaches taken in these studies are capable of quantifying trends in emissions at the full urban scale and with the accuracy required for verification.

Levin et al. (2011) presented the only prior study to accurately assess emission inventories over time at a regional scale, using a multi-decadal dataset of atmospheric GHG concentrations, $^{14}CO_2$, and radon-222 from Heidelberg, Germany. Unfortunately, the key element of this unique study—long term, high frequency radioisotope measurements—are not currently widely reproducible due to cost and technological requirements. The framework described in the present study uses measurements made by readily available sensors combined with open-source meteorological data and models, and is thus scalable to numerous locations, as needed for MRV.

The SLC CO_2 measurement program was initiated as part of a study of carbon and oxygen isotopes focused on urban source attribution. Pataki et al. (2003, 2006, 2007) estimated the proportional contributions of natural gas versus gasoline combustion and biological respiration to observed CO_2 enhancements, and (2005) suggested the application of CO_2 as a tracer of atmospheric transport and mixing in complex terrain. Pataki et al. (2009) found general agreement between SLC eddy-flux measurements and an emissions inventory compiled for the sampled area. SLC CO_2 was simulated with a multiple box model to understand the relative contributions of meteorology and anthropogenic and biological surface fluxes to observed daily and seasonal cycles (Strong et al. 2011).

Methods

Observations

A network of CO_2 measurement sites has been operated at up to five locations in SLC and its suburbs (Figure 1-1, Table 1-1) since 2001. We modeled CO_2 data from 2006 because of the quality and consistency of the data from that year. For this study, we focused on modeling observations from the downtown, neighborhood, and junior high sites (Figure 1-1, Table 1-1). Two-day moving averaged CO_2 concentrations (Figure 1-2) from the Hidden Peak (HDP) mountaintop site (http://raccoon.ucar.edu) at the Snowbird Ski Resort outside SLC were used to represent the background CO_2 concentration in air coming in to the city.

Data from the continuous HDP continuous site and a flask sampling site in Wendover, UT (Conway et al. 2009) were both considered for representing background concentrations. Although the upwind location of Wendover (Figure 1-1) is more favorable for retrieving a background CO_2 concentration for SLC, the low frequency of the collection interval there made this dataset inadequate. Comparison of HDP and Wendover data (Figure 1-2) indicates that the HDP observations provide a reasonable representation of the background as they generally occur within the envelope of the Wendover observations. Although hourly to daily variations at HDP sometimes reflect local vegetative fluxes and nearby urban emissions, synoptic variations at HDP are well aligned with Wendover observations (Figure 1-2) and thus likely reflect variability in the background.

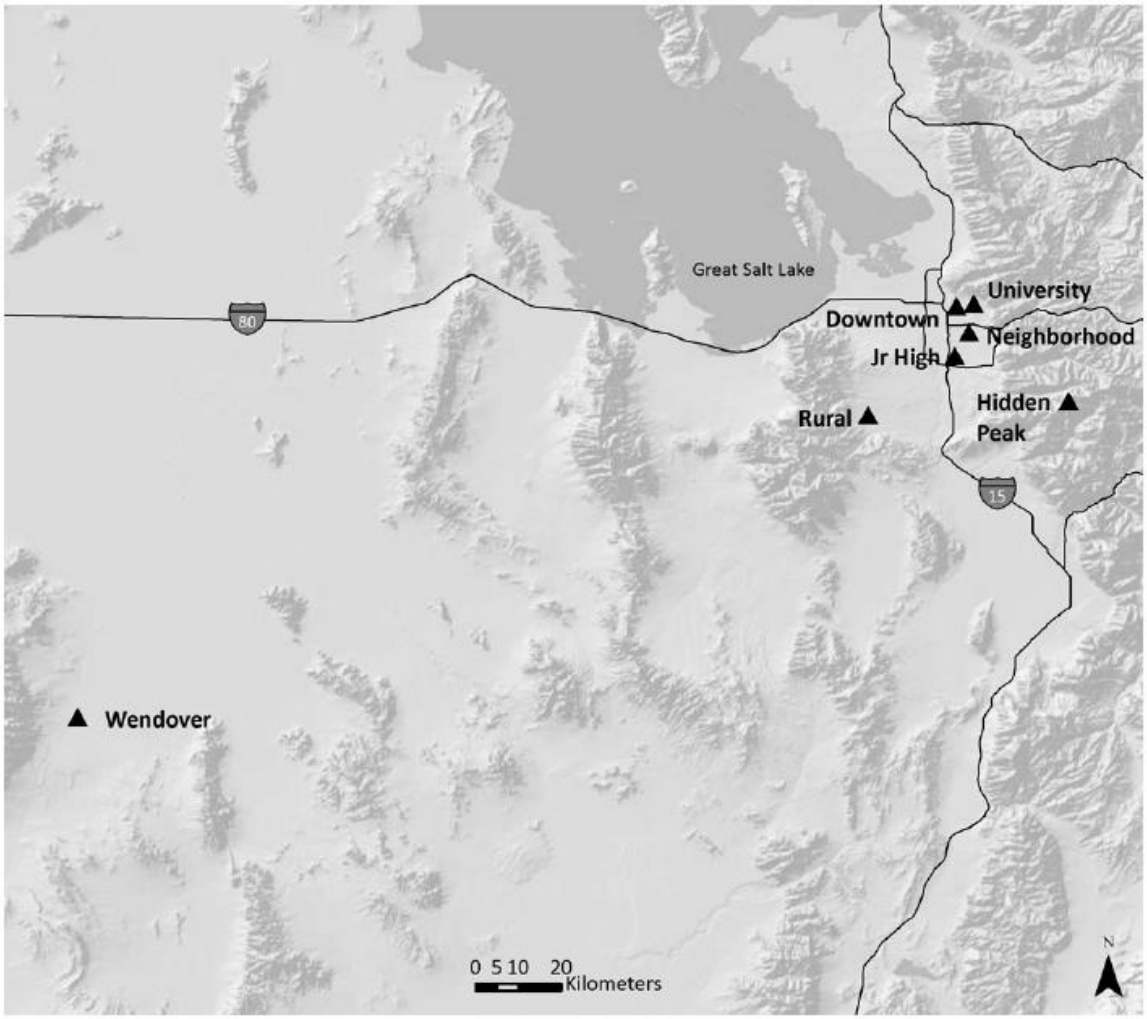

Figure 1-1. Map of Salt Lake City and background CO_2 measurement sites.

Table 1-1. Position of the five urban and two background CO_2 measurement sites in and around SLC in 2006.

Site	**Latitude, º**	**Longitude, º**	**Height above ground, m**	**Height above sea level, m**
University	40.763	-111.848	18	1,430
Downtown	40.758	-111.885	10	1,320
Residential	40.740	-111.858	4	1,339
Junior High	40.654	-111.888	10	1,325
Rural	40.530	-112.069	5	1,580
Snowbird	40.56	-111.65	17.7	3,350
Wendover	39.90	-113.72	0	1,320

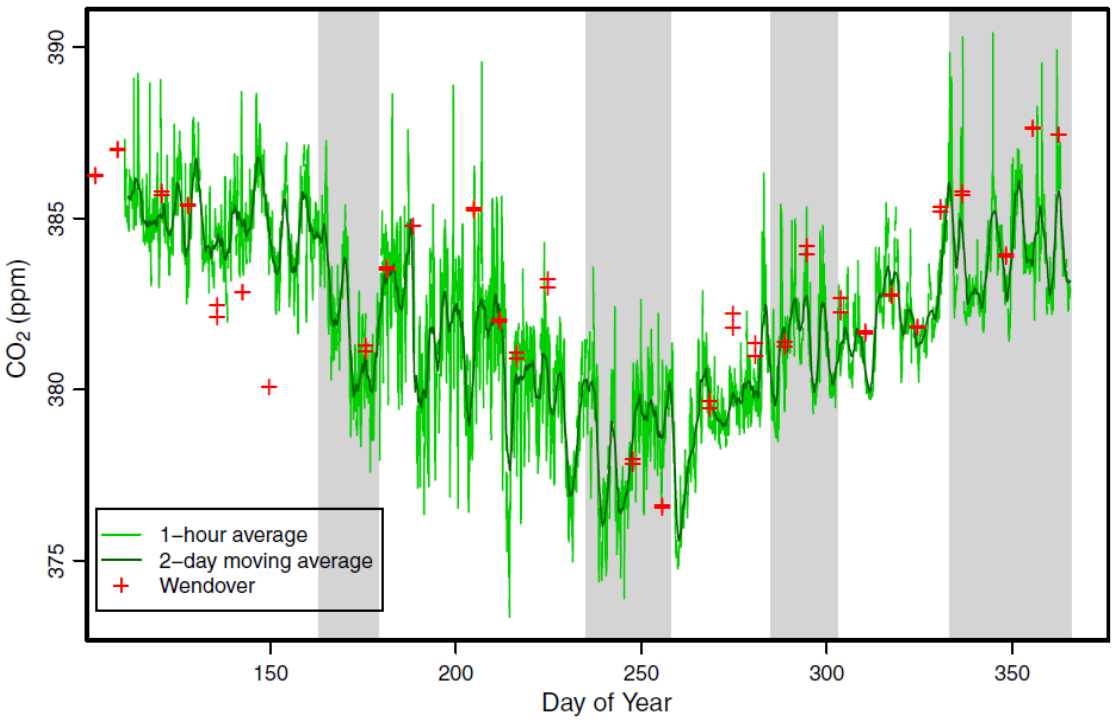

Figure 1-2. Background CO_2 concentrations to SLC in 2006. Hourly and 2-day moving averages from HDP and point measurements from Wendover, UT are shown. Modeled time periods are shaded in gray. Note that although the range of hourly concentrations at HDP sometimes exceeded that from Wendover, synoptic variations were largely consistent with the Wendover observations and thus likely reflected variations in incoming, background air. Two-day moving averaged data was utilized in the modeling framework to represent the advected background concentration.

CO_2 flux fields

The Vulcan database (v2.0) (Gurney et al. 2007, http://vulcan.project.asu.edu) was used for an anthropogenic CO_2 emissions field. Vulcan provides estimates of CO_2 emissions due to fossil fuel combustion from each of eight economic sectors for the U.S. in 2002 as a gridded product with a time and space resolution of one hour and 0.1^0, respectively. According to Vulcan, the major anthropogenic CO_2 sources in the Salt Lake Valley (SLV) are from the transportation, residential, and industrial sectors (Figure 1-3). To minimize the inclusion of year-specific emissions information while still retaining hour-of-the-day and day-of-the-week signatures, we averaged the Vulcan database by month, day-of-week, and hour-of-the-day

(Figure 1-3) prior to integrating it into the modeling framework. It was not necessary to scale the inventory to 2006, the year of interest for our study, because the observation-model framework is intended to determine a change in emissions over time, but not to evaluate absolute emissions from any single time period.

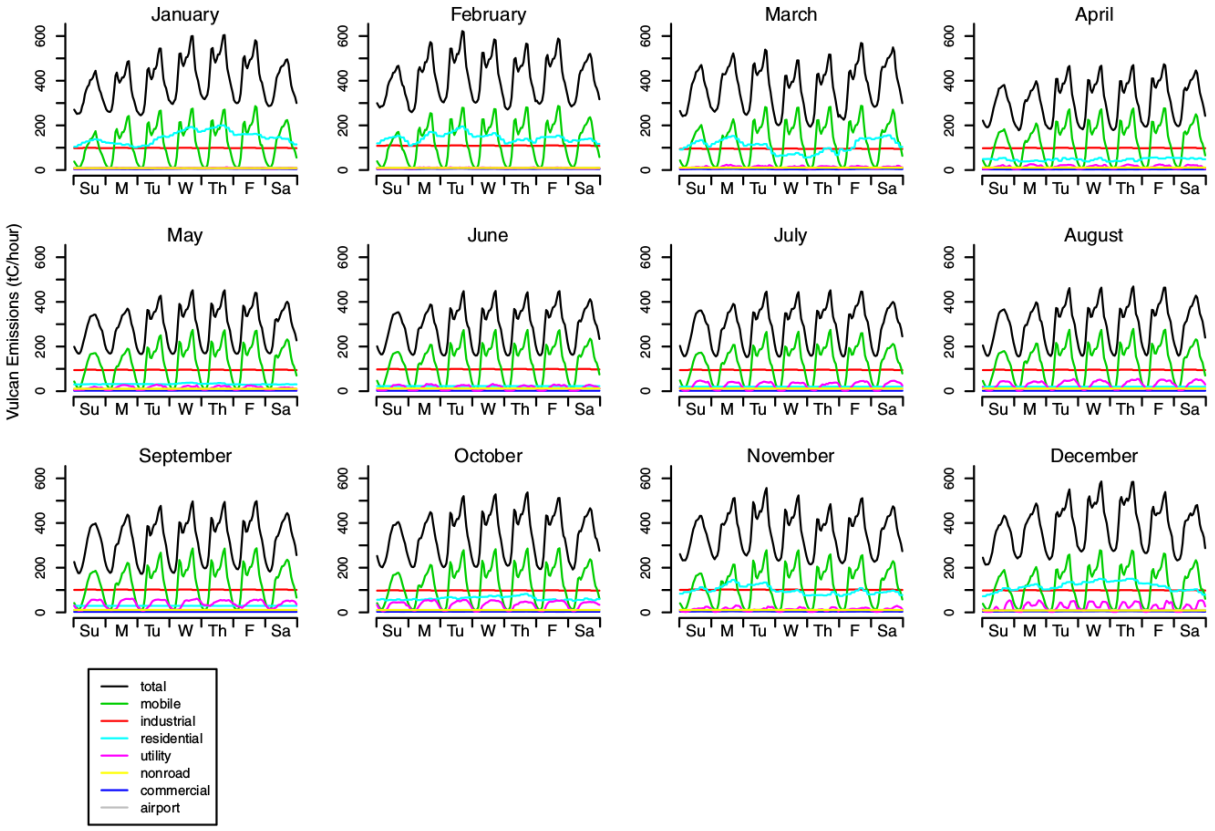

Figure 1-3. Vulcan emissions by sector for a 0.5° × 0.5° area centered on the Salt Lake Valley, averaged by hour, day-of-week, and month.

To represent CO_2 fluxes due to photosynthetic uptake and soil and plant respiration, we constructed a simple biosphere model using an approach similar to those presented in Gerbig et al. 2003 and Matross et al. 2006. The biosphere model had three major components: (i) CO_2 exchange data from eddy-covariance sites in the Ameriflux network (Baldocchi et al. 2001; http://public.ornl.gov/ameriflux) were used to create a key of flux parameters for relevant

vegetation types; (ii) a satellite-derived map of land-cover types (Homer et al. 2004) determined the spatial extent of vegetation types; and (iii) light and temperature data output by the assimilated meteorological fields in the atmospheric transport and dispersion model were used to drive the biosphere model.

Five eddy-flux sites (Baldocchi et al. 2001) were chosen to calibrate the biosphere model based on their representation of ecosystems which are most similar to those in and around SLC (Table 1-2). Net ecosystem exchange (NEE) data from each site in 2006 was partitioned into two functional components (Equation 1-1), which were each modeled separately. Gross ecosystem exchange (GEE) is a light-dependent term that represents photosynthesis (Equation 1-2) where SWR is solar radiation and g_0-g_2 are the fit model parameters. Ecosystem respiration (R) is a temperature-dependent term (Equation 1-3) and includes both heterotrophic and autotrophic respiration, where T is the air temperature and r_0 and r_1 are the model parameters.

$$\mathrm{NEE} = \mathrm{GEE} + \mathrm{R} \tag{1-1}$$

$$\mathrm{GEE} = g_0 + \frac{g_1 \cdot \mathrm{SWR}}{g_2 + \mathrm{SWR}} \tag{1-2}$$

$$\mathrm{R} = r_0 + r_1 \cdot \mathrm{T} \tag{1-3}$$

All eddy-flux data were filtered by friction velocity to eliminate unrepresentative observations. A minimum temperature (T_{min}) was chosen for each site so that if the air temperature was less than T min it was set to T min to prevent modeled respiratory fluxes from becoming negative at low temperatures. (Functionally, T_{min} accounts for the persistence of soil respiration even at very low temperatures when vegetation is dormant.) Positive GEE values resulting from curves with steep slopes at low-light levels were disregarded. Model parameters were fit for windows of time of varying lengths to maximize the fidelity of model fits at each site

and to capture within-season differences. Here temporal variability in biospheric CO_2 exchange was obtained from the eddy-flux sites, but, in practice, an alternative approach would be to use a satellite-derived vegetation greenness index for the study region (Mahadevan et al. 2008).

The 2001 National Landcover Database (v1) (Homer et al. 2004), a Landsat product that categorizes the United States into 16 land-cover classes and gives percent canopy at a 30-m resolution, was used to represent the spatial distribution of vegetation types. NEE was calculated using sunlight and temperature information output by the atmospheric transport model (discussed in the next section) and the flux parameters for the surrounding vegetation type and time of year. Land-cover types were retrieved for a 33 × 33 cell (ca. 1 km^2) area centered on each particle's location. NEE values for land-cover types associated with Niwot Ridge, Tonzi Ranch, and Harvard Forest were weighted by the percent canopy relative to that of the calibration site (Table 1-2). This approach was particularly important for the city where trees occur at a lower density than at the calibration sites.

Table 1-2. Ameriflux sites chosen to calibrate the biosphere flux model for the 16 land-cover types in the National Landcover Database (NLCD).

Ameriflux site	**Land cover type**	**Dominant species**	**Canopy cover, %***
Niwot Ridge, CO	evergreen forest	subalpine fir, Engelmann spruce, lodgepole pine	67
Tonzi Ranch, CA	deciduous forest, mixed forest	blue oak, annual C3 grasses	33
Corral Pocket, UT	shrub/scrub, grassland	perennial bunch grasses	0.2
Mead rainfed, NE	cultivated crops, pasture/hay	corn/soy rotation	0.1
Harvard Forest, MA	urban, woody wetlands	red oak, red maple, birch, eastern hemlock, white pine	91

*Mean canopy cover is given for a 33 × 33 pixel area around each site in the NLCD. No Ameriflux site was used to represent open water, barren, and herbaceous wetland land cover types and hence no vegetative fluxes were modeled where those types occurred.

Atmospheric transport model

The Stochastic Time-Inverted Lagrangian Transport (STILT) model (Lin et al. 2003) was used as the ATDM. STILT links the local concentration $C(x_r, t_r)$ of a conserved tracer, measured at the observation ("receptor") point (x_r) at time (t_r), to the sources S of the tracer emitted at upstream locations x at prior time t, by computing the influence function $I(x_r, t_r \mid x, t)$,

$$C(\mathbf{x}_r, t_r) = \int_{t_0}^{t_r} dt \int_V d^3x I(\mathbf{x}_r, t_r \mid \mathbf{x}, t) S(x,t) + \int_V d^3x I(\mathbf{x}_r, t_r \mid \mathbf{x}, t_0) C(\mathbf{x}, t_0) \qquad (1\text{–}4)$$

The first term in Equation 1-4 represents the concentration enhancement at the receptor due to sources sampled in domain V between times t_0 and t_r. The second term in Equation 1-4 is the advected lateral boundary condition. STILT simulates upstream influences on receptors by generating "footprints," which represents the sensitivity of each receptor to upwind surface emissions in units of ppm$/(\mu mol\ m^{-2}\ s^{-1})$ (Figure 1-4A).

We ran STILT in time-reversed mode such that an ensemble of air parcels ("particles") was transported back in time for up to six days from each receptor. STILT-generated footprints were convolved with the Vulcan emissions and biosphere flux fields to generate a set of predicted concentration enhancements above background at each observation site (Figure 1-4B). We found that run length (i.e., the number of hours backward in time) and particle number had very little effect on the results, so results reported in this paper are for 100-particle, 36-hour runs.

The STILT model was driven with customized meteorological fields from the advanced research version of the Weather Research and Forecasting (WRF v3.2) model (Skamarock and Klemp 2008, Nehrkorn et al 2010). Meteorological fields were generated at three gridded resolutions (4, 12, and 36 km) in a nested arrangement centered on SLC (Figure 1-5) for four approximately monthly time periods (Table 1-3). A set of "high-resolution" (1.3 km for the inner

nest) WRF (v3.2.1) fields with an urban canopy model (UCM) parameterization (Chen et al. 2010) were generated for a two-week subsample of the October, 2006 time period.

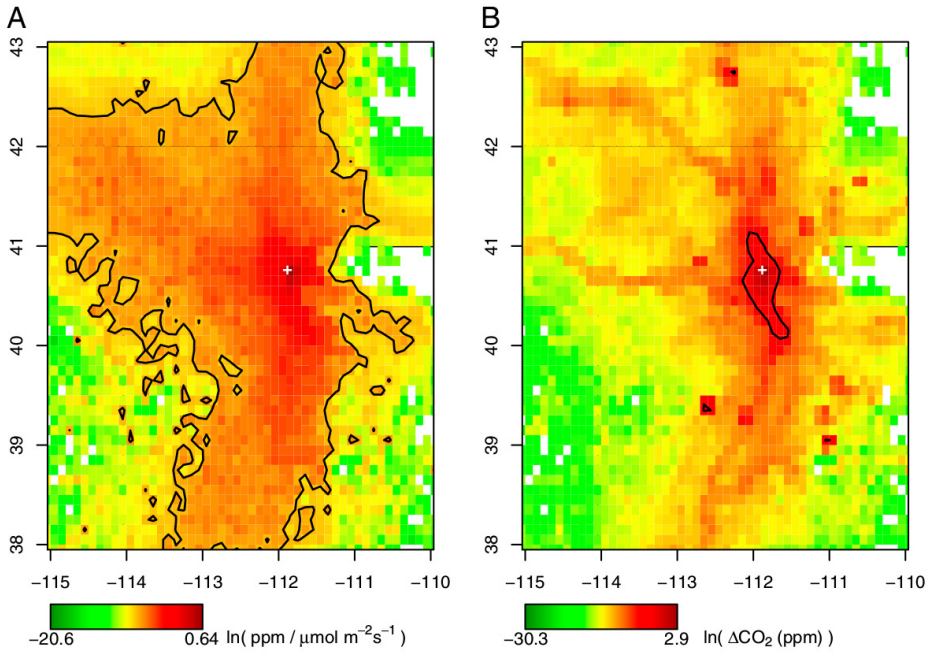

Figure 1-4. Spatial distribution around SLC of the simulated, logarithmic, average hourly (A) influence footprint and (B) CO_2 enhancement at the downtown site (white cross) for two weeks in October 2006. Contours enclose the areas responsible for (A) 90% of the total average footprint and (B) 99% of the total average CO_2 enhancement. Note that the area contributing the majority of the simulated CO_2 enhancement is much smaller than the influence region because of the compact nature of the urban source. Also note that the measurement site is on average sensitive to the entire city and broader metropolitan region.

Table 1-3. Means and standard deviations (1σ) of hourly observed and baseline modeled CO_2 (ppm) at the downtown site for the four simulated time periods from 2006.

Time Period	**Sample Size**	**Mean (SD)**	
		Observed	**Modeled**
June 13 – 27	334	397 (14)	391 (13)
Aug 23 – Sep 14	545	395 (17)	393 (19)
Oct 10 – 29	461	422 (34)	405 (26)
Nov 29 – Dec 31	785	439 (47)	429 (46)

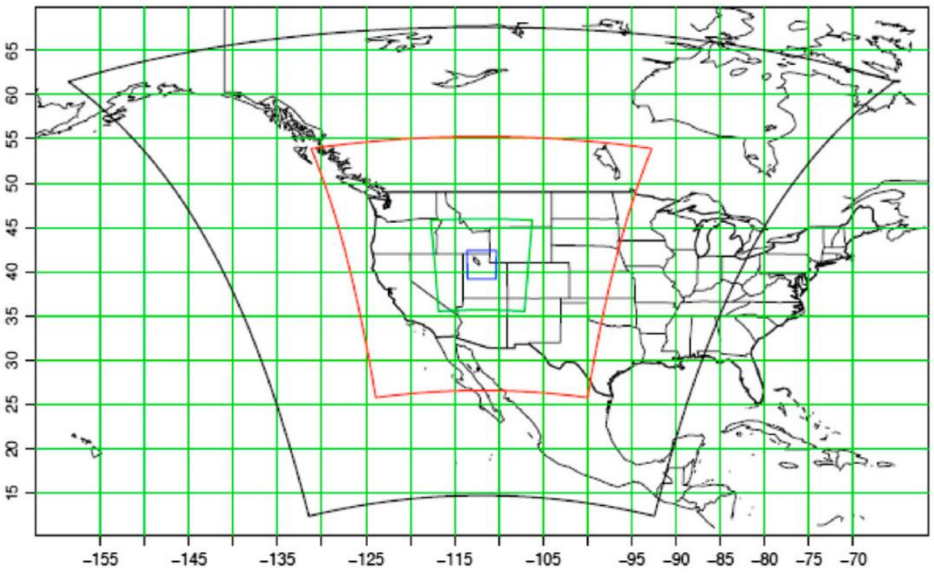

Figure 1-5. Position of the four nested Weather Research and Forecasting domains. The horizontal resolutions of the largest to smallest domains are 36, 12, 4, and 1.3 km, respectively. The inner nest was implemented for the "high-resolution" run only.

Characterization of CO_2 observations from Salt Lake City

The SLC CO_2 data follow a distinctive diel pattern, in which concentrations are higher at night and lower during the day (Figure 1-6A), following the daily cycle of the mixing height, which is shallow at night due to thermal stratification, and deep most days due to solar heating of the surface. The diel cycle of CO_2 concentrations is notably out of phase with emissions (Figure 1-6B), implying that thermally forced circulations impose a stronger influence on near-surface concentrations than emission rates (Strong et al. 2011). Mean hourly enhancements over background in 2006 at the downtown site ranged from ~0-20 ppm ($1\sigma \cong 16$ ppm) in the afternoon (12-18 hr MST) and from ~20-60 ppm ($1\sigma \cong 35$ ppm) at night (22-04 hr MST). Peak concentrations are typically observed in the early morning due to the combined effects of atmospheric stratification and increased emissions from rush-hour traffic; concentrations drop

rapidly thereafter with the onset of deeper vertical mixing in mid-morning (Figure 1-6A) (Strong et al. 2011).

Seasonal averages are lower in summer than winter (Figure 1-6A). During the growing season, CO_2 concentrations sometimes fall below background in the afternoon, likely due to uptake by urban trees (Ramamurthy and Pardyjak 2011). In the winter, the SLV is prone to atmospheric temperature inversions, which suppress vertical mixing and give rise to sustained periods of elevated concentrations. The overall distribution of observed CO_2 is heavily right-skewed (Figure 1-6C) and is seemingly comprised of two sub-populations, representing stratified and unstratified conditions (Figure 1-6D).

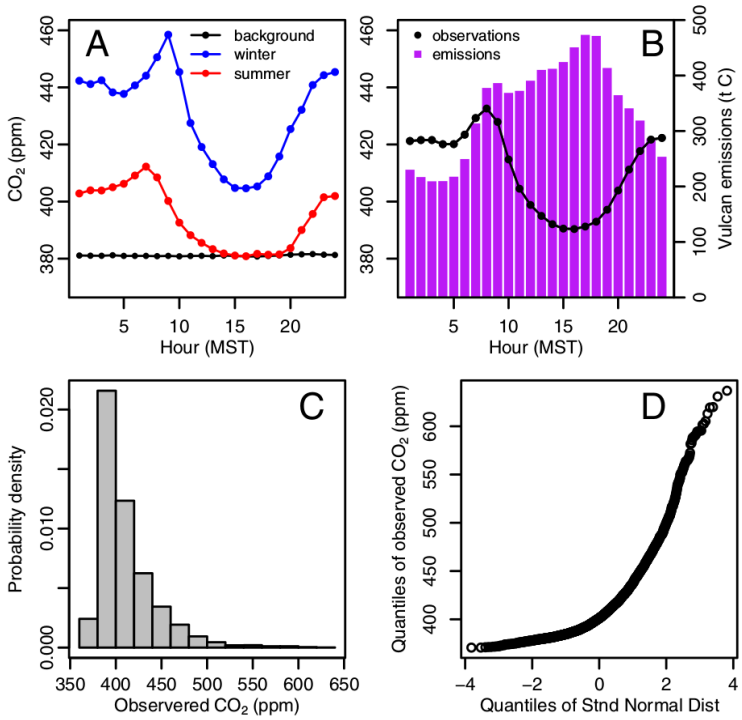

Figure 1-6. Average hourly observed CO_2 concentration at the downtown site in 2006. (A) Averaged by hour of the day from winter (Dec.–Feb.) and summer (June–Aug.) months, and from nearly the entire year (April–Dec.) at the background site. (B) Observed CO_2 from the whole year (Left y-axis) versus average hourly CO_2 emissions estimated from the Vulcan inventory for a 0.5° × 0.5° area encompassing the Salt Lake Valley (Right y-axis). (C and D) Distribution of observed CO_2.

Simulation of CO_2 observations

We used the Weather Research and Forecasting – Stochastic Time-Inverted Lagrangian Transport (WRF-STILT) atmospheric transport model (http://stilt-model.org) and anthropogenic and biogenic flux inventories to simulate the SLC CO_2 data, as described in the Methods section below and references therein. The observation-model framework was tested for four monthly time periods from different seasons in 2006 (Table 1-3) and three sampling locations in SLC. We assessed two horizontal resolutions of the ATDM, 4 km ("baseline") and 1.3 km ("high-resolution") (Figure 1-5), the latter of which was tested for only a two-week subset of the autumn time period. The high-resolution ATDM included parameterization of an urban canopy model (UCM) (Chen et al. 2010), which allows for greater heterogeneity in surface properties related to the urban environment than is available in standard WRF configurations. Figure 1-7 shows hourly observed and simulated CO_2 for baseline and high-res models. The time series demonstrates the model's general capability for capturing the typical diel pattern of near-surface CO_2 concentrations, albeit with a systematic underestimation using a priori emissions (Figure 1-7B).

Elsewhere (Nehrkorn et al. 2013), we evaluated the performance of the two WRF configurations (baseline and high-resolution with an UCM) by comparing observed and modeled meteorological parameters from the SLV. The high-resolution meteorological configuration with the UCM led to improved representation of the daily evolution of the surface (2 m) temperature and boundary layer height, especially when the flow was driven by local circulations. Likewise, the high-resolution WRF-STILT model resulted in changes in simulated CO_2, in particular related to the timing of the nocturnal boundary layer formation and breakup (Figure 1-7B).

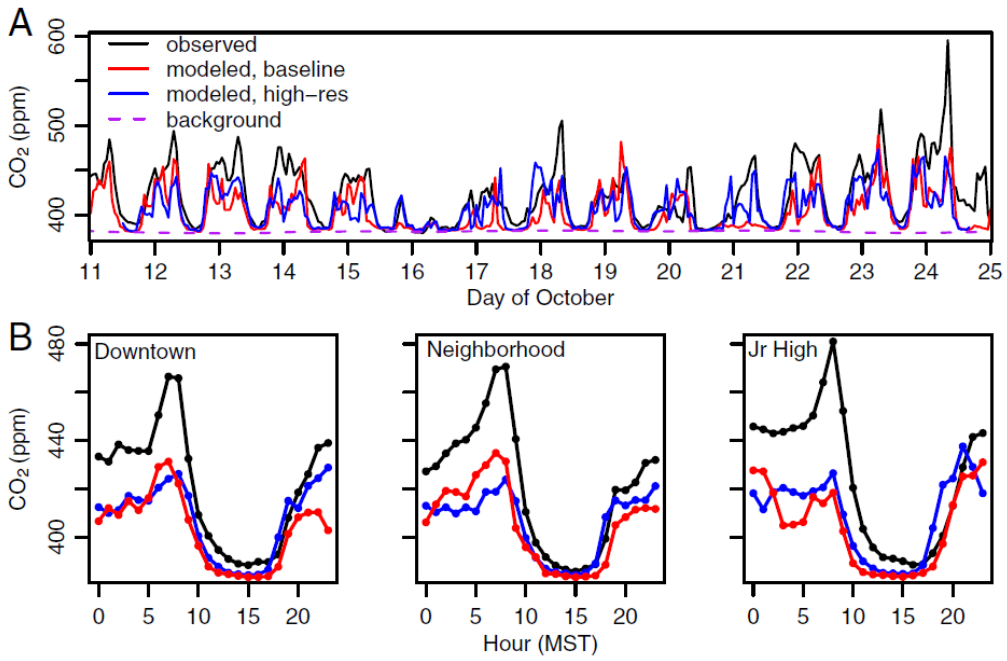

Figure 1-7. Hourly observed and modeled CO_2 concentrations for two weeks in October 2006 (A) at the downtown site, and (B) averaged by hour of the day at the downtown, neighborhood, and junior high sites.

The model captures many weather-related events such as the multi-day persistence of low concentrations around October 16 and August 30 (Figures 1-7A and 1-8B). Some, generally short, time periods are poorly simulated, such as on June 24-25, when the model substantially underestimates observed CO_2 (Figure 1-8A). The model also captures seasonal variability in the magnitude and variance of CO_2 enhancements (Table 1-3). In December, the model is often unable to simulate CO_2 concentrations at hourly resolution (Figure 1-8D), although this result was not unexpected because meteorological conditions during strong winter temperature inversions in valleys are difficult to simulate (Finn et al. 2008). But the model does capture the very high variances in CO_2 and the general amplitude of enhancements over background during December (Table 1-3, Figure 1-8D).

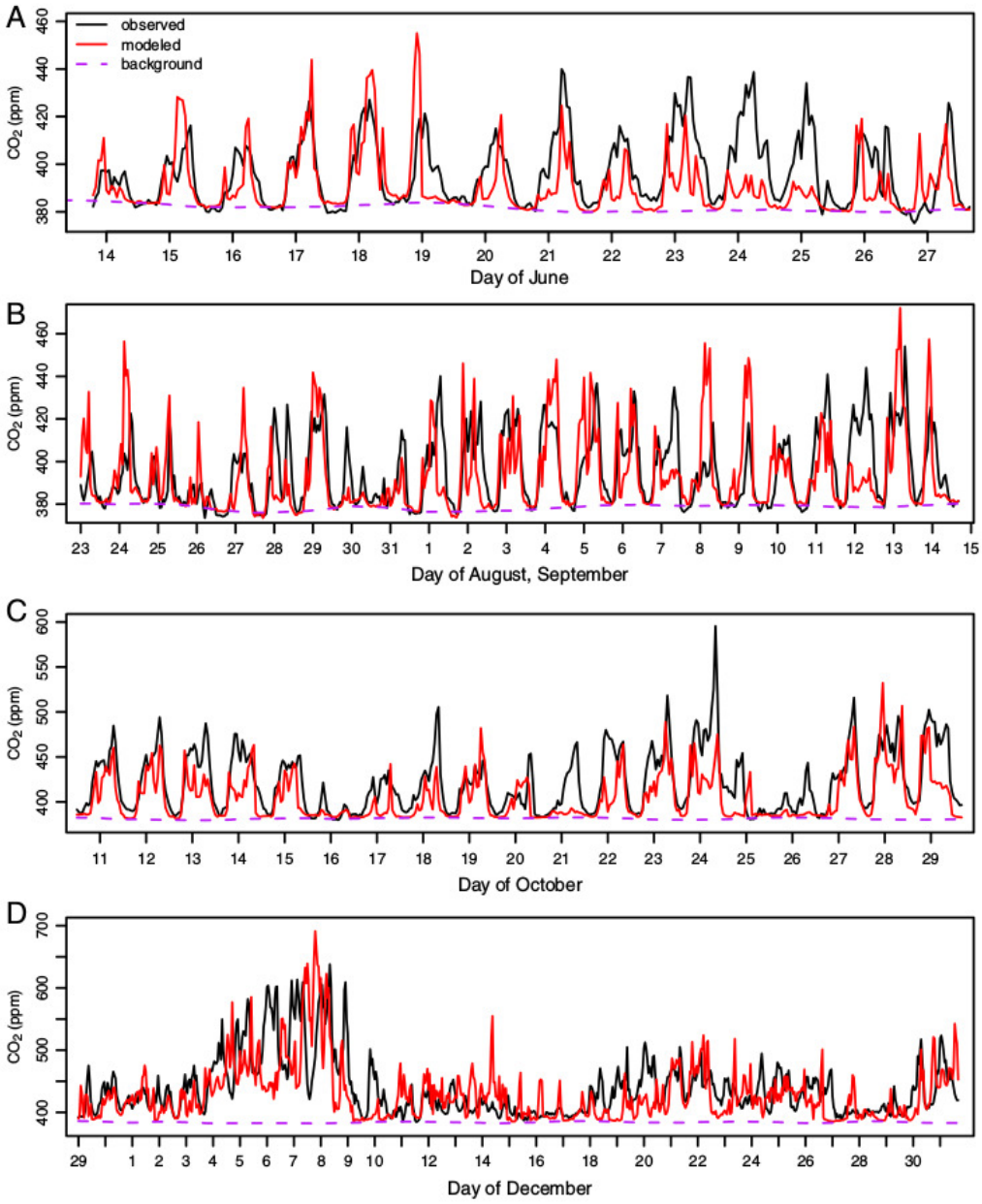

Figure 1-8. Hourly observed and modeled CO_2 concentrations for four time periods in 2006 at the downtown site. Modeled values are from the baseline configuration only. Background values are shown by the dashed line.

The model biosphere sometimes draws down simulated CO_2 in SLC below background during midday, in the spring and summer months only, in agreement with the observations (Figure 1-6A), and known irrigation practices, and contributes small enhancements from plant

and soil respiration during all other times. Overall, the model suggests that the biosphere has a relatively minor influence on CO_2 concentrations in SLC, which is not surprising given the semi-arid ecosystems of the region and previous findings (Pataki et al. 2009, Strong et al. 2011, Ramamurthy and Pardyjak 2011).

Quantification of the data-model relationship

Two approaches were employed to quantify the relationships between hourly observed and simulated CO_2 concentrations for the four time periods and three observation sites. We first applied a Type II, standard major axis regression (Warton et al. 2006) to fit a line to observed versus simulated values (Figure 1-9). The inverse of the regression line slope provides an estimate of the optimum factor by which to scale emissions inventory to best match the observed data. Confidence intervals (CIs) on the slope define our ability to detect changes in emissions over time at the 95% confidence level, assuming spatial and temporal biases in the model are unchanging over time.

Because the regression is based on modeled and observed values paired in time, it may be susceptible to sporadic failures in the transport model, and thus may lead to CIs which are overly pessimistic in terms of trend detection capability. We therefore adopted an alternative approach which gives less weight to poorly timed events by selecting scaling factors that minimize the differences in observed and simulated population means from each site and time period. 95% CIs for this optimization procedure were calculated using a percentile bootstrap.

Table 1-4 gives scaling factors generated by both optimization methods for the high-res and baseline models for October. Table 1-5 gives scaling factors for the other time periods. Mean scaling factors for October from the high-resolution model are between 1.5 and 1.8, with 95% CIs that are ±7-8% of the mean (Table 1-4). Mean scaling factors for other seasons from the

baseline model mostly range between 1 and 2 and have 95% CIs that are ±6-13% of the means (Table 1-5).

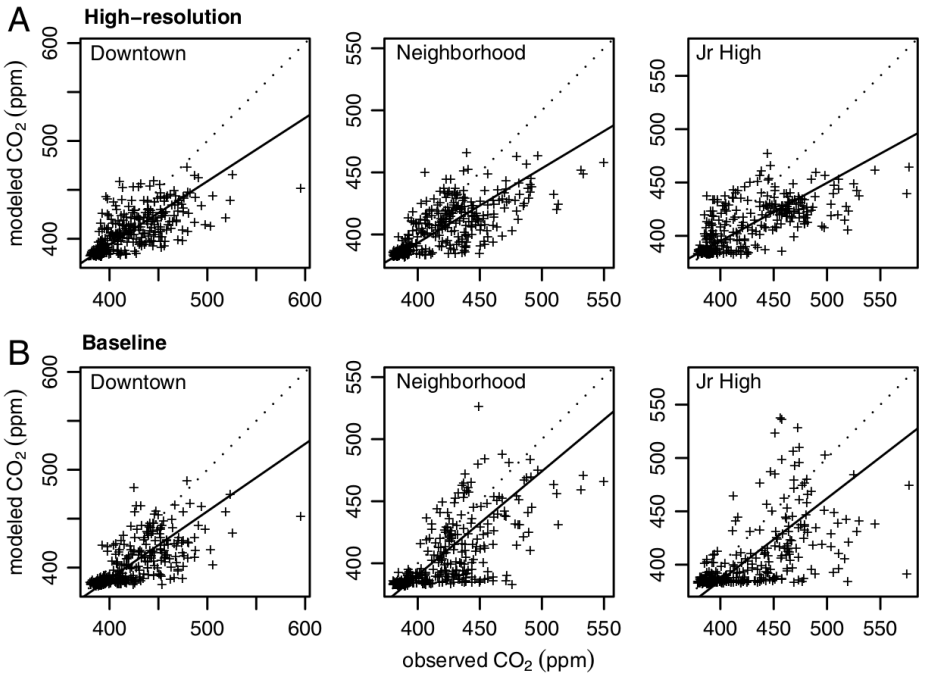

Figure 1-9. Hourly modeled versus observed CO_2 at three sites for a two-week time period in October 2006 resulting from (A) high-resolution and (B) baseline model configurations. Solid lines are standard major axis regression lines and dashed lines are one-to-one shown for reference.

Table 1-4. Mean scaling factors by two optimization procedures and 95% confidence intervals for baseline and high-resolution models at three sites for a 2-wk time period in October 2006.

Site	Model configuration	Scaling factor (±95% CI) (CI/mean)	
		by regression	by minimizing differences in means
Downtown	high-res, UCM	1.54 (±0.12) (±8%)	1.52 (±0.11) (±7%)
	baseline	1.45 (±0.12) (±8%)	1.83 (±0.16) (±9%)
Neighborhood	high-res, UCM	1.67 (±0.13) (±8%)	1.63 (±0.11) (±7%)
	baseline	1.20 (±0.10) (±8%)	1.67 (±0.16) (±9%)
Junior High	high-res, UCM	1.83 (±0.15) (±8%)	1.59 (±0.12) (±8%)
	baseline	1.30 (±0.11) (±9%)	1.93 (±0.24) (±12%)

Table 1-5. Mean scaling factors by two optimization procedures and 95% confidence intervals from the baseline model for three sites and four time periods in 2006.

Site	Time period	Scaling factor (±95% Confidence Interval)	
		by regression	by minimizing differences in means
Downtown	June 13 – 27	1.13 (±0.10) (±9%)	1.60 (±0.21) (±13%)
Downtown	Aug. 23 – Sep. 14	0.90 (±0.06) (±7%)	1.13 (±0.11) (±9%)
Downtown	Nov. 29 – Dec. 31	1.03 (±0.06) (±6%)	1.21 (±0.08) (±7%)
Downtown	Oct. 10 – 29	1.31 (±0.08) (±6%)	1.73 (±0.13) (±7%)
Neighborhood	Oct. 10 – 29	1.14 (±0.07) (±6%)	1.60 (±0.13) (±8%)
Junior High	Oct. 10 – 29	1.32 (±0.09) (±7%)	1.93 (±0.18) (±9%)

Scaling factors for the high-resolution model are similar to those for the baseline model, but are more consistent between sites and optimization methods, and have narrower CIs (Table 1-4). We infer that the high-resolution model is better for trend assessment, although this was not immediately apparent by visual inspection of Figure 1-7. Improvements by the high-resolution model are especially noticeable in the decreased persistence of very low model values when the data indicate elevated concentrations (Figure 1-10). When inventory fluxes are multiplied by the optimal scaling factors, the distributions of simulated CO_2 from the high-resolution model are remarkably close to observed distributions (Figure 1-10), although variance was not included in the optimization procedure.

These results support the application of high-resolution modeling, and optimization of sample distributions and regressions, for determining trends in urban emissions. We infer from the results reported in Table 1-4 for the high-resolution model that 15% is a conservative estimate of the minimum increase or decrease in monthly emissions detectable by our observation-model framework, although caution must be exercised in generalizing these results due to the short time period (~2 weeks) for which the high-resolution model was tested. By

applying the framework to several years' worth of data, changes in scaling factors, and thus relative changes in emissions, could likely be estimated with greater precision.

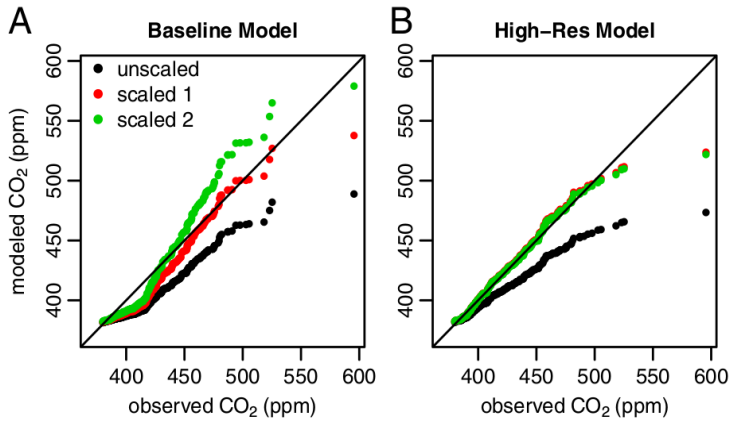

Figure 1-10. Quantile–quantile plots of hourly modeled versus observed CO_2 at the downtown site for two-weeks in October 2006 from (A) baseline and (B) high-resolution models. Model values unscaled and scaled by the two optimization methods are shown. For the high-resolution model, scaling factors by the two optimization methods are near identical, so the two scaled model distributions are nearly indistinguishable.

The scaling factors generated in this study are significantly greater than the expected value of 1.0 (Tables 1-4 and 1-5), implying that emissions were under-reported for the SLC urban core and/or that modeled meteorology was too well-mixed. However, absolute emissions cannot be evaluated with the same level of accuracy as can a change in emissions over time because our statistical procedures do not account for systematic model errors, such as possible over- or under-estimation of the mean boundary layer height or biases in the presumed spatial distribution of emissions. To evaluate absolute emissions, rather than a change in emissions, a fiducial tracer or a sustained release experiment would be necessary.

Approaches for improving emission trend detection

A key limitation to further constraining emissions is the inability of current models to simulate small-scale atmospheric processes. Examples of processes which affect concentrations over short time scales at individual urban sites, but which models cannot explicitly represent, include circulations at building, street, and neighborhood scales, and intermittent turbulence in the nocturnal boundary layer. Improved parameterization of these processes could significantly improve the capability of atmospheric models to simulate urban GHG concentrations. Representation of proximal emission processes at an enhanced spatial resolution similar to that of the meteorology (1.3 km) could also lead to improved simulations.

Contrary to the expectations of some (cf. JASON 2011), the SLC case suggests that increasing the number of surface measurement stations across the city would be ineffective at substantially improving the observational approach for detecting a change in emissions. Simulations indicate that individual measurements sites are sensitive to emissions across the full urban region (Figure 1-4). Observed CO_2 concentrations at the five measurement stations in SLC are strongly correlated on a daily basis (Figure 1-10) because within day variance is dominated by the diel cycles in atmospheric stability (Figure 1-6) and forcing of these cycles occurs on the scale of the whole valley. This finding suggests that the current network of five stations in SLC is more than adequate for characterizing the daily cycle of urban-scale CO_2. If we consider just the afternoon hours, the opposite problem occurs: fluctuations at stations quite close together (< 5 km) are not significantly correlated (Figure 1-11), suggesting that small-scale processes are responsible for CO_2 concentration variations in the afternoon and are not directly tied to region-wide emissions. Hence, denser measurements of such variations would not help to significantly improve determination of regional trends.

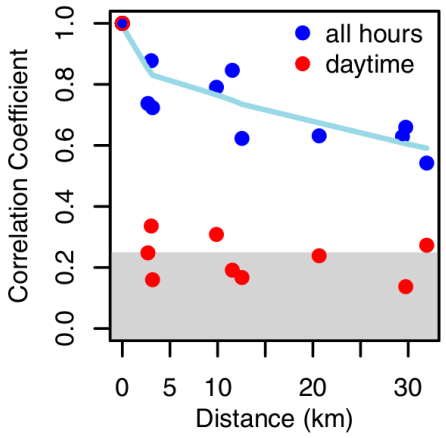

Figure 1-11. Cross-correlation functions for 5-min observed CO_2 among the five measurement sites at optimum lag times for March 16–Oct. 27, 2006. Data for all hours and for daytime hours only (11–18 h MST) are plotted against the distance between sites. Correlation coefficients less than 0.25 are insignificant.

Alternative measurement strategies that are less sensitive to the details of atmospheric circulation and emissions may lead to improved trend detection capability. Shallow circulations rearrange CO_2 between sub-layers of the atmosphere on hourly timescales, but for the duration that emitted CO_2 remains in the urban region, total column amounts are directly linked to total emissions. Figure 1-12 shows simulations of the characteristic pattern of CO_2 enhancement, vertically integrated through the partial atmospheric column, which comprises the "urban dome" over the SLV. Observations throughout the column are not available for validation, but simulations appear to have sufficient fidelity at the surface (Figure 1-7) to justify exploration of the character of the urban dome through modeling. The position of the urban dome shifts with the wind, but, due to the valley topography (Figures 1-12C and 1-1), its core generally lies on a predictable NW-SE axis. During the day, the dome extends vertically up to 2 km, but at night, excess CO_2 is contained within a thin layer less than 100 m deep (Figure 1-12FG).

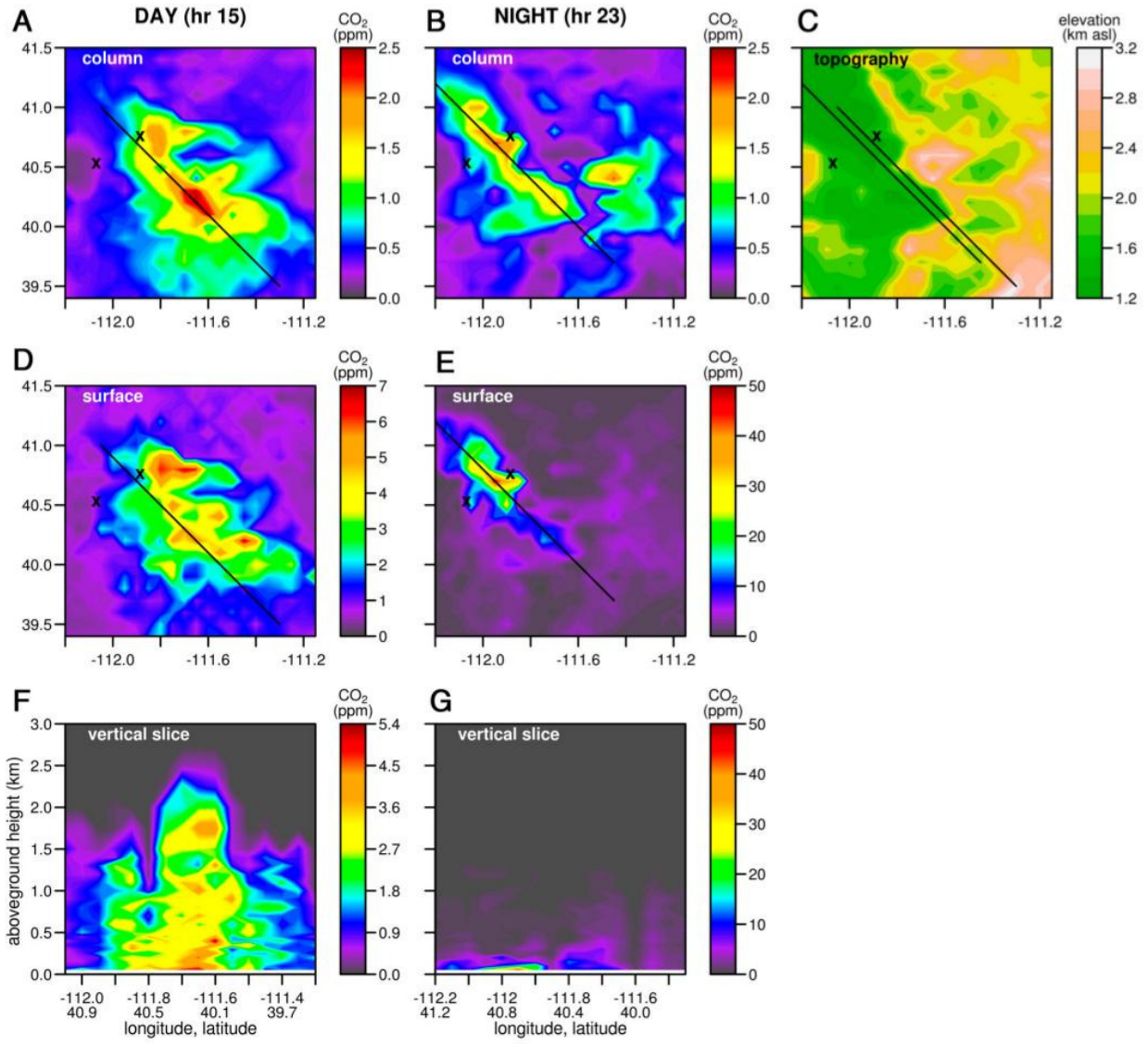

Figure 1-12. Simulated partial column-averaged XCO_2 (ppm) enhancements above background up to 3 km above SLC and the surrounding area on October 18, 2006 at 15 h (A) and 23 h (B) MST. (D and E) Simulated CO_2 enhancement near the surface, 50 m above the ground, for the same times and locations as in A and B. (F and G) Vertical slices through the areas of maximum XCO_2 enhancement in the urban domes. (C) Topography in kilometers above sea level. The downtown and rural measurement sites are marked with Xs for reference. Lines in A–E show the positions of the transects plotted in F and G. Note that the two upper-left panels have the same scale, but the four lower panels do not.

The differences between enhancements at the surface and those integrated through the partial column are striking. The areal extent and magnitude of column enhancements are larger

in the day than the night (Figure 1-12AB), directly reflecting the higher daytime emissions (Figure 1-6B) that we wish to measure. We infer that urban enhancements in column amounts are more sensitive to regional-scale meteorology, especially mean wind speeds, and to emissions integrated through the whole urban region. Conversely, surface values are more sensitive to boundary layer height, shallow circulations, and local traffic emissions. Mean winds are much easier to model than boundary layer heights, and can be validated with hourly observations from airports and weather stations. Broad scale emission inventories are better defined than fine-scale, day-to-day traffic patterns.

The magnitude of the anthropogenic CO_2 enhancement in the partial column integral is notably smaller than at the surface, by factors of 2 (daytime, Figure 1-12AD) to 20 (nighttime, Figure 1-12BE), suggesting that increased accuracy may be required to both measure and simulate the column enhancement. To our knowledge, ground-based measurements of CO_2 column amounts with the accuracy required for verification have been demonstrated just once, in Los Angeles, where peak concentrations in the column were indeed observed in midday (Wunch et al. 2009). Total column measurements could be made from space, obviating the need for many surface stations and eliminating intrusive measurements on the territory of a treaty signatory. The widespread, spatially heterogeneous, and shifting nature of the simulated SLC urban dome suggests that remote sensing of the dome may offer the best route for its full characterization. Unfortunately, no presently planned satellite has the necessary orbit or targeting capability.

Summary and future directions

We have demonstrated an observation-model framework capable of detecting a change in anthropogenic CO_2 emissions of 15% or more from an urban region on a monthly basis. The

model framework consists of an atmospheric transport model (STILT) driven by a high-resolution (1.3 km) mesoscale meteorological model (WRF) and coupled to moderately high-resolution models of the spatial and temporal distribution of anthropogenic emissions (Vulcan) and biogenic fluxes. We compared simulations to observations from four time periods and three locations in SLC. Constraints on emission rates were obtained by optimizing the emission model two ways, both of which gave similar central values and confidence intervals.

The observation-model framework is readily scalable to other sites using commercial sensors and open-source models. Measurements are needed to define background (upwind) values, especially for urban areas downwind of other major source regions. For heavily vegetated cities, it will be necessary to distinguish anthropogenic from biogenic emissions, possibly with tracer measurements of fossil fuel combustion (e.g. CO, ^{14}C). Analysis of the statistical correlations among the SLC measurement sites indicates that five was an ample number, although this result likely depends on SLC's relatively small size and topographic confinement.

We argue that measurements of vertically integrated column amounts would provide more new information than would additional surface sites. In our estimation, column measurements offer a promising route for improved detection of CO_2 emissions from major source regions, complementing or possibly obviating the need for extensive surface measurements near these areas. Remote sensing of the column-integrated "urban dome" appears to offer the best route for accurate verification of emission inventories of CO_2 and other GHGs.

Acknowledgements

We thank Dean Cardinale and the Snowbird Ski and Summer Resort for their support at HDP, and Kevin Gurney for providing the Vulcan emission inventory. This study was supported by Grants NNX11AG47G and NNX08AR47G from the National Aeronautics and Space Administration (NASA) and ATM-0830916 from the National Science Foundation (NSF) to Harvard University, by NSF Grant ATM-0836153 to Atmospheric and Environmental Research, Inc., and by the U.S. intelligence community. Any opinions, findings, conclusions, and recommendations expressed in this material are those of the authors and do not necessarily reflect the views of the intelligence community, NSF, or NASA. The SLV CO_2 observation network was supported by the Office of Science (BER), U.S. Department of Energy, Grants DE-FG02-06ER64309 and DESC0005266. HDP measurements were supported by NSF Grant EAR-0321918 and National Oceanic and Atmospheric Administration Grant NA09OAR4310064. The National Center for Atmospheric Research is sponsored by the NSF.

References

Baldocchi D, Falge E, Gu L, Olson R, Hollinger D, Running S, Anthoni P, Bernhofer C, Davis K, Evans R, Fuentes J, Goldstein A, Katul G, Law B, Lee X, Malhi Y, Meyers T, Munger W, Oechel W, Paw U KT, Pilegaard K, Schmid HP, Valentini R, Verma S, Vesala T, Wilson K, Wofsy S (2001) FLUXNET: A new tool to study the temporal and spatial variability of ecosystem-scale carbon dioxide, water vapor, and energy flux densities, Bulletin of American Meteorological Society 82: 2415-2434.

Bergeron O, Strachan IB (2011) CO_2 sources and sinks in urban and suburban areas of a northern mid-latitude city, Atmospheric Environment, 45 (8): 1564-1573.

Chen F, Kusaka H, Bornstein R, Ching J, Grimmond CSB, Grossman-Clarke S, Loridan T, Manning KW, Martilli A, Miao SG, Sailor D, Salamanca FP, Taha H, Tewari M, Wang XM, Wyszogrodzki AA, Zhang CL (2010) The integrated WRF/urban modeling system: development, evaluation, and applications to urban environmental problems, International Journal of Climatology, 31 (2): 273-288.

Ciais P, Rayner P, Chevallier F, Bousquet P, Logan M, Peylin P, Ramonet M (2010) Atmospheric inversions for estimating CO_2 fluxes: methods and perspectives, Climatic Change, 103 (1-2): 69-92.

Conway TJ, Lang PM, Masarie KA (2009) Atmospheric carbon dioxide dry air mole fractions for the NOAA ESRL carbon cycle cooperative global air sampling network, 1968-2008, Ver 2009-07-15. Available at ftp://ftp.cmdl.noaa.gov/ccg/co2/flask/event.

Eggleston HS, Buendia L, Miwa K, Ngara T, Tanabe K , eds. (2006) 2006 IPCC Guidelines for National Greenhouse Gas Inventories (Institute for Global Environmental Strategies, Hayama, Japan), prepared by the National Greenhouse Gas Inventories Program.

Finn D, Clawson KL, Carter RG, Rich JD (2008) Plume dispersion anomalies in a nocturnal urban boundary layer in complex terrain, Journal of Applied Meteorology and Climatology, 47 (11): 2857-2878.

Gerbig C, Lin JC, Wofsy SC, Daube BC, Andrews AE, Stephens BB, Bakwin PS, Grainger CA (2003) Toward constraining regional-scale fluxes of CO_2 with atmospheric observations over a continent: 2. Analysis of COBRA data using a receptore-oriented framework, Journal of Geophysical Research - Atmospheres 108 (D24): 4757-4778.

Gratani L, Varone L (2005) Daily and seasonal variation of CO_2 in the city of Rome in relationship with traffic volume, Atmospheric Environment, 39 (14): 2619-2624.

Gregg JS, Andres RJ, Marland G (2008) China: emissions pattern of the world leader in CO_2 emissions from fossil fuel consumption and cement production, Geophysical Research Letters, 35 (8): L08806.

Gurney KR, Mendoza DL, Zhou YY, Fischer ML, Miller CC, Geethakumar S, Du Can SD (2009) High resolution fossil fuel combustion CO_2 emission fluxes for the United States, Environmental Science and Technology, 43 (14): 5535-5541.

Homer C, Huang CQ, Yang LM, Wylie B, Coan M (2004) Development of a 2001 national land cover database for the United States, Photogrammetric Engineering and Remote Sensing 70 (7): 829-840.

JASON (2011) Methods for remote determination of CO_2 emissions (MITRE Corporation, McLean, VA), JSR-10-300, www.fas.org/irp/agency/dod/jason/emissions.pdf.

Levin I, Hammer S, Eichelmann E, Vogel FR (2011) Verification of greenhouse gas emission reductions: the prospect of atmospheric monitoring in polluted areas, Philosophical Transactions of the Royal Society A, 369 (1943): 1906-1924.

Lin JC, Gerbig C, Wofsy SC, Andrews AE, Daube BC, Davis KJ, Grainger CA (2003) A near-field tool or simulating the upstream influence of atmospheric observations: the Stochastic Time-Inverted Lagrangian Transport (STILT) model, Journal of Geophysical Research – Atmospheres, 108 (D16): 4493.

Mahadevan P, Wofsy SC, Matross DM, Ziao XM, Dunn AL, Lin JC, Gerbig C, Munger JW, Chow VY, Gottlieb EW (2008) A satellite-based biosphere parameterization for net ecosystem CO_2 exchange: Vegetation Photosynthesis and Respiration Model (VPRM), Global Biogeochemical Cycles, 22 (2): BG2005.

Marland G (2008) Uncertainties in accounting for CO_2 from fossil fuels. Journal of Industrial Ecology, 12 (2): 136-139.

Matross DM, Andrews A, Pathmathevan M, Gerbig C, Lin JC, Wofsy SC, Daube BC, Gottlieb EW, Chow VY, Lee JT, Zhao CL, Bakwin PS, Munger JW, Hollinger DY (2006) Estimating regional carbon exchange in New England and Quebec by combining atmospheric, ground-based and satellite data, Tellus B 58 (5): 344-358.

Mays KL, Shepson PB, Stirm BH, Karion A, Sweeney C, Gurney KR (2009) Aircraft-based measurements of the carbon footprint of Indianapolis, Environmental Science and Technology, 43 (20): 7816-7823.

McRae JE, Graedel TE (1979) Carbon dioxide in the urban atmosphere: dependencies and trends, Journal of Geophysical Research – Oceans and Atmospheres, 84 (NC8): 5011-5017.

National Research Council, Committee on Methods for Estimating Greenhouse Gas Emissions (2010) Verifying greenhouse gas emissions: method to support international climate agreements (The National Academy Press, Washington, D.C.).

Nehrkorn T, Eluszkiewicz J, Wofsy SC, Lin JC, Gerbig C, Longo M, Freitas S (2010) Coupled weather research and forecasting-stochastic time-inverted Lagrangian transport (WRF-STILT) model, Meteorology and Atmospheric Physics, 107 (1-2): 51-64.

Nehrkorn T, Henderson J, Leidner M, Mountain M, Eluszkiewicz J, McKain K, Wofsy S (2013) WRF simulations of the urban circulation in the Salt Lake City area for CO_2 modeling, Journal of Applied Meteorology and Climatology, 52 (2): 323-340.

Pataki DE, Bowling DR, Ehleringer JR (2003) Seasonal cycle of carbon dioxide and its isotopic composition in an urban atmosphere: anthropogenic and biogenic effects, Journal of Geophysical Research – Atmospheres, 108 (D23): 4735.

Pataki DE, Tyler BJ, Peterson RE, Nair AP, Steenburgh WJ, Pardyjak ER (2005) Can carbon dioxide be used as a tracer of urban atmospheric transport?, Journal of Geophysical Research – Atmospheres, 110 (D15): D15102.

Pataki DE, Bowling DR, Ehleringer JR, Zobitz JM (2006) High resolution atmospheric monitoring of urban carbon dioxide sources, Geophysical Research Letters, 33: L038143.

Pataki DE, Xu T, Luo YQ, Ehleringer JR (2007) Inferring biogenic and anthropogenic carbon dioxide sources across an urban to rural gradient, Oecologia, 152 (2): 307-322.

Pataki DE, Emmi PC, Forster CB, Mills JI, Pardyjak ER, Peterson TR, Thompson JD, Dudley-Murphy E (2009) An integrated approach to improving fossil fuel emissions scenarios with urban ecosystem studies, Ecological Complexity, 6 (1): 1-14.

Peylin P, Houweling S, Krol MC, Karstens U, Rodenbeck C, Geels C, Vermeulen A, Badawy B, Aulagnier C, Pregger T, Delage F, Pieterse G, Ciais P, Heimann M (2011) Importance of fossil fuel emission uncertainties over Europe for CO_2 modeling: model intercomparison, Atmospheric Chemistry and Physics, 11 (13): 6607–6622.

Ramamurthy P, Pardyjak ER (2011) Toward understanding the behavior of carbon dioxide and surface energy fluxes in the urbanized semi-arid Salt Lake Valley, Utah, USA, Atmospheric Environment, 45 (1): 73-84.

Skamarock WC, Klemp JB (2008) A time-split nonhydrostatic atmospheric model for weather research and forecasting applications, Journal of Computational Physics, 227 (7): 3465-3485.

Strong C, Stwertka C, Bowling DR, Stephens BB, Ehleringer JR (2011) Urban carbon dioxide cycles within the Salt Lake Valley: a multiple-box model validated by observations, Journal of Geophysical Research – Atmospheres, 116 (D15307): D15307.

Wang Y, Munger JW, Xu S, McElroy MB, Hao J, Nielsen CP, Ma H (2010) CO_2 and its correlation with CO at a rural site near Beijing: implications for combustion efficiency in China, Atmospheric Chemistry and Physics, 10 (18): 8881-8897.

Warton DI, Wright IJ, Falster DS, Westoby M (2006) Bivariate line-fitting methods for allometry, Biological Reviews, 81 (2), 259-291.

Wunch D, Wennberg PO, Toon GC, Keppel-Aleks G, Yavin YG (2009) Emissions of greenhouse gases from a North American megacity, Geophysical Research Letters, 36: L15810.

Zimnoch M, Godlowska J, Nick JM, Rozanski K (2010) Assessing surface fluxes of CO_2 and CH_4 in urban environment: a reconnaissance study in Krakow, southern Poland, Tellus B, 62 (5): 573-580.

Chapter 2

Boston Greenhouse Gas Measurement Network

Abstract

A network of atmospheric greenhouse gas measurement stations has operated continuously in Boston and the surrounding region since 2012. Measurements are made from elevated structures, such as building rooftops and towers, with Picarro cavity ring-down spectrometers. A novel method for sampling from a tall building in an urban environment, where there are many potential sources of contamination by measuring from the corners of the building in sequence, was developed. A system for automated, reliable, remote operation of the measurement network is described. Routine calibrations ensure between-site comparability and allow for characterization of measurement uncertainty. Strategies for improved system reliability and measurement quality, based on our experience operating the network, are discussed. Data from the network can be used to test observation and modeling capabilities in an urban environment, and to investigate the magnitude and patterns of carbon dioxide and methane fluxes in the Boston urban region.

Introduction

Following on the conceptual modeling work for Salt Lake City, we sought to build an urban greenhouse gas observational network in our home city of Boston, Massachusetts, which we could operate out of our lab, and where we could leverage and build upon local knowledge and collaborations to test observational capabilities and investigate a range of questions. We established such a network (Figure 2-1, Table 2-1) beginning in the summer of 2012, and it has operated continuously since then for nearly three years. Each site in the network has a commercial Picarro (Santa Clara, CA, USA) cavity ring-down spectrometer (CRDS) that measures carbon dioxide (CO_2), methane (CH_4), and water vapor (H_2O) continuously in ambient air (Crosson 2008). This chapter describes the measurement network, including site and logistical considerations, software design for data QA/QC and processing, calibration procedures and measurement error characterization, problems encountered and their resolutions, and a summary of the measurement results.

Figure 2-1. Map of the measurement sites in the Boston GHG network at two zoom levels.

Table 2-1. Locations, instrument model and serial numbers, dates of measurement coverage for each site in the Boston GHG measurement network.

Site	Lon, °	Lat, °	Height, m above ground	Picarro model number	Picarro serial number	Dates of measurement coverage
Boston University (BU)	-71.10	42.35	29	G2101-i	CFFDS2051	Aug. 2012 – June 2014
				G1301	CFADS30	June 2014 – present
Copley Square (COP)	-71.08	42.35	215	G2401	CFKADS2033	July 2012 – present
Harvard Forest (HF)	-72.17	42.54	29	G2301	CFADS2211	Aug. 2012 – May 2014
				G2311-f	CFHADS2008	May 2014 – Present
Nahant (NHT)	-70.91	42.42	16	G1301	CFADS30	July 2012 – Feb. 2014
Thompson Island (THI)	-71.01	42.32	25	G2101-i	CFFDS2058	Oct. 2013 – Oct. 2014
UMass Boston (UMB)	-71.04	42.31	62	G2101-i	CFFDS2058	Aug. 2012 – Aug. 2013

Site descriptions

Boston University

At the BU site, the sample inlet is mounted on a 2-meter tower located in the center of the flat rooftop of the 6-story College of Arts and Sciences (CAS) building. The CAS building is located in a neighborhood comprised of both shorter and taller buildings, and a few small bathroom vents are located in distant areas of the roof, so sample air may be periodically influenced by very nearby sources. When the measurements began, the analyzer was located inside the building in a small printer room that had large windows and large temperature swings. In February, 2013, we moved the instrument to a dedicated windowless room in the building's penthouse.

Copley Square

Measurements at the COP site are made from the 51st story of the 52-story Prudential Tower. The Prudential building is much taller than the other buildings in its immediate vicinity so contamination of sample air from nearby building sources is not a major concern. [A new building with a height similar to the Prudential's is planned for nearby Dalton Street (Ross 2015), and this could compromise the quality of the COP observations in the future.] However, the building itself has many large vents on its rooftop for bathrooms, building air-handling systems, and a restaurant. Furthermore, airflow over a building leads to the formation of small-scale turbulence and a zone of low pressure at the top of the building, which can entrain or aspirate air emitted from the building (Prasad et al. 2013).

To reduce the likelihood of sampling air emitted from building vents, four sample inlets were placed at the corners of the building, one story below the top of the building, where a balcony (used to stage window-washing equipment) allows for access to the building's exterior (Figure 2-2). The concept of the COP corner-sampling method is that, at any given time, at least one corner will sample air that is representative of uncontaminated, upwind conditions. Each corner is sampled sequentially for five minutes and the upwind corner(s) is selected (Figure 2-3) as that with the lowest average concentration of CO_2, CH_4, or CO in each 20-minute, 4-corner sequence (Figure 2-4).

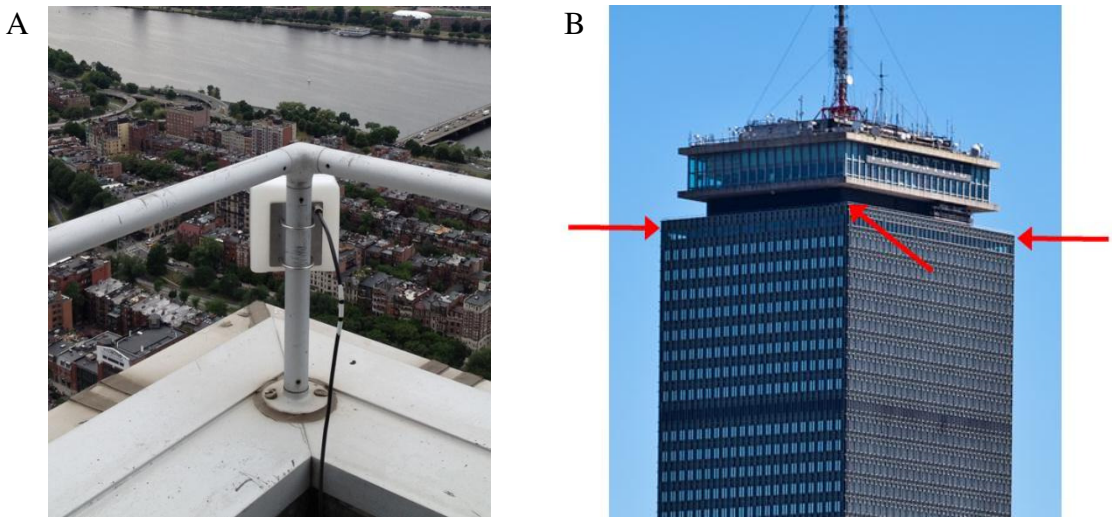

Figure 2-2. (A) A sample inlet at one of the corners of the Prudential Tower, and (B) exterior view of the building with red arrows indicating the locations of the sample inlets at each of the building's four corners on the 51st story.

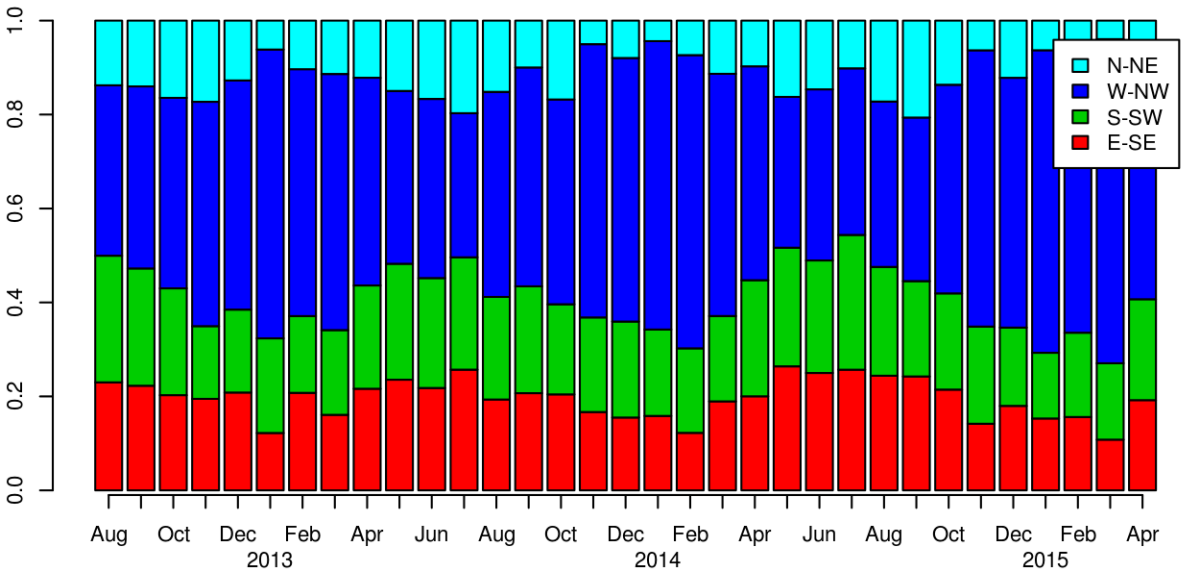

Figure 2-3. Monthly average fractional contribution of each corner to the selected data at the COP site. The legend describes the orientation of each corner.

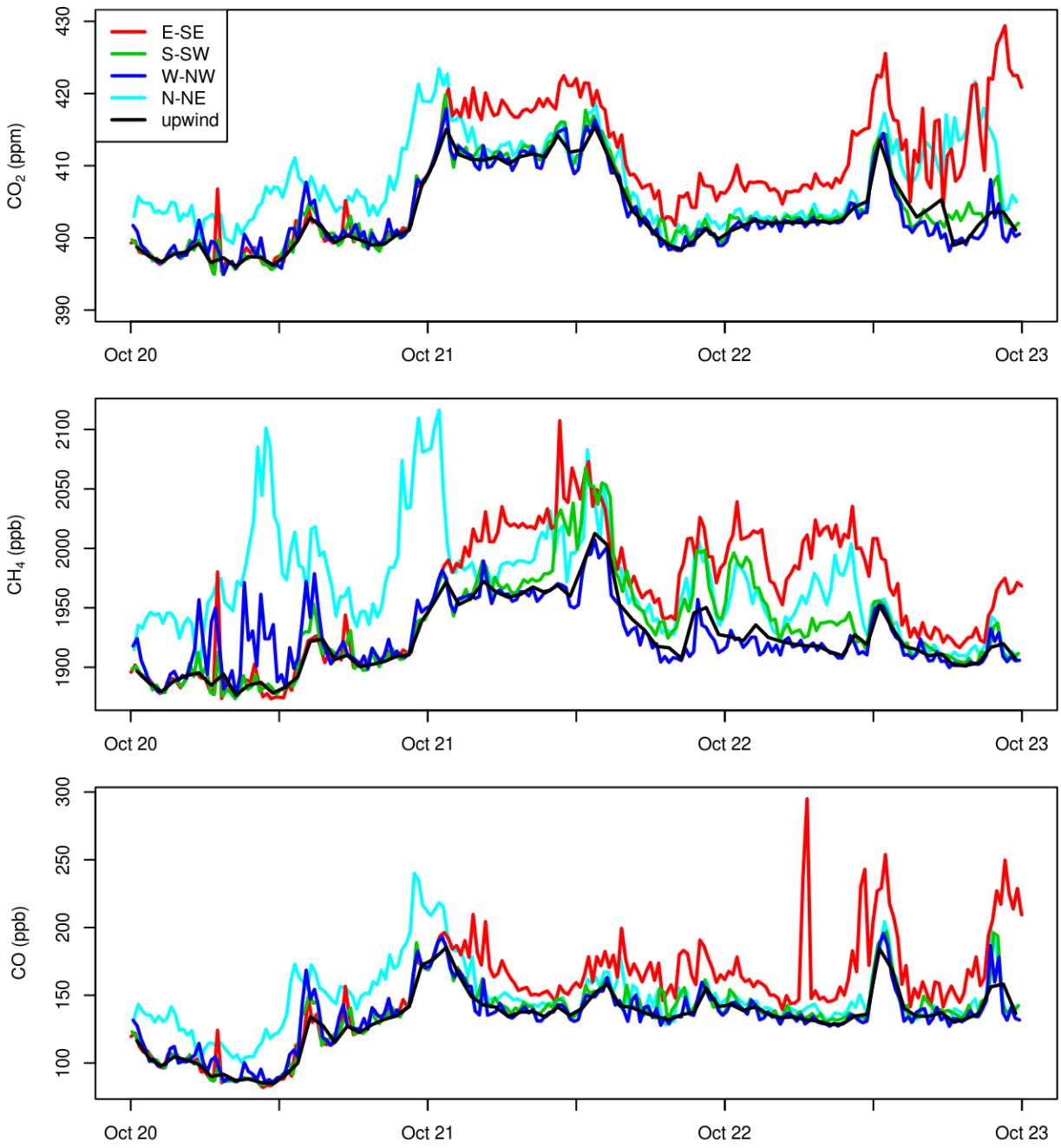

Figure 2-4. Example of the COP corner-sampling method for three days in October, 2012. The colored lines show average concentrations during each 5-minute sampling interval from each corner. The black line shows the average hourly inferred upwind concentration. The legend describes the orientation of each corner.

Harvard Forest

Observations at HF were integrated into the existing Environmental Monitoring Site, where atmospheric measurements have been made from a tower in a mixed-deciduous forest in central Massachusetts (Figure 2-1) for over two decades (Urbanski et al. 2007). Samples were drawn from eight heights (0.3, 0.8, 4.5, 7.5, 12.7, 18.3, 24.1, and 29 m) on the tower, for four minutes each and for eight minutes at the highest level. Measurements from the top level at the HF site are intended to provide background concentrations for Boston during conditions of westerly flow. Measurements from the vertical profile can be used to estimate ecosystem-scale flux rates (e.g. Meredith et al. 2014).

To test whether the non-continuous sampling at HF and COP reduced the representativeness of the datasets, we simulated the COP sub-sampling routine with the continuous BU dataset by randomly sub-selecting one 5-minute period in each 20-minute interval. The hourly averages generated from the sub-selected dataset were not significantly different than hourly averages generated from the full dataset.

Nahant

Nahant is a tied island located northeast of Boston in Massachusetts Bay (Figure 2-1). Measurements at NHT were made from the fifth story a fire control tower located in a residential area ~50 m from the northeastern shore of the island. Because the roof of the fire control tower was not accessible, the sample inlet was mounted on a ~1 m boom that extended out a window on the northwestern side of the building (for ascetic reasons; Figure 2-5). During the ~1.5 year measurement period at this site (Table 2-1), the fire control tower was not occupied and the nearby residence was seldom occupied. Measurements at NHT were discontinued in 2014 when the owners of the property undertook major renovations and full-time residence. The NHT site

was intended to provide background concentrations for Boston during conditions of on-shore flow.

A B

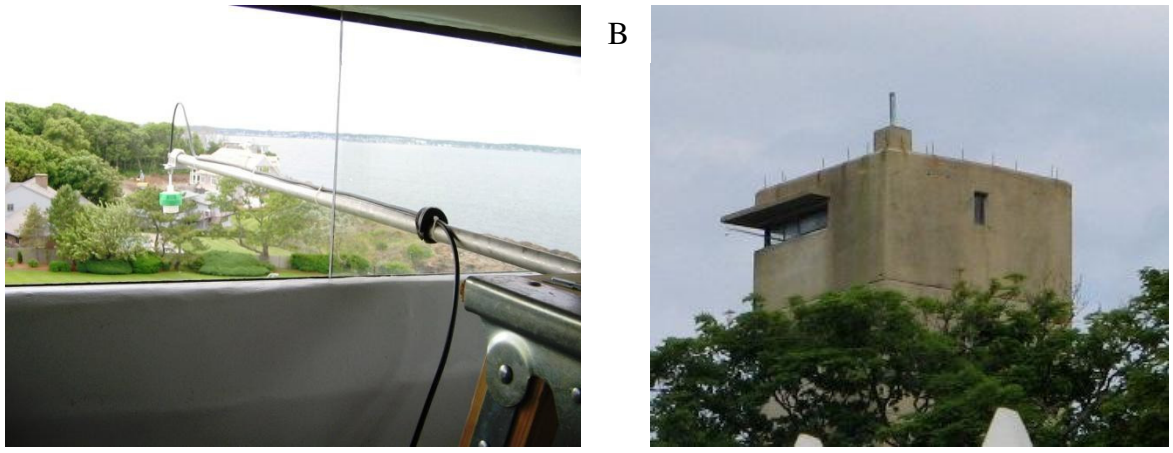

Figure 2-5. (A) Interior and (B) exterior view of the boom-mounted sample inlet at the NHT site.

University of Massachusetts, Boston

Measurements at UMB were made from the 12-story Healey Library building, which is located ~500 m from the Boston Harbor in Dorchester, MA (Figure 2-1). The sample inlet was mounted to a vertical pole that extended from the dome of the disused Martin Observatory (Figure 2-6). After one year of measurements, the analyzer was moved from this site to Thompson Island because measurements were determined to be vulnerable to contamination from many nearby rooftop and building sources.

Figure 2-6. Sample inlet mounted above the observatory dome at the UMB site.

Thompson Island

Thompson Island is located in the Boston Harbor ~2.5 km from downtown Boston (Figure 2-1). The island is accessible by ferry from South Boston and is mostly used for seasonal recreational and educational activities through its affiliation with the Outward Bound organization and Boston Harbor Islands National Park Area. The sample inlet at THI is mounted to the top of a flagpole on a small hill near the center of the island, and the instrument is housed in a nearby dormitory building (Figure 2-7). Measurements were discontinued in the fall of 2014 (Table 2-1) and are schedule to resume in the early summer of 2015 upon the completion of a building renovation project.

Figure 2-7. The flagpole on Thompson Island where the sample inlet is mounted.

Most of the analyzers are housed in locations where the ambient temperature stays within the range required by the analyzers to operate (specified by the manufacturer as ~10-35 °C), but is not controlled by us and therefore can exhibit strong daily and seasonal variability, depending on the site. The HF site is cooled with an air conditioning system throughout the year to counterbalance the heat produced by the many instruments and computers in the room. The THI site is heated in the winter with electric space heaters, but is not cooled in the summer. The NHT site had no temperature control, so to keep the analyzer warm enough in the winter, a cardboard box was placed over the instrument rack to reduce the volume into which the instrument's exhaust heat was mixed.

Analyzer descriptions

Picarro CRDS analyzers measure $^{12}C^{16}O_2$ at 1603 nm, and $^{12}C^{1}H_4$ and $^{1}H_2{}^{16}O$ at 1651 nm with a pair of near-infrared diode lasers. The CRDS measurement is made by emitting laser light into an optical cavity containing the sample gas, turning off the laser, and measuring the time

constant of the decay in light intensity ("ring-down time") as light is absorbed by the target gas in the cavity. Stable temperature and pressure conditions in the optical cavity and a high-precision wavelength monitor promote high precision and longterm stability in the CRDS measurements (Crosson 2008).

Several different models of Picarro analyzers have been used in the Boston network to measure CO_2, CH_4, and H_2O (Table 2-1). Models G1301, G2301, and G2401 have nearly identical spectroscopy and similar performance characteristics. The G1301 was the first available commercial model, and the G2401 measures carbon monoxide (CO), in addition to CO_2 and CH_4. Model G2101-i analyzers also measure $^{13}CO_2$ and compute $\delta^{13}CO_2$, but those data have not been used because we did not implement a calibration system for $\delta^{13}C$. The model G2311-f analyzer has a second operational mode intended for eddy-flux applications, with a higher measurement rate (10 Hz compared to 0.2 Hz) and reduced precision, but this "fast flux" mode was not utilized for the Boston network. Measurement intervals are ~2 seconds for all species on all analyzers, except for the G1301, which measures H_2O every ~14 seconds, and for the G2101-i, which measures CH_4 and H_2O every ~7 seconds.

The analyzers' operation and data acquisition systems are controlled by Picarro software running on a dedicated Windows computer. The temperature and pressure of the Picarro optical cells are strictly controlled to 45 ± 0.005 °C and 140 ± 0.1 torr, except for analyzer CFHADS2008, which has set points of 60 °C and 151.5 torr. Occasionally, when ambient temperatures and sample gas flow rates undergo large abrupt changes, the analyzer cavity may temporarily exceed its specified temperature or pressure range while it acts to respond to changing conditions.

Measurement infrastructure

At each site, the Picarro analyzer and associated equipment are housed indoors and sample air is drawn from the outdoors through a sample line (Figure 2-8). The outdoor terminus of each sample line is capped with a 2 µm disc filter (47 mm diameter PTFE membrane, Pall Corp., Port Washington, NY, USA) to prevent ingestion of particles and liquid water. Filter-holders at the inlets are oriented vertically with the open end pointing down (e.g. Figure 2-5) to aid the shedding of precipitation, which can otherwise pool in the filter holder and restrict air flow. The outdoor filters are replaced every ~3-4 months. To avoid the use of removable components near the building's ledge, for safety reasons, at the COP site, filters are located in-line downstream of each inlet (Figure 2-9), and fixed shrouds are used to shield inlets from precipitation (Figure 2-2). A few small holes were added to the interior side of each shroud to facilitate air circulation.

In the standard configuration, the sample pump supplied by Picarro (PU2115-N84.0-12.07, KNF Neuberger, Trenton, NJ, USA) is located downstream of the analyzer and provides flow through the entire measurement system (Figure 2-8). The model G2101-i analyzers at the BU, UMB, and THI sites (Table 2-1) have lower flow rates (~25 standard $cm^3 \cdot min^{-1}$ (sccm) compared to ~250 sccm), which led to unacceptably long residence times in the sample lines. Therefore, bypass pumps (UN05ATI, KNF Neuberger) were added upstream of the G2101-i analyzers to minimize residence times in sample lines (Figure 2-10).

Residence times at sites with long sample lines were approximated by blowing in the inlet and measuring the time until the CO_2 spike was recorded by the analyzer. Sample residence times, were ~35 and ~13 minutes before the bypass pumps were installed, and ~90 and ~30

seconds after the bypass pumps were installed, at the BU and UMB sites, respectively. At the COP site, the four sample lines are continuously flushed with a bypass pump (Figure 2-9) and have equal lengths to ensure equivalent residence times (~6 minutes) among them. A [porous metal] flow restrictor (Mott Corporation, Farmington, CT, USA) is located downstream of the COP bypass pump to isolate the sample lines from pump-related pressure perturbations. All pumps are refurbished approximately once per year.

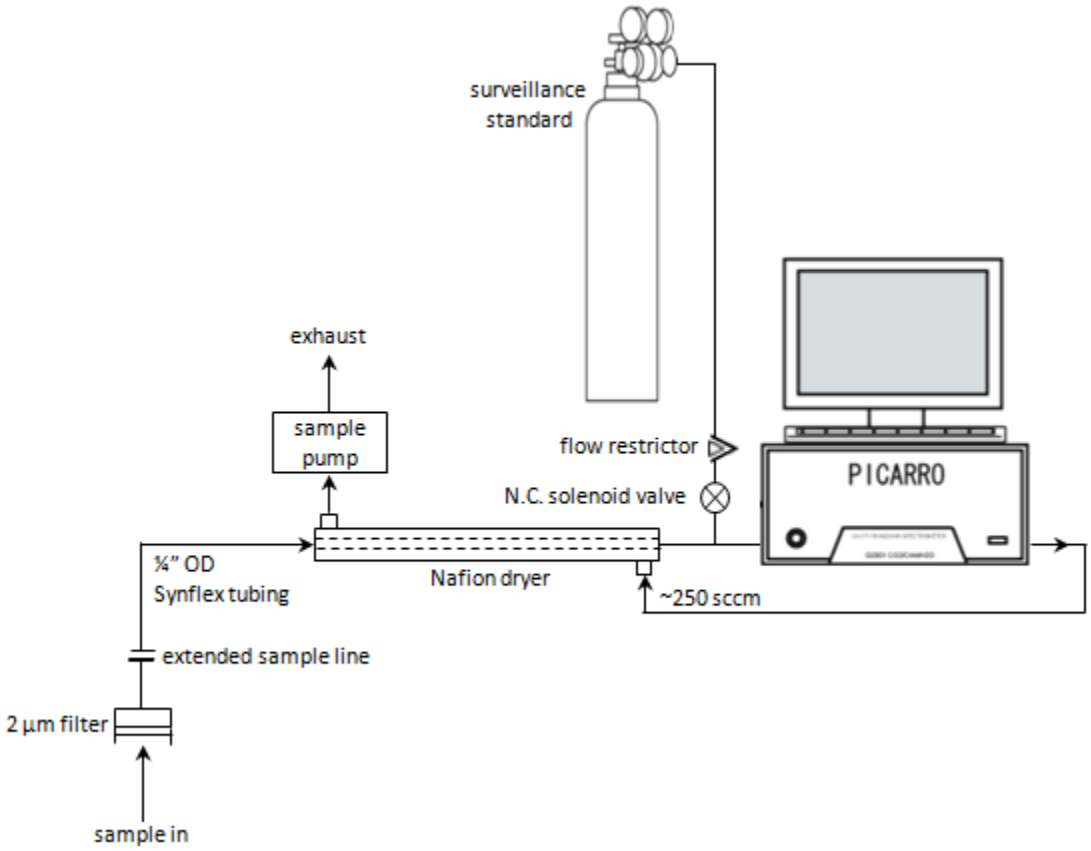

Figure 2-8. Flow diagram for the standard configuration in the Boston network.

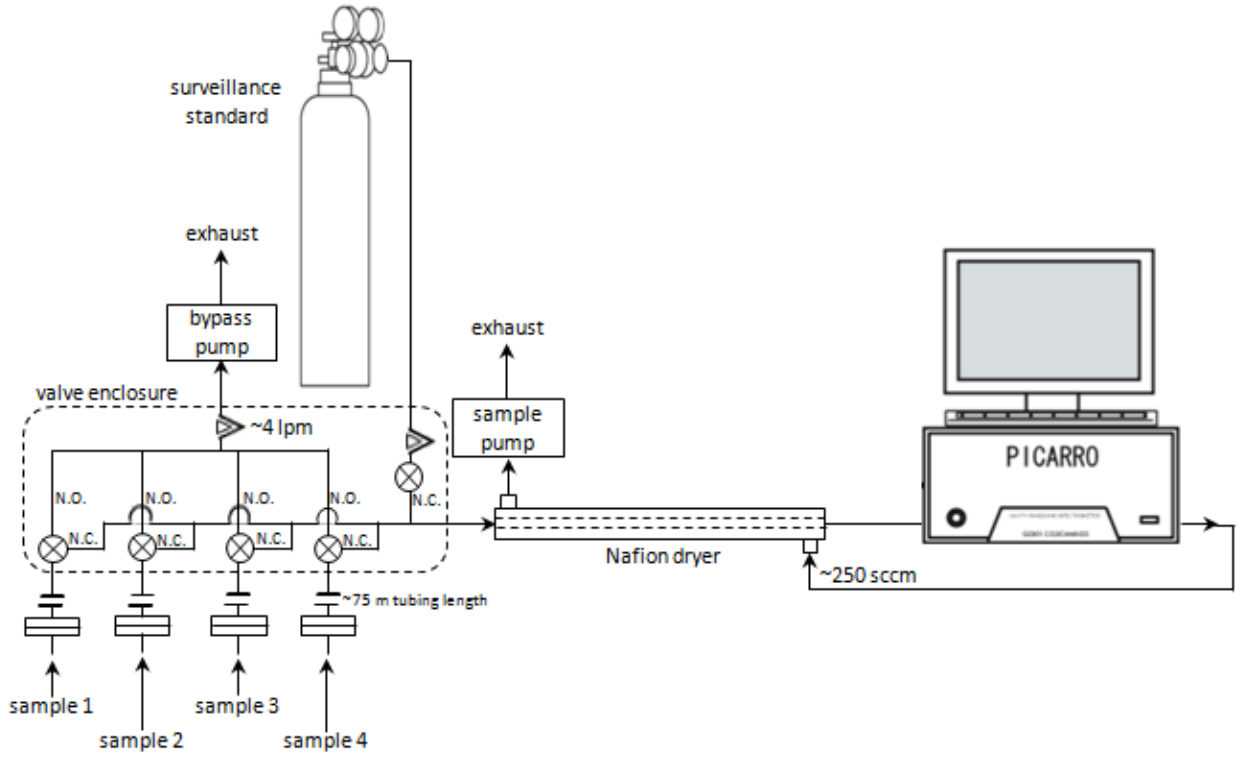

Figure 2-9. Flow diagram for the COP site with the four-corner sampling configuration.

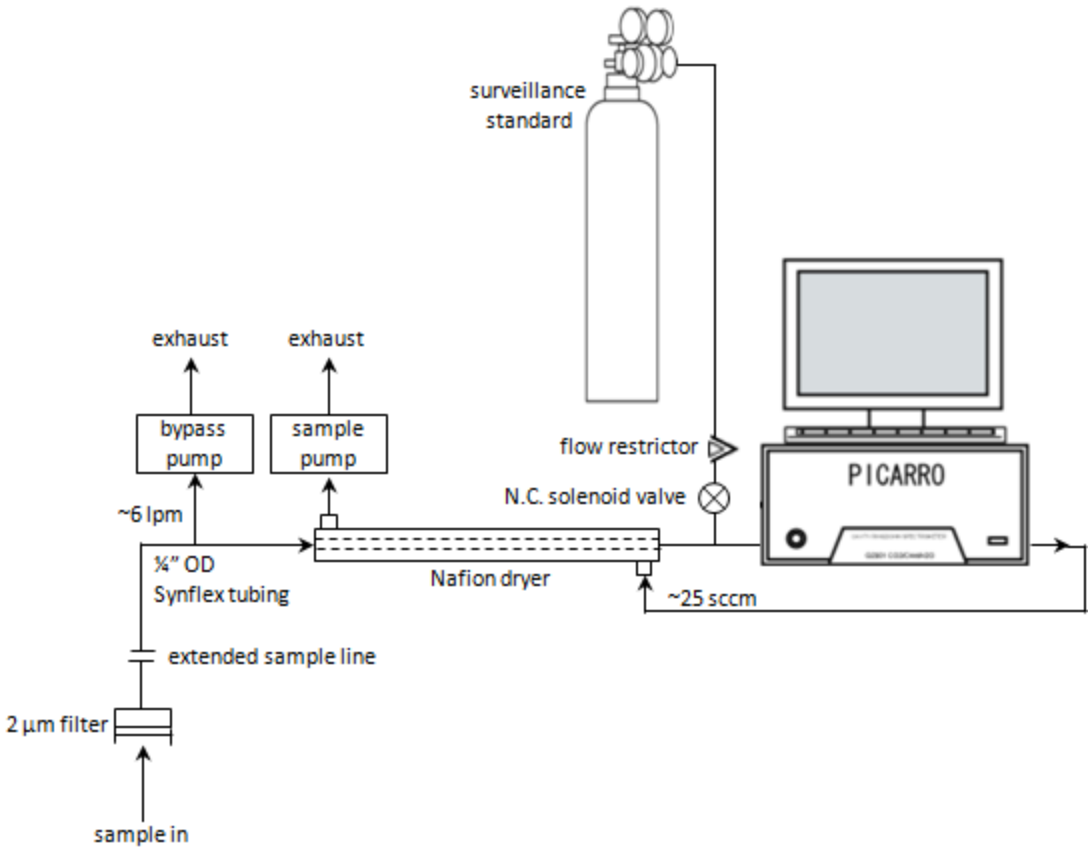

Figure 2-10. Flow diagram for the BU, UMB, and THI sites with Picarro G2101-i models, which have lower flow rates, and therefore an additional bypass pump compared to the standard configuration.

Measurement calibration

Calibration system

The primary goal of the network calibration system is ensure compatibility among measurements from all sites in the network, over time, within a quantifiable uncertainty range, and secondarily to trace measurements to the NOAA/WMO scale. Recommended measurement uncertainty (1σ) goals are ±0.1 ppm for CO_2 and ±2 ppb for CH_4 in well-mixed background air, and ±0.2 ppm CO_2 and ±5 ppb CH_4 (or ~5% of average enhancements) for regional studies with large enhancements (WMO 2014).

The response of the Picarro analyzers is highly linear so the network calibration system consists of the following two components: (i) a set of two calibration standards that span a range of concentrations is used to periodically (Table 2-2) calculate calibration equation slopes (gain), and (ii) regular frequent measurements of single ambient-level calibration standards ("surveillance standards", Table 2-3) fixed at each site are used to calculate calibration equation intercepts (offsets, null-values). All calibration and surveillance standards were manufactured by Scott-Marin (Riverside, CA, USA) using natural air (Nara et al. 2012) and were tied to scales defined by the NOAA Central Calibration Laboratory (www.esrl.noaa.gov/gmd/ccl/ccl.htm) with a laboratory-based Picarro.

Surveillance standards are measured at each site every 8 hours, in order to track instrument drift and help identify measurement problems. The interval of 8 hours was chosen to ensure that measurement variability due to diel changes in ambient conditions are captured. Surveillance gas is supplied to the sample line by actuating a two-way [stainless steel with Viton plunger seal and O-rings] solenoid valve (Figure 2-8; Gems Sensors & Controls, Plainville, CT, USA) using the Picarro-supplied valve controller software. Surveillance tank regulators (Scott Specialty or Airgas, two-stage, high-purity) are adjusted to meet the analyzer's flow demand plus ~50 sccm, and the excess surveillance gas is routed out the inlet. "Over-blowing the inlet" with the standard gas ensures that the surveillance measurement is never contaminated with sample air. Surveillance standards are measured for 4 minutes during each interval, and data from the first ~90 seconds are disregarded to ensure equilibration.

Table 2-2. Summary of all calibration activities to-date to compute each analyzer's response slope.

Analyzer	**Site**	**Date (DD-MM-YYYY)**	**Low-span (SN / CO_2 / CH_4)**	**High-span (SN / CO_2 / CH_4)**	**Location**
CFFDS2051	BU	2012-12-12	CC108731 / 387.73 / 1736.6	CC101254 / 415.06 / 2285.2	Field
CFFDS2051	BU	2014-06-27	JJ400 / 379.21 / 1707.8	JJ3616/ 413.69 / 2297.4	Field
CFADS2211	HF	2012-05-17	ND43187 / 381.44 / 1751.8	ND43208 / 409.20 / 2238.8	Lab
CFADS2211	HF	2012-12-13	CC108731 / 387.73 / 1736.6	CC101254 / 415.06 / 2285.2	Field
CFADS2211	HF	2014-05-30	JJ400 / 379.21 / 1707.8	JJ3616/ 413.69 / 2297.4	Field
CFHADS2008	HF	2014-06-06	JJ400 / 379.21 / 1707.8	JJ3616/ 413.69 / 2297.4	Field
CFADS30	NHT	2012-05-22	ND43187 / 381.44 / 1751.8	ND43208 / 409.20 / 2238.8	Lab
CFADS30	NHT	2012-12-11	CC108731 / 387.73 / 1736.6	CC101254 / 415.06 / 2285.2	Field
CFADS30	NHT	2014-05-29	JJ400 / 379.21 / 1707.8	JJ3616/ 413.69 / 2297.4	Field
CFADS30	BU	2014-07-24	JJ400 / 379.21 / 1707.8	JJ3616/ 413.69 / 2297.4	Field
CFKADS2033	COP	2012-05-17	ND43187 / 381.44 / 1751.8	ND43208 / 409.20 / 2238.8	Lab
CFKADS2033	COP	2012-12-12	CC108731 / 387.73 / 1736.6	CC101254 / 415.06 / 2285.2	Field
CFKADS2033	COP	2012-06-10	JJ400 / 379.21 / 1707.8	JJ3616/ 413.69 / 2297.4	Field
CFKADS2033	COP	2014-08-07	JJ400 / 379.21 / 1707.8	JJ3616/ 413.69 / 2297.4	Field
CFFDS2058	UMB	2012-12-13	CC108731 / 387.73 / 1736.6	CC101254 / 415.06 / 2285.2	Field
CFFDS2058	THI	2014-07-30	JJ400 / 379.21 / 1707.8	JJ3616/ 413.69 / 2297.4	Field

Surveillance tanks are replaced in the field before their pressure drops to ~500 psi, after which surface interactions on the cylinder walls can cause the CO_2 mixing ratio to change significantly within the tank (Daube et al. 2002). Pre- and post-deployment calibrated values of all surveillance tanks that have come back from the field thus far have changed by $\leq$ 0.05 ppm

for CO_2 and ≤ 0.2 ppb for CH_4. Final surveillance values (Table 2-3) are assigned as the average of pre- and post-deployment calibrated values.

Table 2-3. Surveillance standard CO_2 and CH_4 values, and their locations and time periods of deployment.

Cylinder serial number	**CO_2 (ppm)**	**CH_4 (ppb)**	**Deployment site and dates**
CC106559	405.39	1856.4	BU, July 2012 – present
CC12741	400.29	1861.6	HF, Aug 2012 – Jan 2014
CC73095	401.49	1895.5	HF, Jan 2014 – present
CC28253	401.26	1848.6	NHT, July 2012 – Feb 2014
CC56824	398.82	1896.5	NHT, Feb 2014 – March 2014
CC67195	401.75	1847.5	COP, July 2012 – Feb 2014
CC50695	397.97	1867.4	COP, Feb 2014 - present
CC497	398.75	1842.6	UMB, Aug 2012 – Aug 2013 THI, Oct 2013 – present

Calibration results

Calibration slopes are linearly interpolated to approximate drift over time. The impact of drift in slopes on corrected CO_2 and CH_4 over a range of values is shown in Figure 2-11. Except for analyzer CFFDS2051, the performance of which was known to have degraded, slopes drifted by <0.1 ppm up to ~450 ppm CO_2 and by <2 ppb up to 2600 ppb CH_4. Data from sites with more than two slope re-calibrations (HF and COP) demonstrate that drift was not unidirectional over the long term, and that more frequent calibrations did not necessarily lead to smaller slope drifts being captured (Figure 2-11).

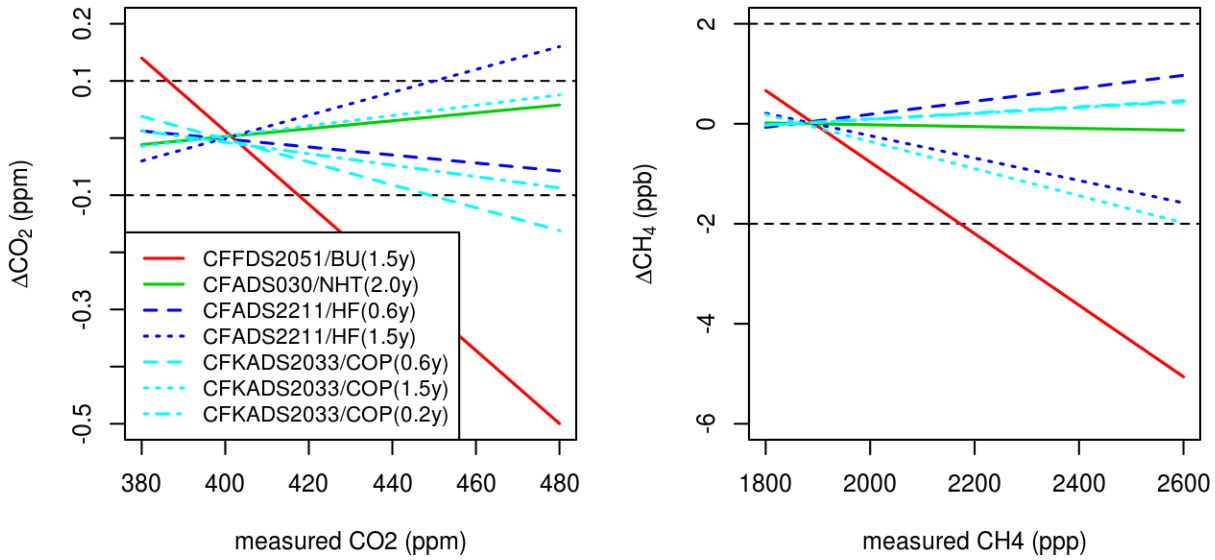

Figure 2-11. Impact of changes in calibration slopes on CO_2 and CH_4 corrections, over a range of values, for various analyzers, sites, and re-calibration intervals. Values of zero drift on the y-axis intersect with surveillance tank values on the x-axis.

Surveillance measurements are fit with a smoothed polynomial (fsmooth.Pspline function in R) with an ~15 day smoothing window (Figures 2-12 and 2-13), which is used to apply an offset correction to the data. Drift in surveillance measurements was ~1.2 ppm CO_2 per year and 5-10 ppb CH_4 per year for analyzer CFFDS2051, and <0.3 ppb CO_2 per year and <3 ppb CH_4 per year for all other analyzers. Computed drift from the surveillance measurements depends on the exact time-period of interest and the fidelity of a linear approximation to the observed changes in the surveillance measurements.

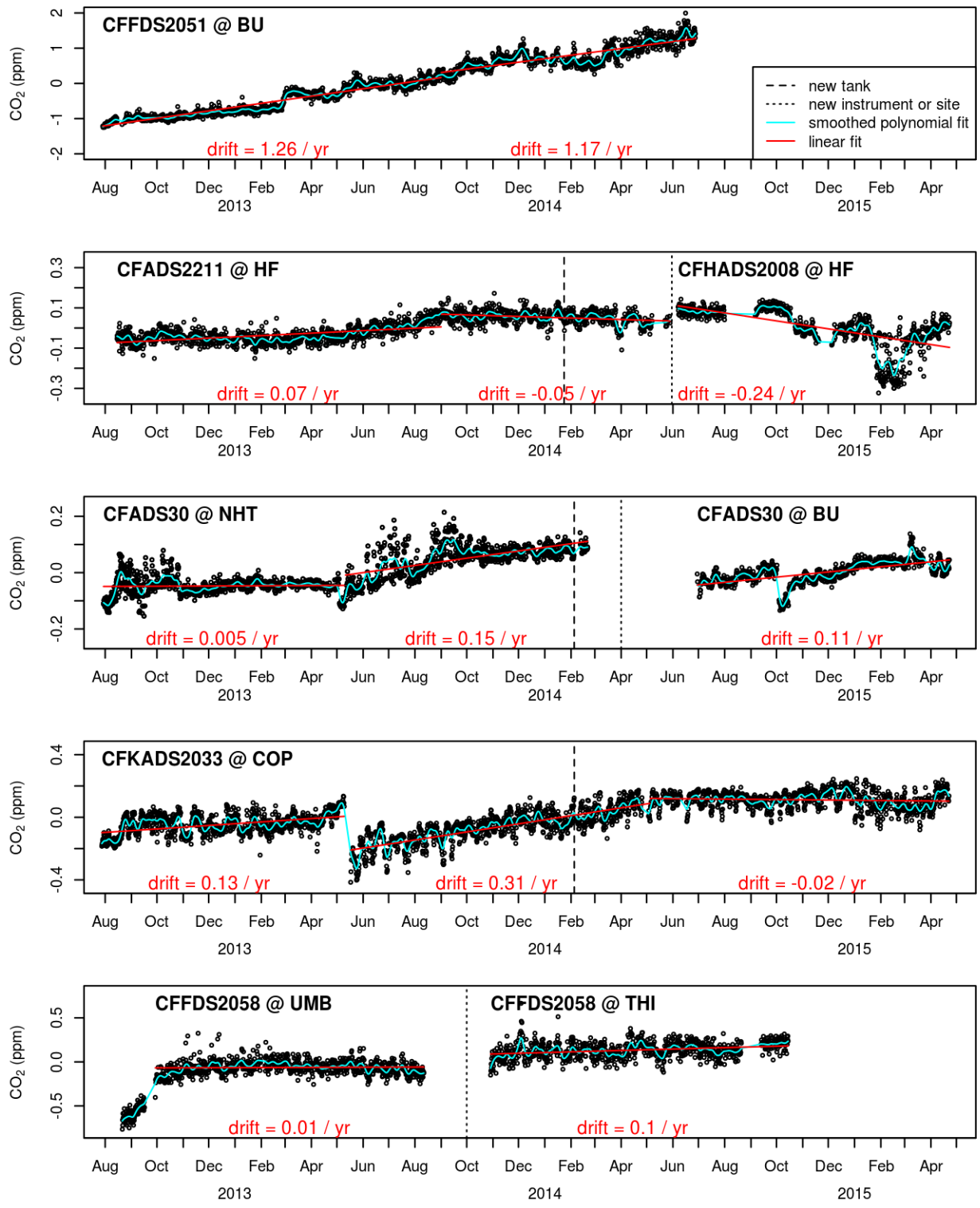

Figure 2-12. Average offset between true and measured surveillance values of CO_2 (black points), a smoothed polynomial fit to the points (cyan lines), and linear approximations of measurement drift rates for individual analyzers, sites, over approximately one-year time periods. Plots were shifted to have zero means to aid visualization of drift. Vertical dashed lines indicate when new surveillance standards or analyzers were installed.

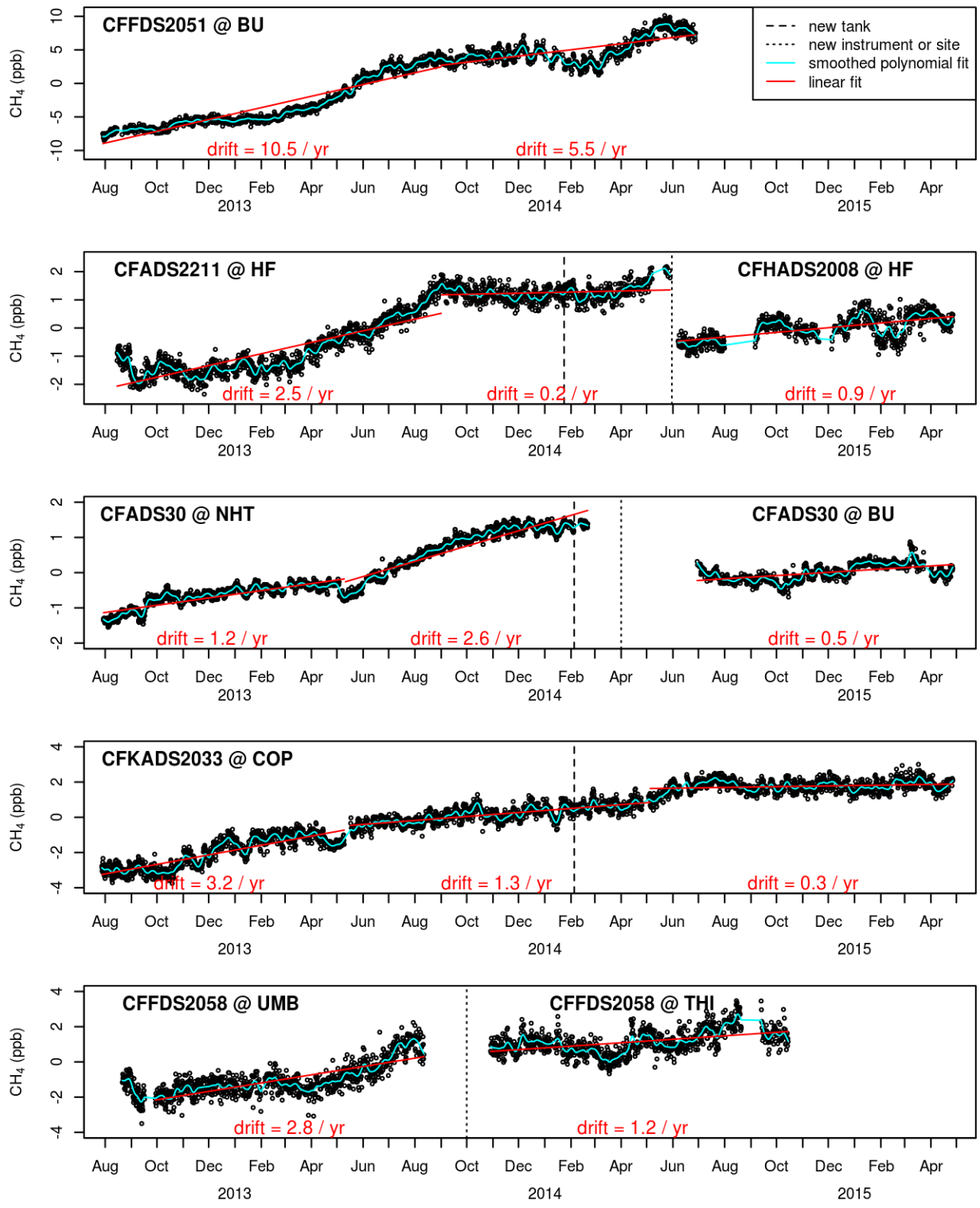

Figure 2-13. Average offset between true and measured surveillance values of CH_4 (black points), a smoothed polynomial fit to the points (cyan lines), and linear approximations of measurement drift rates for individual analyzers, sites, over approximately one-year time periods. Plots were shifted to have zero means to aid visualization of drift. Vertical dashed lines indicate when new surveillance standards or analyzers were installed.

Short-term drift can be computed as the change between individual surveillance measurements. Such an analysis demonstrates that uncertainty (1σ) due to short-term drift has been ~0.3 ppm $CO_2 \cdot day^{-1}$ for the model G2101-i analyzers (CFDS2051 and CFFDS2058) and ~0.1 ppm $CO_2 \cdot day^{-1}$ for all other analyzers (Figure 2-14). Short-term drift in CH_4 varies among analyzers between ~0.2 to ~1.6 $ppb \cdot day^{-1}$ (Figure 2-15). Short-term drift has been fairly consistent for individual analyzers over time, apart from the degradation of CFDS2051, and some seasonal patterns related to ambient temperature variability, indicating that such an analysis could be used to adjust the frequency of surveillance measurements (currently at 8 hours) according to uncertainty requirements. Uncertainty (1σ) in residual offsets are <0.1 ppm CO_2 and <0.5 ppb CH_4 for all analyzers over the full measurement period (Figures 2-16 and 2-17). The measurement precision of each analyzer, according to the in-situ surveillance measurements, is given in Table 2-4.

Table 2-4. Individual measurement precision, computed as the average standard deviation of the raw surveillance measurements made over the entire measurement campaign. A range is given for analyzer CFFDS2051 because its performance degraded over time.

Picarro	CO_2 (ppm)	CH_4 (ppb)
CFFDS2051	0.26 – 1.13	0.6 – 2.0
CFADS30	0.04	0.4
CFKADS2033	0.05	0.3
CFADS2211	0.04	0.3
CFHADS2008	0.03	0.3
CFFDS2058	0.40	1.1

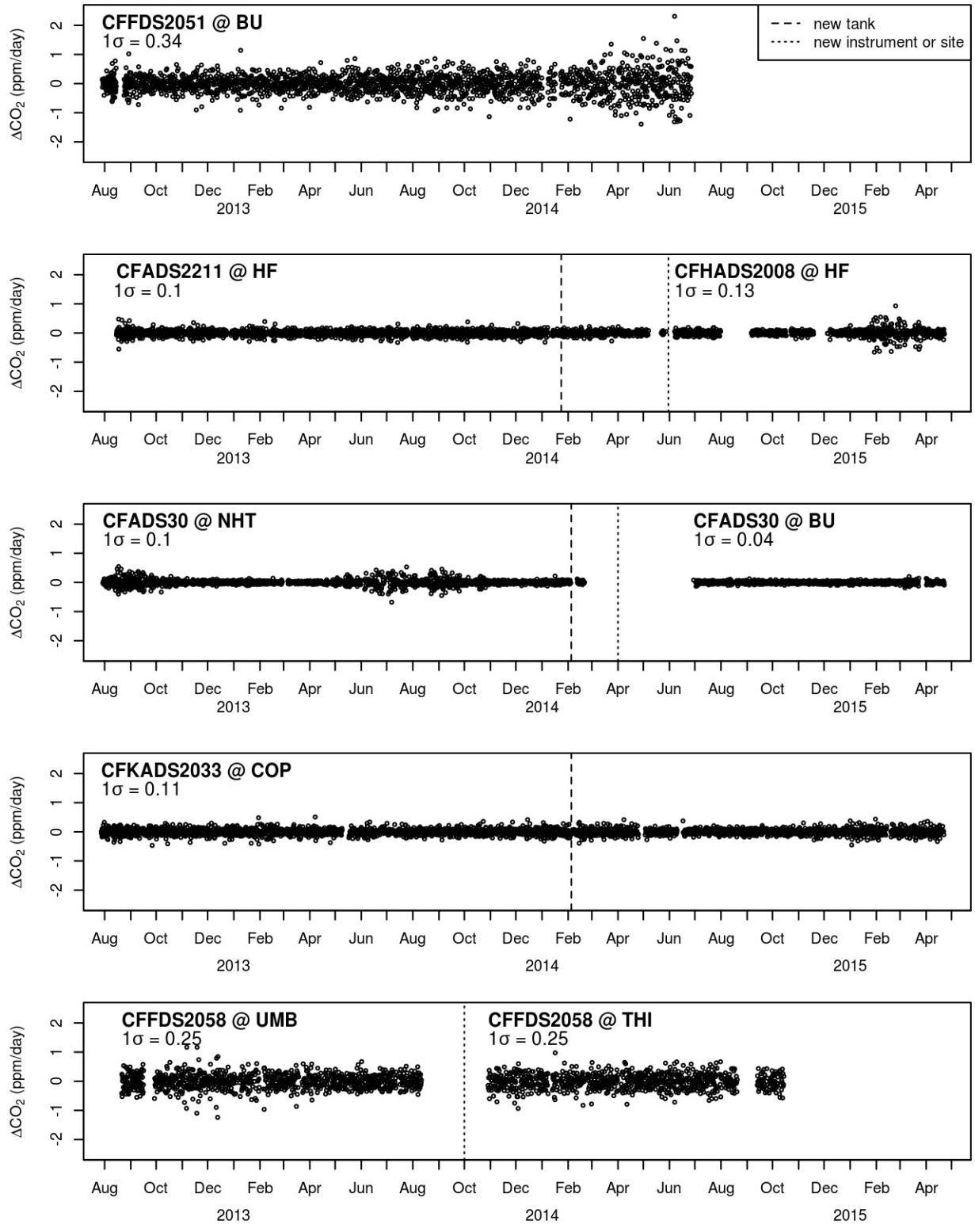

Figure 2-14. Point-to-point changes (ppm/year) in surveillance CO_2 measurements.

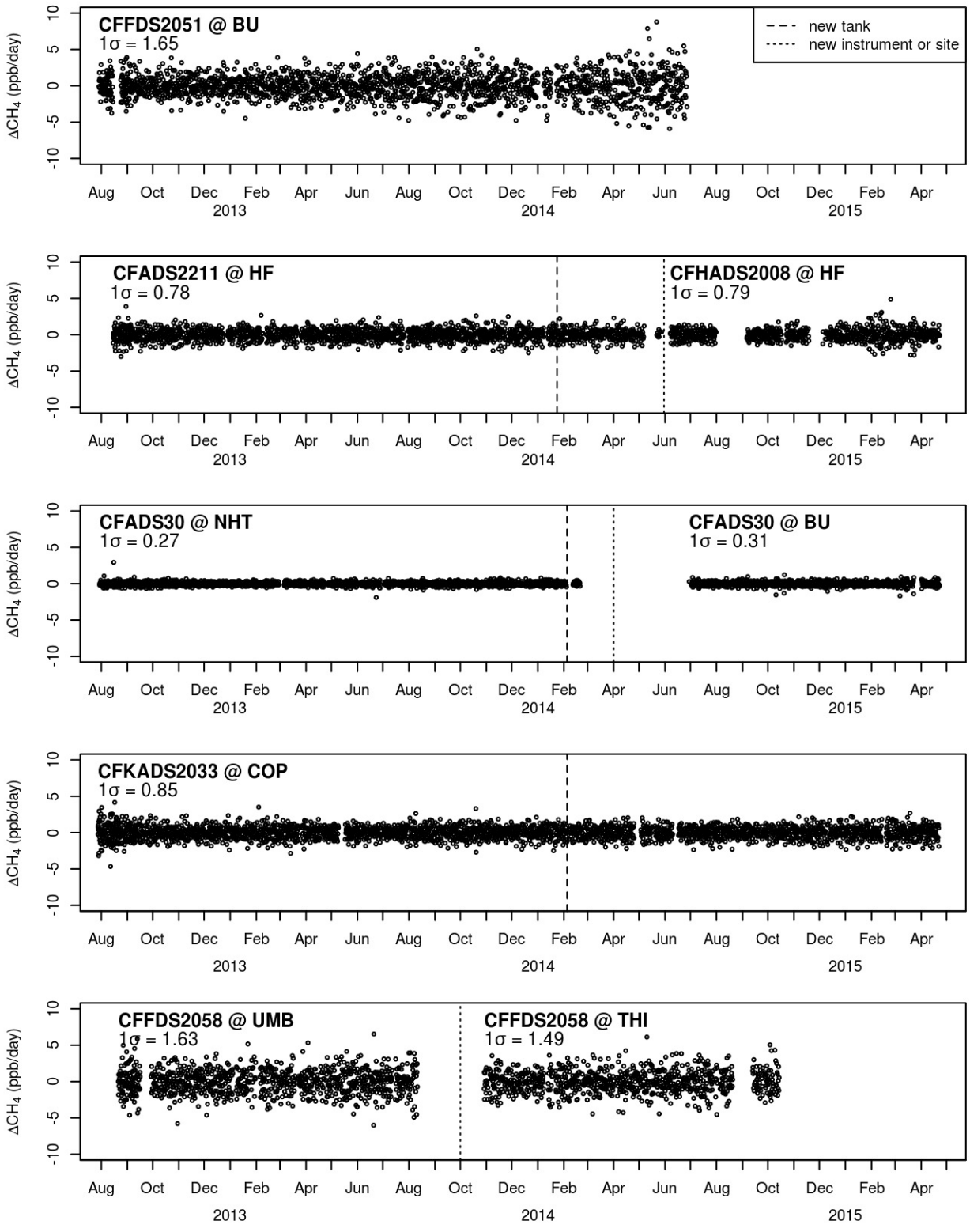

Figure 2-15. Point-to-point changes (ppb/year) in surveillance CH_4 measurements.

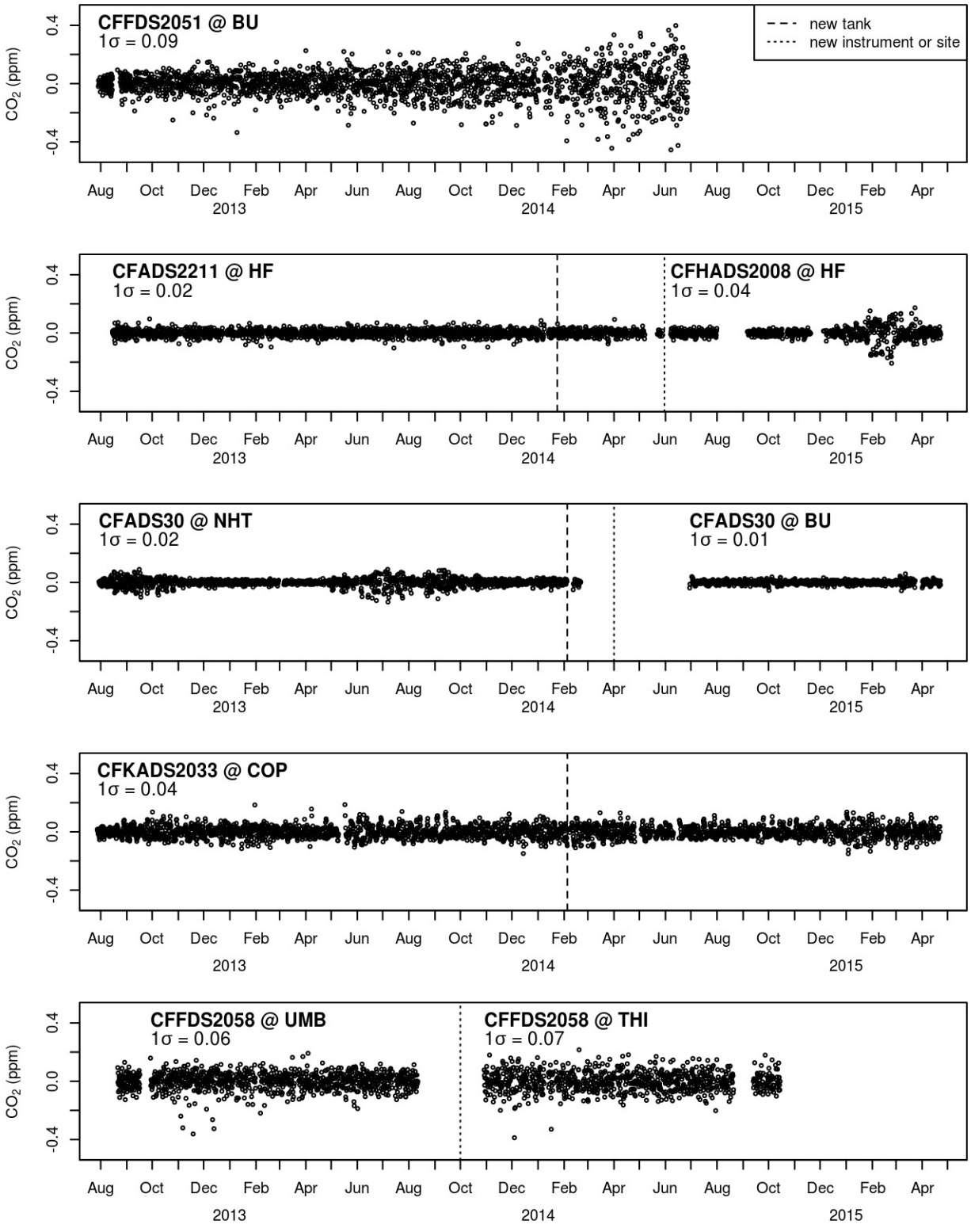

Figure 2-16. Residuals of the smoothed polynomial fits to average surveillance CO_2 measurements, and their standard deviation for individual analyzers and sites.

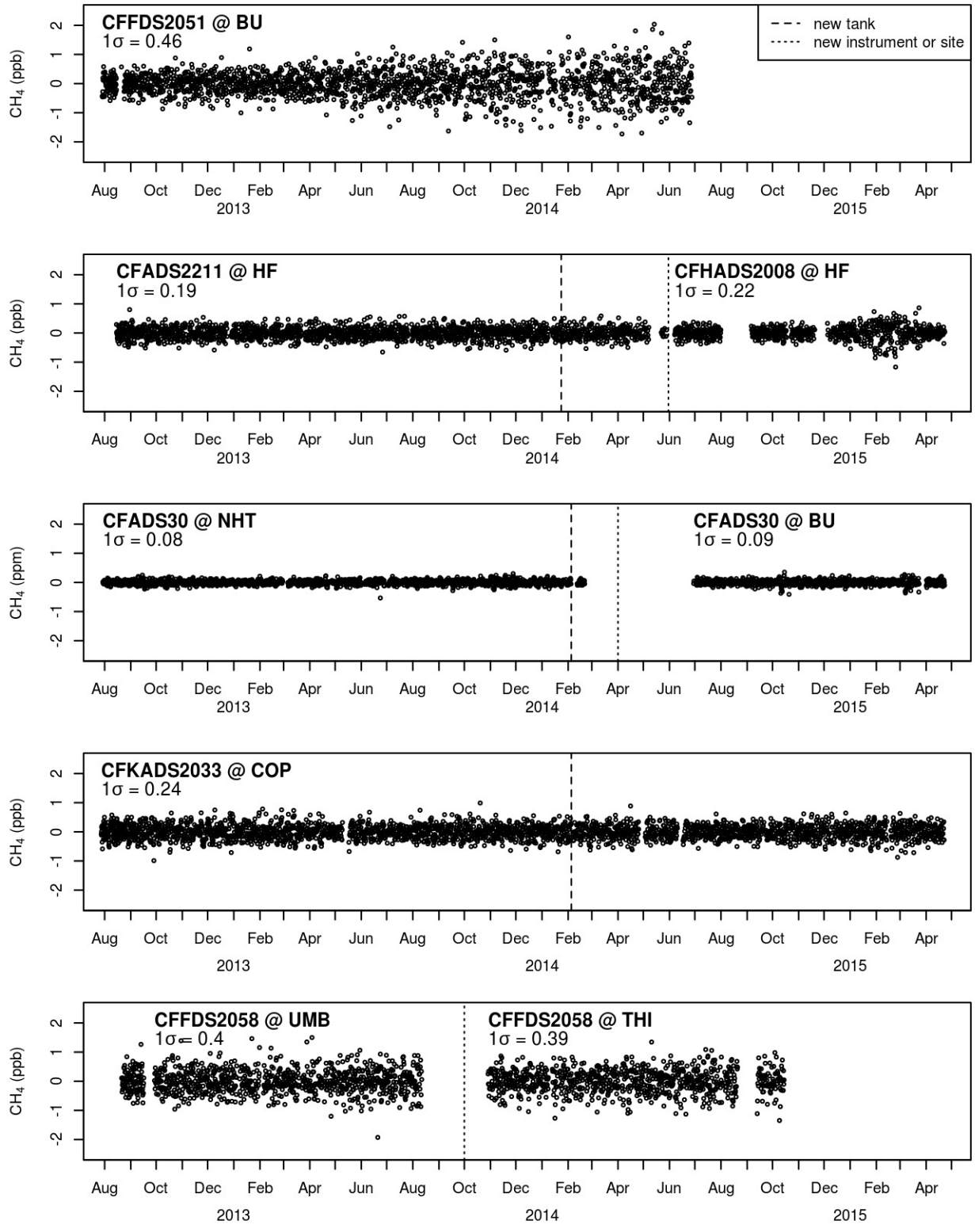

Figure 2-17. Residuals of the smoothed polynomial fits to average surveillance CH_4 measurements, and their standard deviation for individual analyzers and sites.

Measurement water correction

Carbon dioxide and CH_4 measurements must be reported as dry-mole fractions, and this has traditionally been achieved by drying sample air prior to measurement, which requires additional equipment. The Picarro CRDS measures CO_2, CH_4, and H_2O with sufficient precision that an empirical H_2O-correction equation (which corrects for both dilution and pressure-broadening effects) can be used to convert CO_2 and CH_4 measurements made in ambient moist air to dry mole-fractions (Chen et al. 2010).

When the measurement network was initially setup in the summer of 2012, sample air was not dried and we planned to use a set of manufacturer-supplied H_2O correction equations to compute dry CO_2 and CH_4 mole-fractions from measured values. Later, we learned that the model G2101-i analyzer measures $^{12}C^{16}O_2$ at a different wavelength than the other Picarro models, in a region with direct spectral interference from $^{1}H^{2}H^{16}O$ ("semi-heavy water", Rella 2012), which is not directly reported by the analyzer and which can vary widely in the atmosphere (e.g. Richardson et al. 2012). Therefore, the general H_2O-correction equation (Chen et al. 2010) is not applicable to the G2101-i analyzers, and development of an effective empirical H_2O-correction for those analyzers is not feasible. The δD-dependent H_2O-correction equation given in Rella (2012) may be used in combination with an estimate of the possible range of δD to estimate the additional uncertainty associated with the HDO interference in the BU measurements prior to the installation of the dryer.

Furthermore, Rella et al. (2013) reported a survey and analysis of the performance of the general H_2O-correction equation across multiple analyzers operated by different labs over several years. The authors found that the general H_2O-correction equation could be reliably used to meet the highest measurement accuracy goals (±0.1 ppm CO_2 and ±2 ppb CH_4, WMO 2014)

only when ambient H_2O levels were ≤ 1%. (Measured water vapor levels >3% are not uncommon for our network in the summer.) To improve the accuracy, the authors recommended that operators derive an H_2O-correction equation specific to each analyzer, and track changes in the equation over time (Rella et al. 2013).

For these reasons, we installed Nafion membrane dryers (MD-050-24, Perma Pure, Toms River, NJ, USA) at all sites in the network, beginning at BU in May, 2013. The dryers are integrated into the measurement system such that the warmer exhaust air from the analyzer is used as the counter-flowing purge gas (Figures 2-8 – 2-10). This system is effective for reducing H_2O levels in sample air to ≤ ~0.15%, with some seasonal variability.

Lab-derived correction equations

To improve the accuracy of the data collected prior to the installation of the Nafion dryers, instrument-specific H_2O-correction equations were measured for each analyzer in the summer of 2014 using the laboratory setup depicted in Figure 2-18. The goal of the setup was to provide the analyzer with alternating intervals of moist and dry air, at a range of H_2O values, while holding the CO_2 and CH_4 mole fractions constant. To achieve this, we first humidified air from a standard tank with no CO_2 or CH_4 ("zero air") with a dew point generator (LI-610, Li-Cor, Lincoln, NE, USA), and then mixed the moist zero air with air from a second standard tank with high CO_2 and CH_4 concentrations, in order to achieve approximately ambient CO_2 and CH_4 concentrations in the resulting mixture. We elected to not directly moisten a standard gas that contained CO_2 because CO_2 solubility in the water reservoir of the dew point generator made it difficult to achieve stable CO_2 concentrations in the humidified sample. Ambient-level humidified air was then split into two streams, one of which was dried via a Nafion-membrane

dryer followed by a cold-trap with dry ice. The sample stream fed to the analyzer was switched between wet and dry streams via a three-way solenoid valve (Figure 2-18).

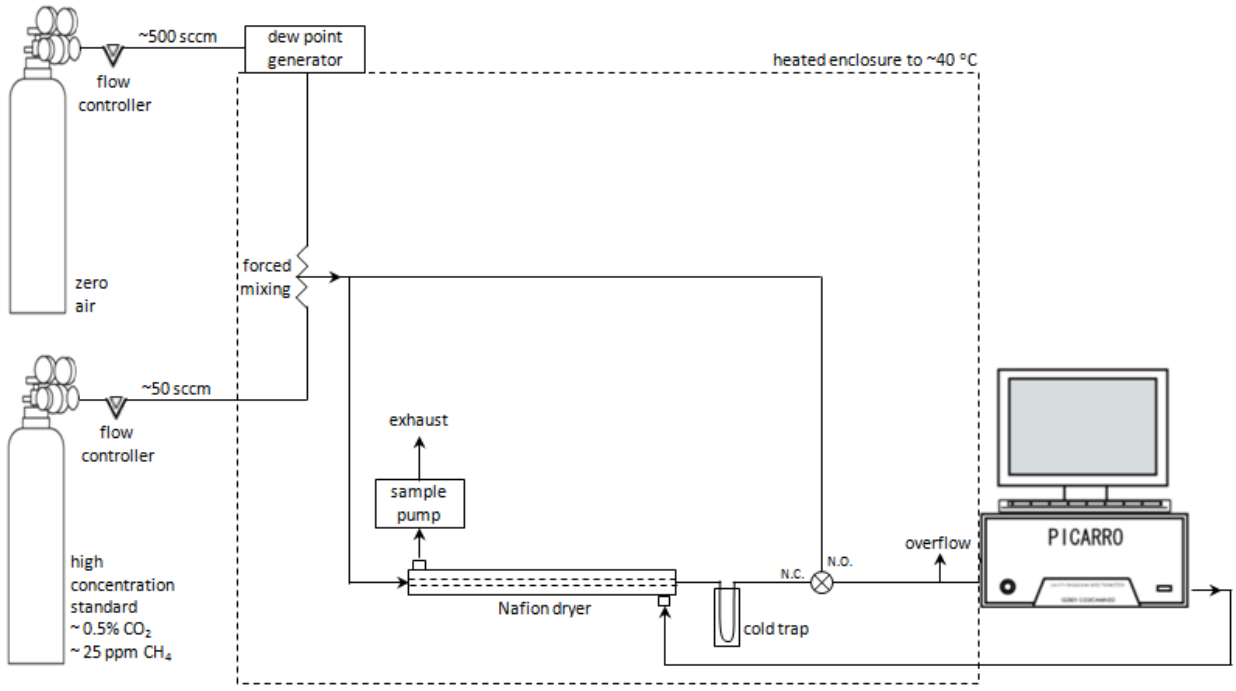

Figure 2-18. Schematic of the laboratory setup for deriving empirical H_2O-correction equations for each Picarro analyzer.

An example timeseries of measurements of alternating humidified and dry sample streams and the resulting H_2O-correction equations derived for one analyzer is shown in Figure 2-19. Empirical H_2O-correction equations are represented as quadratic fits with the following form:

$$\frac{CO_{2,wet}}{CO_{2,dry}} = 1 + aH_2O + bH_2O \qquad (2-1)$$

$$\frac{CH_{4,wet}}{CH_{4,dry}} = 1 + cH_2O + dH_2O \qquad (2-2)$$

The coefficients for Equations 2-1 and 2-2 computed for each analyzer are given in Table 2-5. It is important to note that the parameter used for the H_2O term in Equations 2-1 and 2-2 must be

explicitly specified. The equation from the literature (Chen et al. 2010, Rella et al. 2013) uses the "h2o_reported" parameter, but this parameter is not consistently labeled in the data files output by the analyzers in our network due to their many vintages and models. Our analyzer-specific corrections were derived using the parameter labeled "H2O" in the data files from each analyzer, although the corrections applied by the Picarro software to yield the "H2O" values may not be identical among all analyzers.

Table 2-5. Empirical H_2O-correction coefficients from Equations 2-1 and 2-2 computed for each analyzer and given in the literature.

Analyzer	**a**	**b**	**c**	**d**
CFFDS2051	-1.62×10^{-2}	3.46×10^{-4}	-8.932×10^{-3}	-2.38×10^{-4}
CFADS2211	-1.65×10^{-2}	3.43×10^{-4}	-1.294×10^{-2}	5.78×10^{-5}
CFHADS2008	-1.71×10^{-2}	3.97×10^{-4}	-1.335×10^{-2}	4.64×10^{-5}
CFADS030	-1.28×10^{-2}	2.16×10^{-5}	-9.957×10^{-3}	-1.28×10^{-4}
CFKADS2033	-1.59×10^{-2}	2.26×10^{-4}	-1.259×10^{-2}	9.74×10^{-5}
Chen et al. 2010	-1.20×10^{-2}	-2.67×10^{-4}	-9.823×10^{-3}	-2.39×10^{-4}

The impact of the lab-derived H_2O-correction equations, compared to the manufacturer-provided correction equations, on hourly average dry CO_2 and CH_4 values, measured over several months at the field sites, is depicted in Figure 2-20. Over a broad range of H_2O, CO_2, and CH_4 values, differences are $\leq$ ~0.4 ppm for CO_2 and $\leq$ ~2 ppb for CH_4, except for analyzer CFFDS2051, for which the CH_4 difference is as large as 7 ppb at high H_2O levels, likely due to the analyzer's degraded performance by the time the H_2O-correction was computed. Correction equations were not computed for CO_2 for the model G2101-i analyzers and for analyzers that were only deployed with Nafion dryers. Because H_2O-corrections were not re-computed throughout the measurement period to track potential drift, comparison of our lab-derived and the manufacturer-provided corrections (Figure 2-20) likely offers the most conservative portrayal of the associated uncertainties.

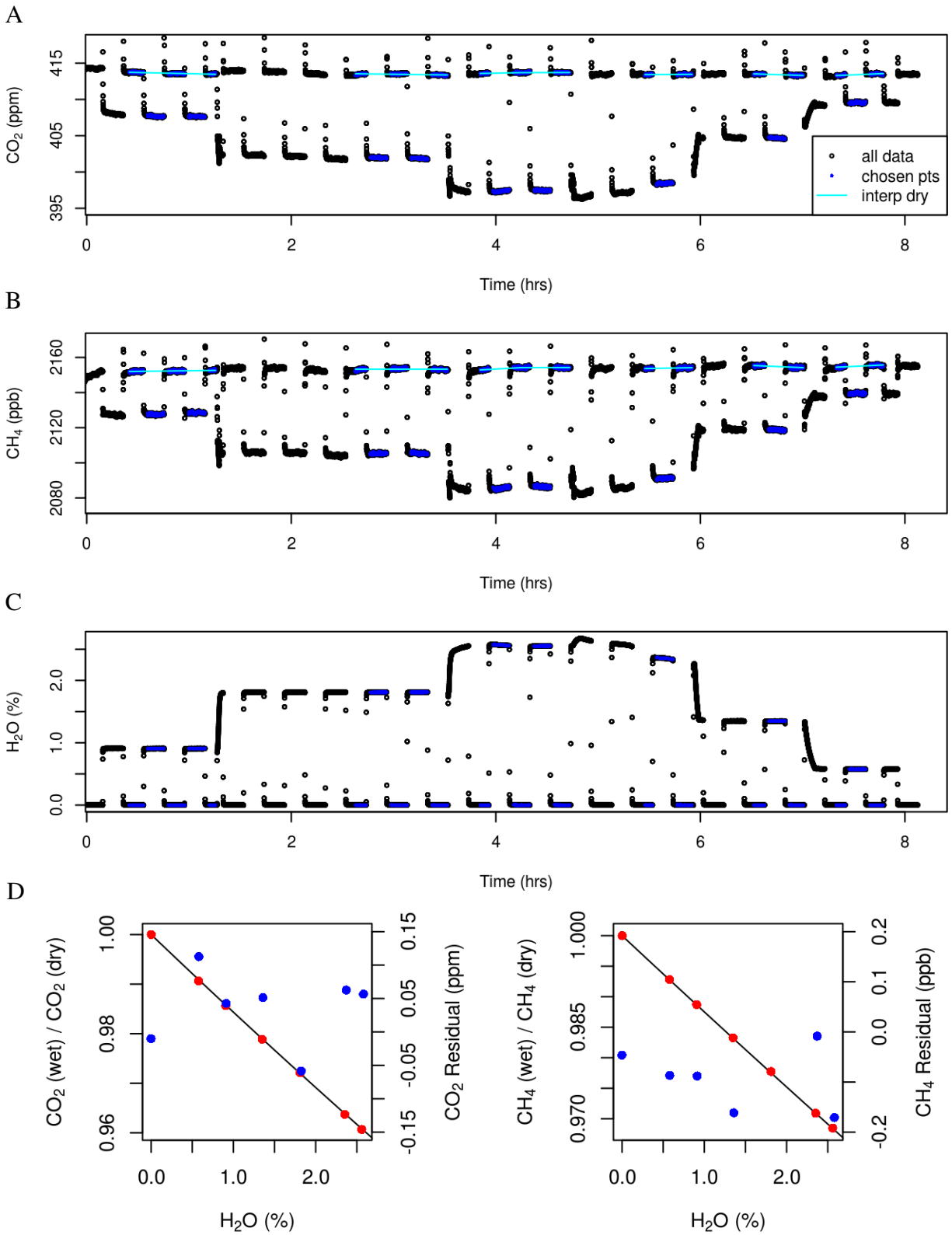

Figure 2-19. (A-C) Example of CO_2, CH_4, and H_2O measurements used to derive the (D) H_2O-correction equations, represented as quadratic fits to red points, for analyzer CFKADS2033. Residuals are shown as blue points and correspond with the right y-axis.

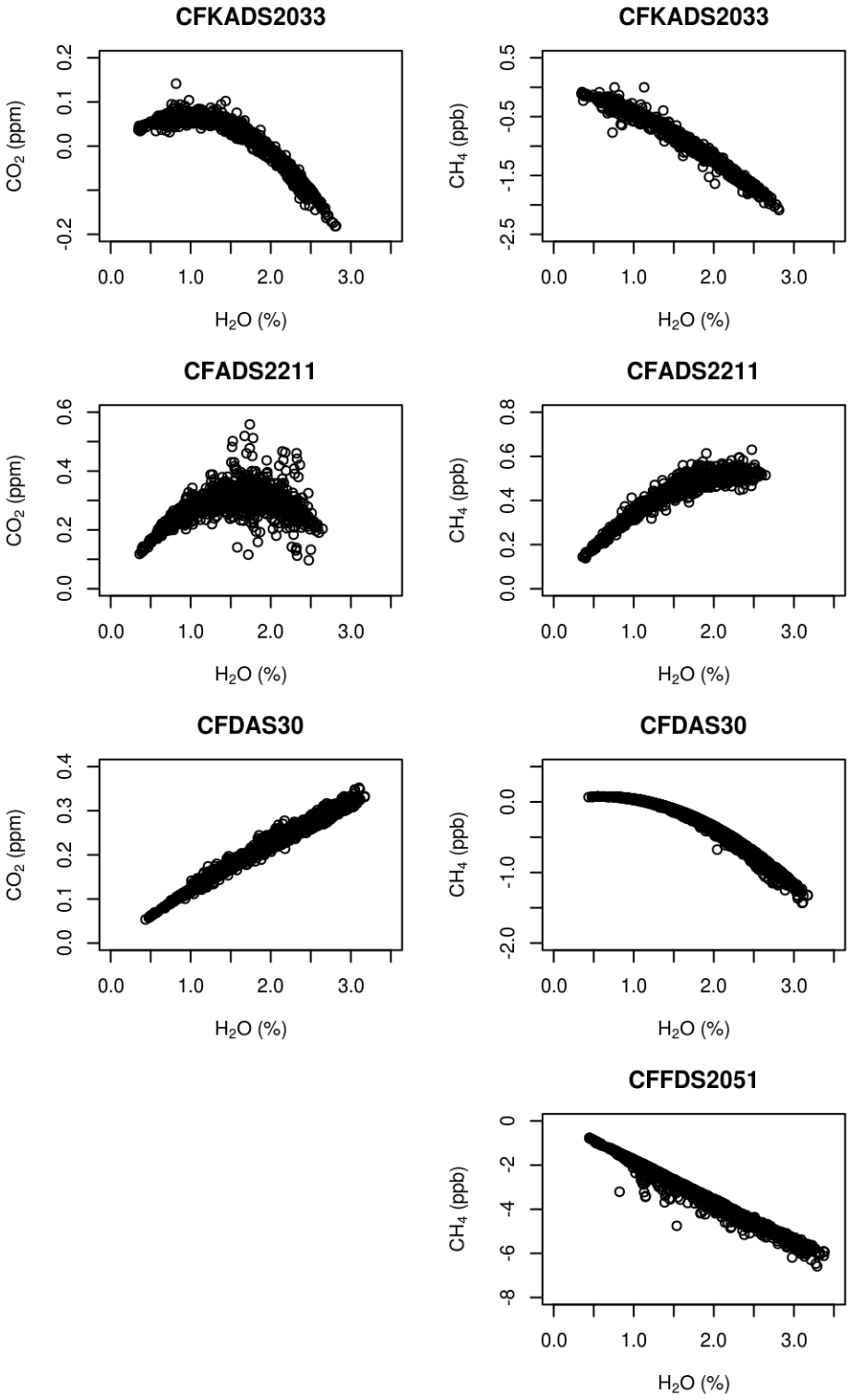

Figure 2-20. Hourly average difference between analyzer-reported and lab-derived dry CO_2 and CH_4 values, versus hourly average H_2O, measured by the five analyzers in the field during August – October, 2012. Data for CFADS2211 are slightly noisier because of the large and rapid concentrations changes associated with the vertical profile measurements at HF.

Computer configuration for remote operation and data acquisition

Reliable remote and longterm operation of the network is aided by several software programs that we installed on the Picarro computers, all of which have DSL connections to the internet. We use remote desktop software (TeamViewer), configured to start automatically with Windows, to remotely log into the Picarro computers. This capability is particularly useful for restarting computers and cycling power (by executing the Picarro program, "ResetAnalyzer.exe"), which is often effective for resolving generic problems with the measurement software. A network time protocol software (Meinberg, www.meinbergglobal.com/english/sw/ntp.htm) continuously syncs the computer clock with NIST time servers to prevent drift, which can otherwise become significant over time. In general, it is important minimize the number of additional programs (e.g. anti-virus software) running on the Picarro computers, and to monitor the CPU usage of new programs, because the Picarro control and measurement software may perform sub-optimally when processing capacity is reduced.

Data files are automatically and continuously copied from the Picarro Windows computers to a Linux file server at Harvard using the following system. First, the Picarro file, "Archivere.exe", is configured to direct compressed copies of each new data file to a backup directory on the Picarro computer. Next, a batch script is run each hour by the Windows task scheduler, which uses the Robocopy command to sync the backup directory with a Dropbox folder that is also synced on the Linux server at Harvard. On the Harvard Linux server, a bash script is run daily from the crontab, which copies the contents of the Dropbox folder to a data archive using the rsync command. This system for remote data acquisition has several safeguards and redundancies to prevent data loss upon failure of any individual component, and has been

reliable since the network began. The Picarro Archiver.exe file is also configured to delete data files that are older than ~1.5 years to prevent the analyzer hard disk from becoming full, and to delete backup data files that are older than ~2 months, which keeps the Dropbox folder at a steady size.

Data QA/QC and processing

We developed a set of programs written in R (www.r-project.org) for routine end-to-end data processing and to help identify operational problems. The processing code is designed to operate on data from individual sites and days, and then to merge final datasets from all sites into one dataset. Currently, the processing code must be executed by a user (based on the reasoning that this encourages the user to visually inspect the data at that time), but a routine could easily be implemented to automatically process the network data each day.

The level-one processing code performs the following steps: it reads-in and appends the raw data files; flags data during pre-recorded maintenance events or when operational parameters were out of range; accounts for time delays in the sampling lines where applicable; applies H_2O-corrections and then calibrations slopes to the raw measurements; separates out data when surveillance standards were flowing and writes surveillance measurement statistics to a separate file; plots raw data and operational parameters (Figure 2-21); and writes the level-one processed data to individual files for each site and day.

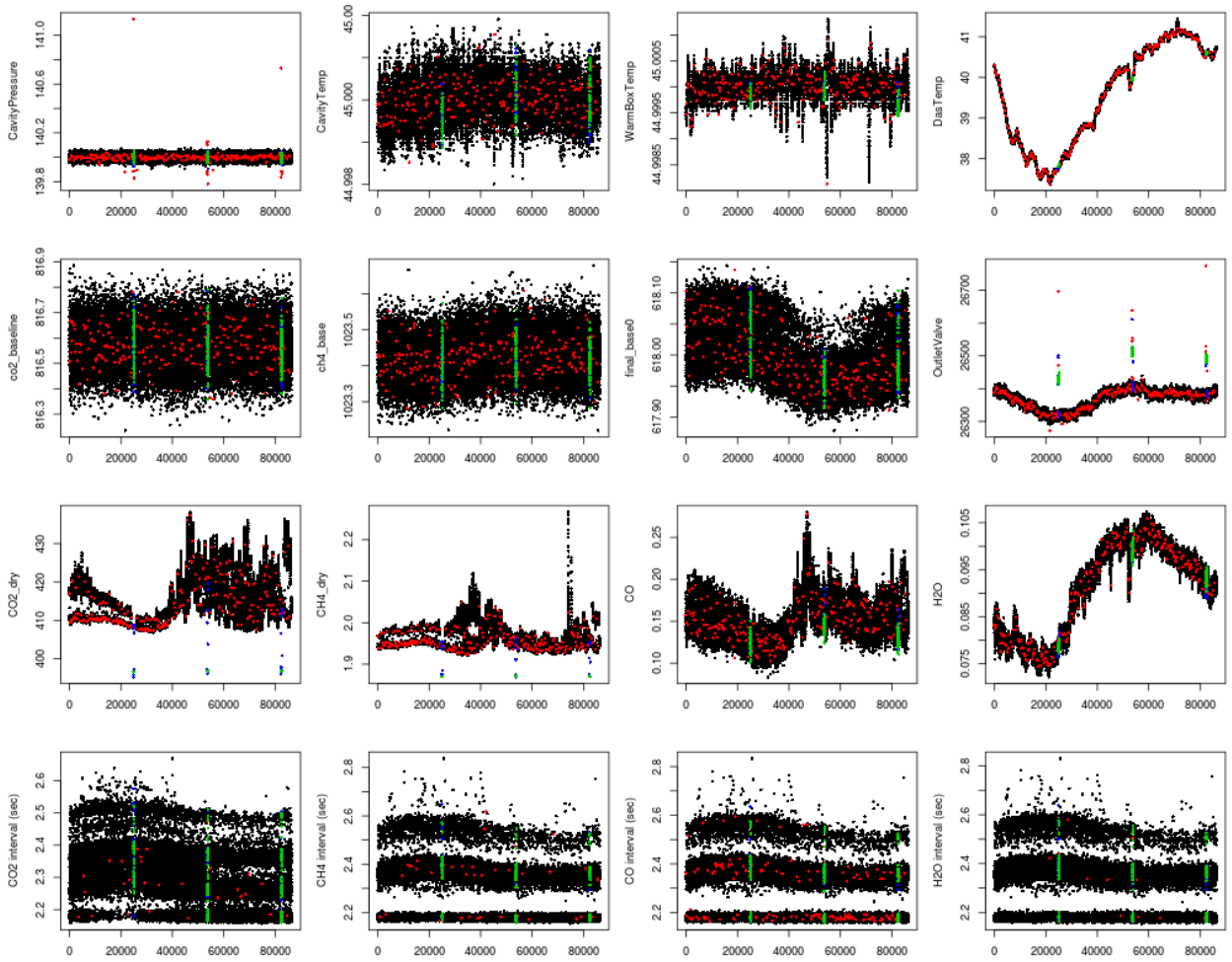

Figure 2-21. An example of the data plots that are generated for each day and site by the level-one processing code to visually inspect the data and identify operational issues. This particular plot is for the COP site on April 14, 2015. The top row of plots shows analyzer pressures and temperatures; the second row shows spectral baselines and the position of the analyzer flow control valve; the third row shows measured concentrations; and the last row of plots shows measurement intervals for each species. Red points are flagged data points, and blue and green points show when the surveillance standard was flowing, where blue represents non-equilibrated values and green points are used to calculate mean surveillance values. In this case, the dappling of red flagged points is due to the opening and closing of solenoid valves for the corner-sampling regime. Note the small perturbation in cavity pressure (upper-left panel) when the surveillance tank was sampled, due to the small pressure differential between the sample and surveillance lines.

The level-two processing code performs the following steps: reads-in daily files output by the level-one code from all sites; applies smoothed surveillance offsets; indentifies the profile level corresponding to each data point from HF; selects the corners with the lowest CO_2, CH_4,

and CO values in each 20-minute 4-corner sampling cycle in the COP dataset; computes five-minute and hourly averages from the fully filtered and corrected datasets; merges the hourly data from all sites into a single file; writes the fully-corrected datasets to data files that will be archived; and creates a daily summary plot showing the merged, HF profile, and COP-corners data (e.g. Figure 2-22).

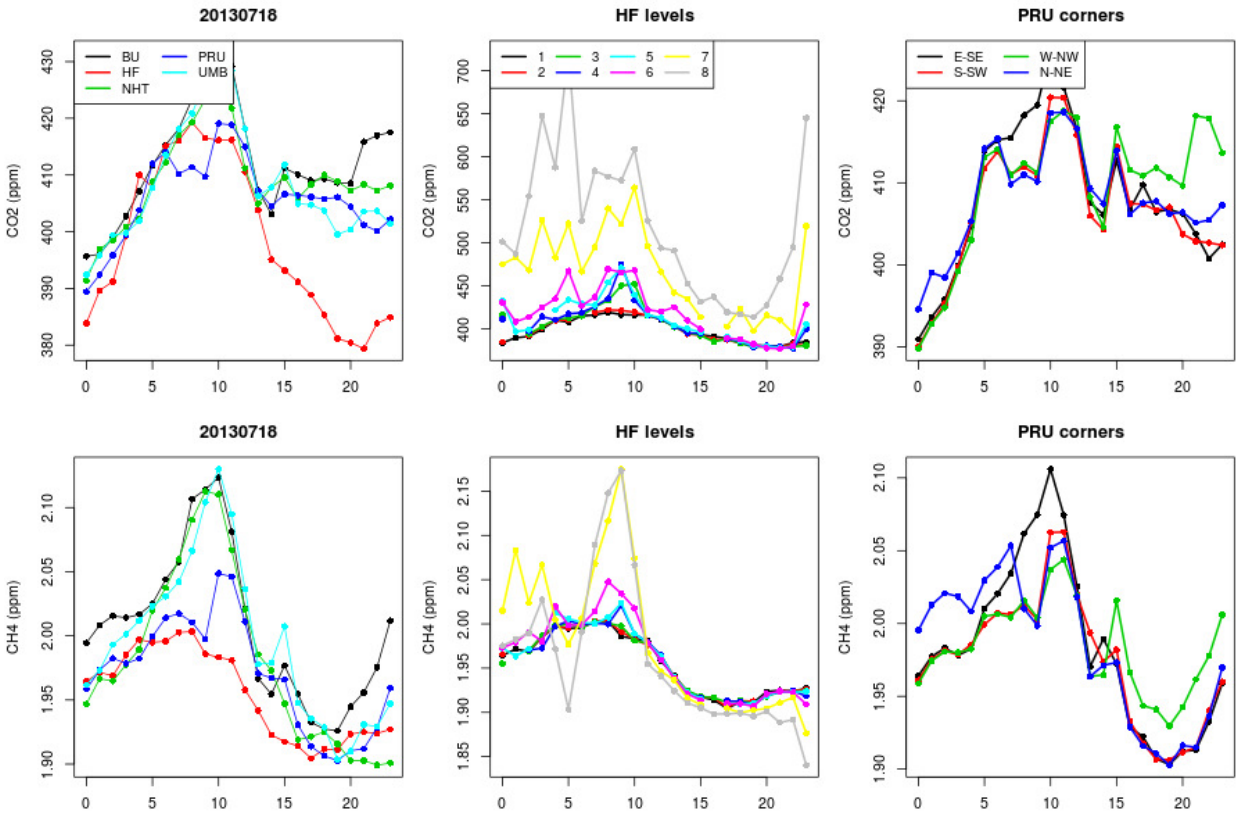

Figure 2-22. Example of the daily data plot generated by the level-two processing code of hourly average measured CO_2 (top-row) and CH_4 (bottom-row) at all sites (left column), HF at the eight sample heights (middle column), and at COP at the four corners (right column).

Operational problems and resolutions

During the nearly three years of operating the Boston network, we have learned many lessons about common operational and instrument problems, their symptoms, and strategies for resolving them. The most common problems are mechanical failures of sample pumps

(frequency ~1 year) and fans located throughout the Picarro analyzer, including in the enclosure, warmbox, and hotbox. Symptoms of such failures appear as loss of cavity pressure control, in the case of a failed sample pump, and poorer temperature control of the warmbox and/or hotbox, in the case of broken fans. Failure of computer components, such as the hard disk or processor fans, are common, but can be difficult to diagnose as they may appear as problems with the measurement software. The following sections describe specific problems encountered in more detail.

Degradation of analyzer CFFDS2051

The measurement quality of the CFFDS2051 analyzer located at BU progressively diminished throughout its deployments, as indicated by the unusually large instrument drift (Figures 2-11 – 2-13), increasing short-term drift (Figure 2-14 and 2-15), and larger measurement uncertainties (Figure 2-14 and 2-15), including from the H_2O-correction equation (Figure 2-20). Additional indicators of measurement degradation, namely increases in surveillance measurement standard deviations, means and variances in spectral baselines, and measurement intervals, are shown in Figure 2-23. Drift was observed in parameters related to both CO_2 and CH_4, although some variables began drifting much earlier than others. Large drift in all variables appears to have commenced in February, 2014. The analyzer was replaced in June, 2014 and sent back to the manufacturer. The source of the problem was not definitively determined, but possibilities include a contaminated cavity, spectral interference, or misalignment of the wavelength monitor. The slow decline of the instrument is inconsistent with the hypothesis of cavity contamination.

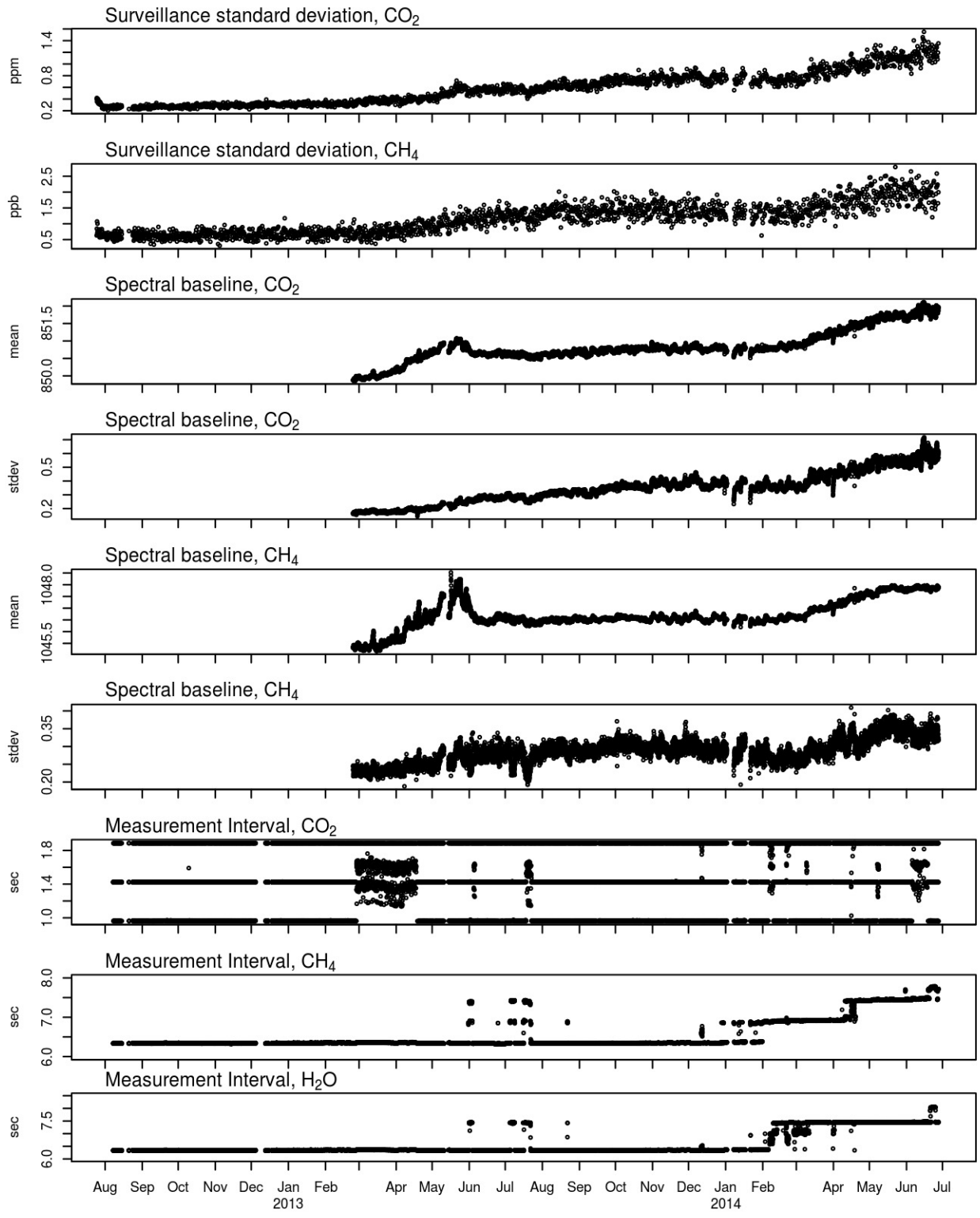

Figure 2-23. Timeseries of hourly averages and standard deviations of parameters from analyzer CFDDS2051 at BU.

Cavity pressure variance

Pressure stability of the optical cavity is essential for stable measurements. The impact of increased cavity pressure variation on measurement precision is demonstrated by Figure 2-24. We have observed transient increases in cavity pressure variability on multiple analyzers, but have been unable to reproduce the effect or correlate it with an external forcing, such as vibrations or pressure fluctuations in the ambient environment. Increased cavity pressure noise was observed on CFADS2211 at HF in May, 2014; on CFFDS2058 at UMB prior to April, 2013; on CFKADS 2033 at COP in April of every year; and on CFADS30 at BU in the fall of 2014 and spring of 2015. Numerous attempts to resolve the issue by replacing the sample pump were unsuccessful. Changing the particle filter at the inlet of the CFFDS2058 unit resolved the issue at UMB, but the solution was unsuccessful on the other units. The pressure of the optical cavity is controlled by a proportional valve used for flow control, located either upstream or downstream of the cavity, depending on the model. In March, 2015 we replaced the proportional valve (with Clippard EV-PM-10-4025) on the CFADS30 analyzer and this promptly resolved the cavity pressure problem (Figure 2-25).

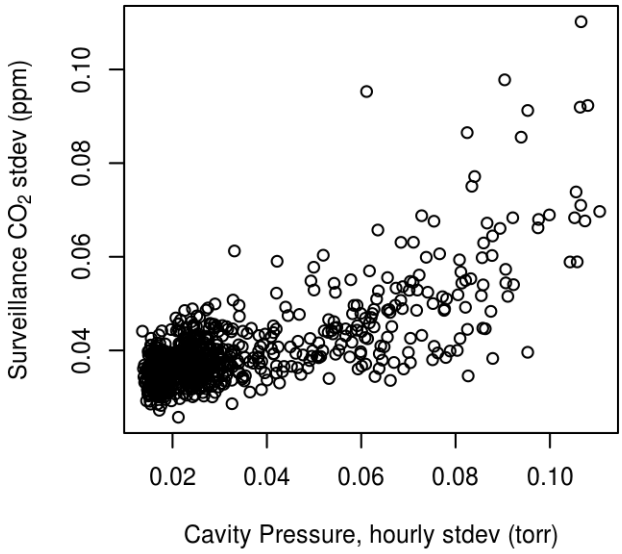

Figure 2-24. Standard deviation of CO_2 measurements during individual surveillance intervals versus cavity pressure standard deviations for corresponding hours. Data are from analyzer CFADS30 at located BU during July, 2014 through April, 2015.

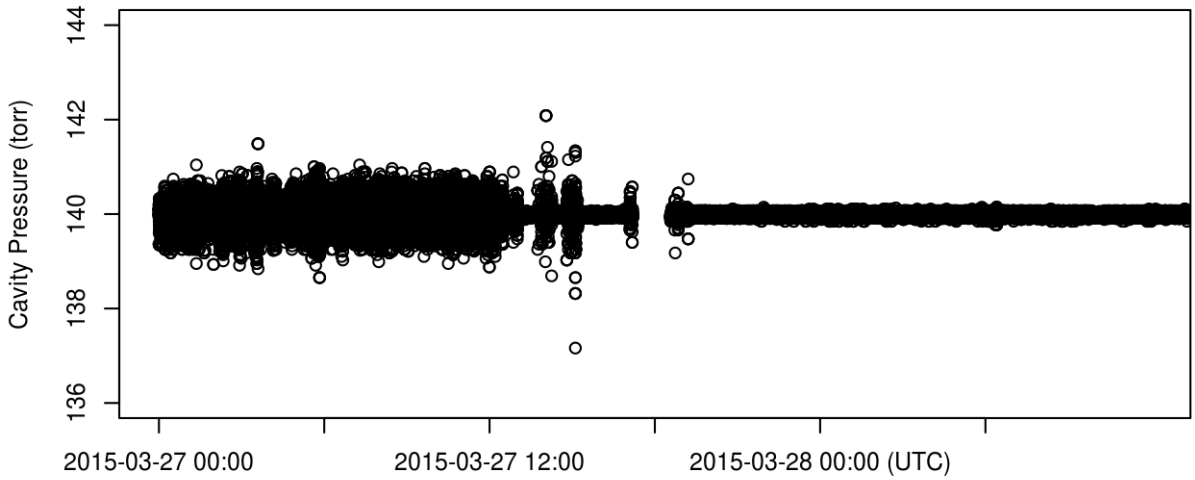

Figure 2-25. Cavity pressure over two days of operation of the CFADS30 analyzer in the lab. Cavity pressure variance was reduced on March 27 when the inlet proportional valve was replaced.

Surveillance equilibration time

After the CFFDS2051 analyzer at BU was replaced with the CFADS30 analyzer, we noticed that the equilibration time for the surveillance measurements of CO_2 was longer,

although no other components in the setup were modified. We came to understand that because the new analyzer had a higher flow rate than the old analyzer (~250 sccm vs. ~25 sccm), we had increased the pressure from the surveillance tank regulator in order to match the demands of the higher-flow instrument. When the valve opened to commence a surveillance measurement, there was a larger pressure change in the tubing connected to the surveillance tank, which induced increased surface interactions between CO_2 and the tubing walls, and led to the longer equilibration times (Figure 2-26).

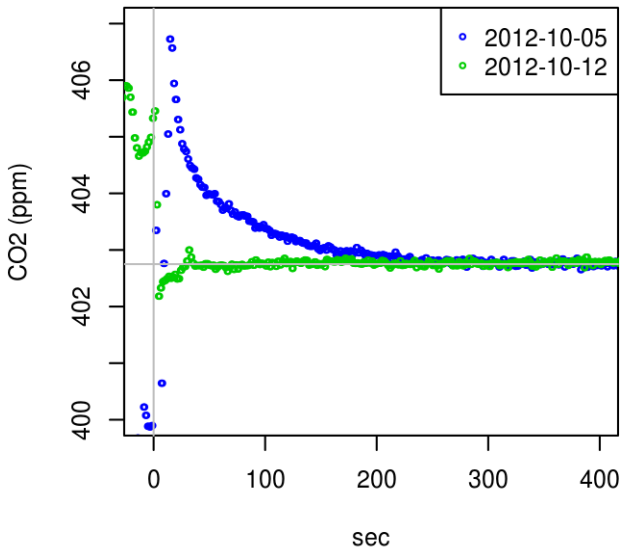

Figure 2-26. Surveillance measurements of CO_2 by analyzer CFADS30 at BU during two example intervals, before and after the flow restrictor was moved. The x-axis is formatted so that the time of valve actuation from both time periods occurs at 0 seconds.

To reduce this affect, the flow restrictor in the surveillance sample line was moved from near the regulator to near the valve (Figure 2-10), which had the impact of minimizing the surface area of sample line that experiences large pressure changes when the valve opened. This change in the position of the flow restrictor was made for all sites in the network and equilibration times improved throughout.

Ambient temperature effects

Because the cavity temperature is highly stable, it is assumed that measurements are not impacted by ambient temperature, as long as the analyzer is operating with the required ambient temperature range of ~10 – 35°C. However, we have found that ambient temperature variability can be related to increased measurement variability, even though the effect is not translated to the cavity temperature. This effect is demonstrated by data from the NHT site, where the analyzer was covered with a cardboard box in the winter to maintain the ambient temperature within the required range because the site had no heating. In this case, surveillance measurement residuals were smaller in the winter than the summer, and this appears to be related to the reduced ambient temperature variability (Figure 2-27) associated with the smaller volume of air in which the analyzer resided.

Despite the observed relationship between ambient temperature and measurement variability in the time-series (Figure 2-27), point-by-point correlations are weak, suggesting the effect is transient. Therefore, it is difficult to prescribe a set of ambient temperature conditions for improved performance. In general, we find that analyzer stability is improved when a passive mechanism to moderate ambient temperature is applied, such as by reducing the circulation volume around the analyzer or by shielding the analyzer from the direct impacts of forced air heating or cooling systems.

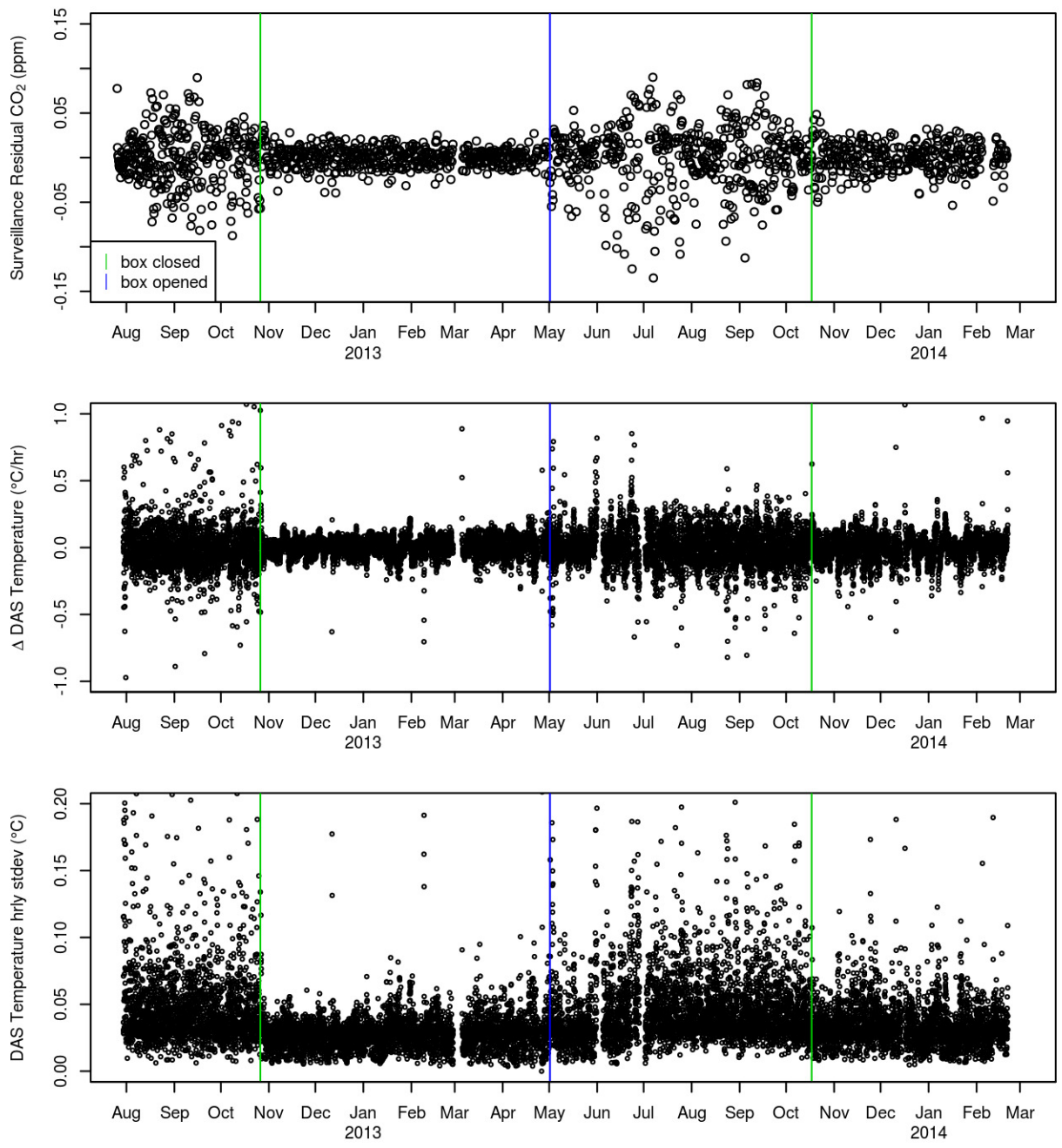

Figure 2-27. Timeseries of surveillance measurement residuals for CO_2 (as in Figure 2-16), hourly changes in Data Analytics System (DAS, i.e. computer enclosure) temperature, and hourly DAS temperature standard deviations, for the CFADS30 analyzer located at NHT. Times when the analyzer was covered and uncovered with a cardboard box are marked with vertical lines.

Summary of measurement results

A broad look at the atmospheric GHG measurement data collected at the Boston network sites since August, 2012 reveals many patterns in space and time, and differences between CO_2 and CH_4 (Figures 2-28 – 2-32). A strong seasonal pattern is apparent in the CO_2 record at all sites, but not in the CH_4 record, reflecting the summer drawdown of CO_2 by vegetation, most strongly at the HF site, but also at the urban sites. The largest and most variable CO_2 and CH_4 concentrations were observed at the BU site throughout the year and across all portions of the distributions. Larger synoptic-to-monthly scale temporal variability was observed for CH_4, with common features in data from all sites (Figure 2-30), suggesting variability derives from the regional-scale background, rather than from the nearby source region. Diel averages for CO_2 and CH_4 (Figures 2-31 and 2-32) show that peak concentrations occur in the morning at both urban sites and in all seasons, reflecting both decreased mixing in the nocturnal boundary layer and increased emissions in the morning in the case of CO_2. Peak concentrations at the taller COP site occur 1-2 hours later than at BU, reflecting the timing of the rise of the mixed layer in the morning.

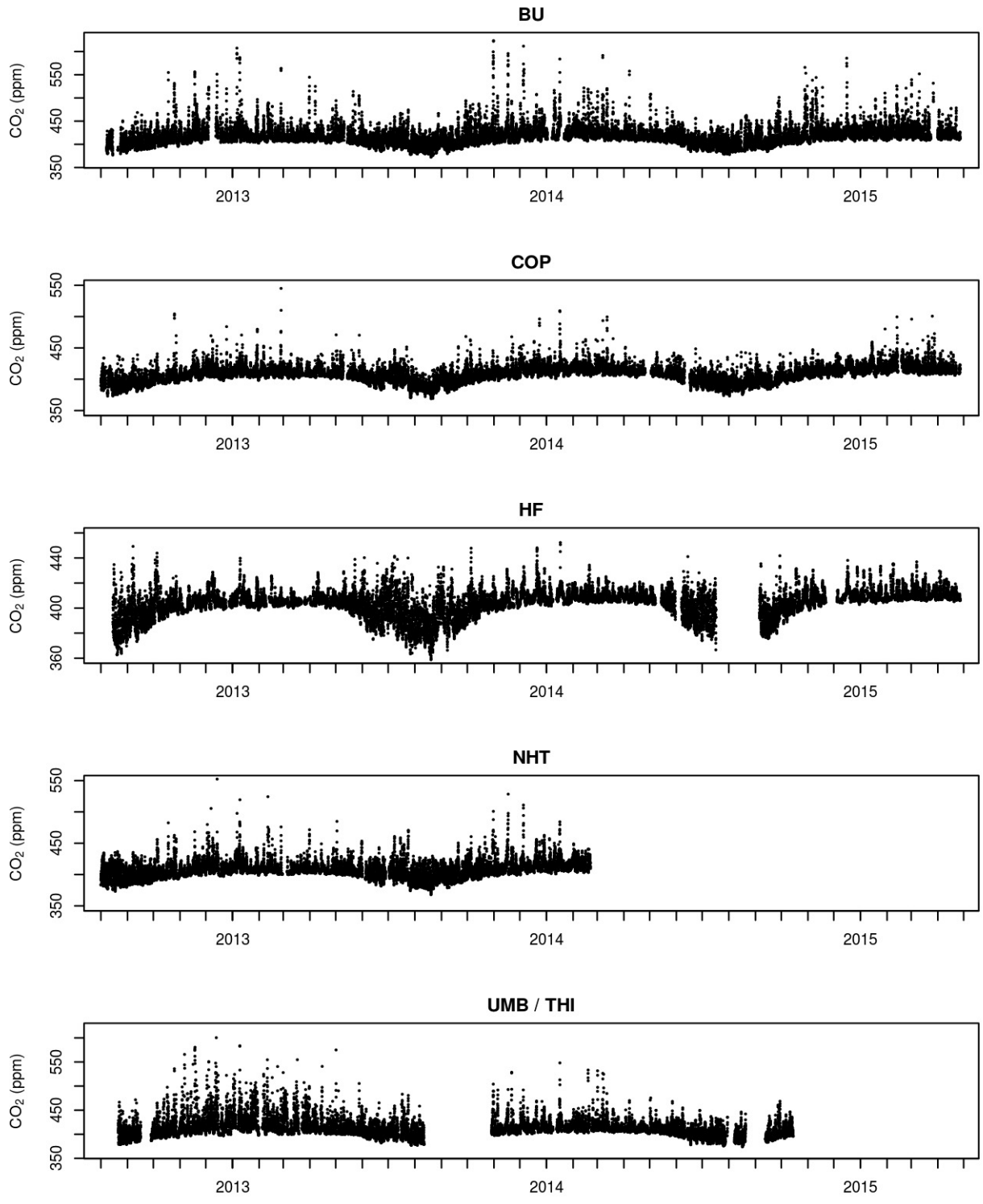

Figure 2-28. Hourly average CO_2 measurements from all sites in the Boston network over the full measurement period.

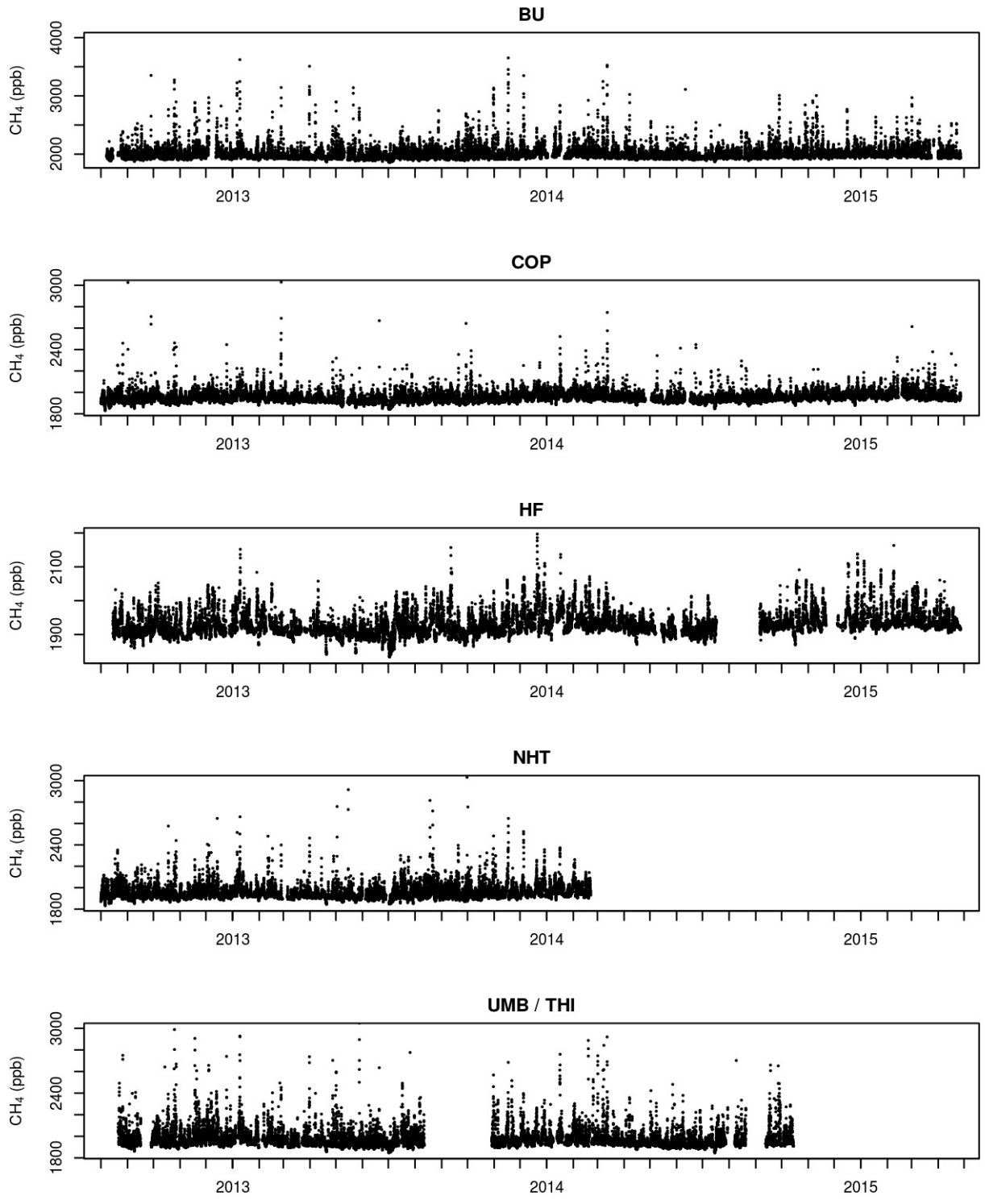

Figure 2-29. Hourly average CH_4 measurements from all sites in the Boston network over the full measurement period.

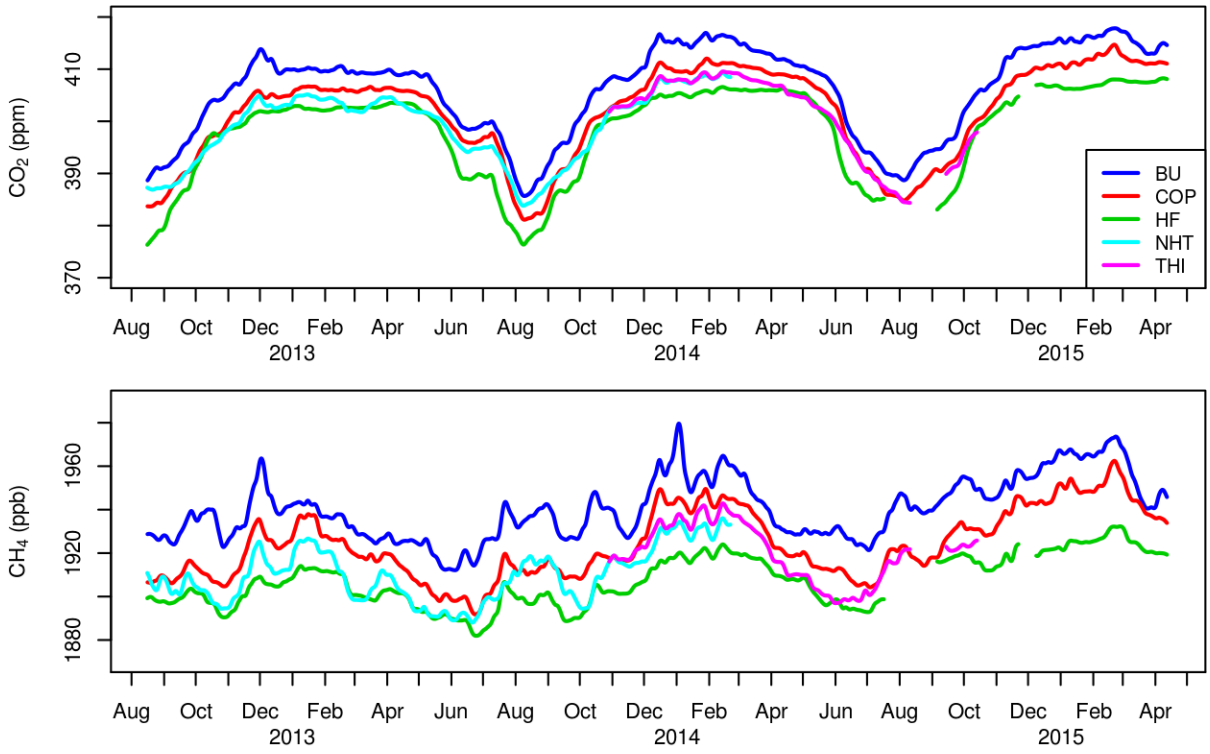

Figure 2-30. Smoothed, 30-day running, 20th-percentiles of CO_2 and CH_4 measurements from Boston network.

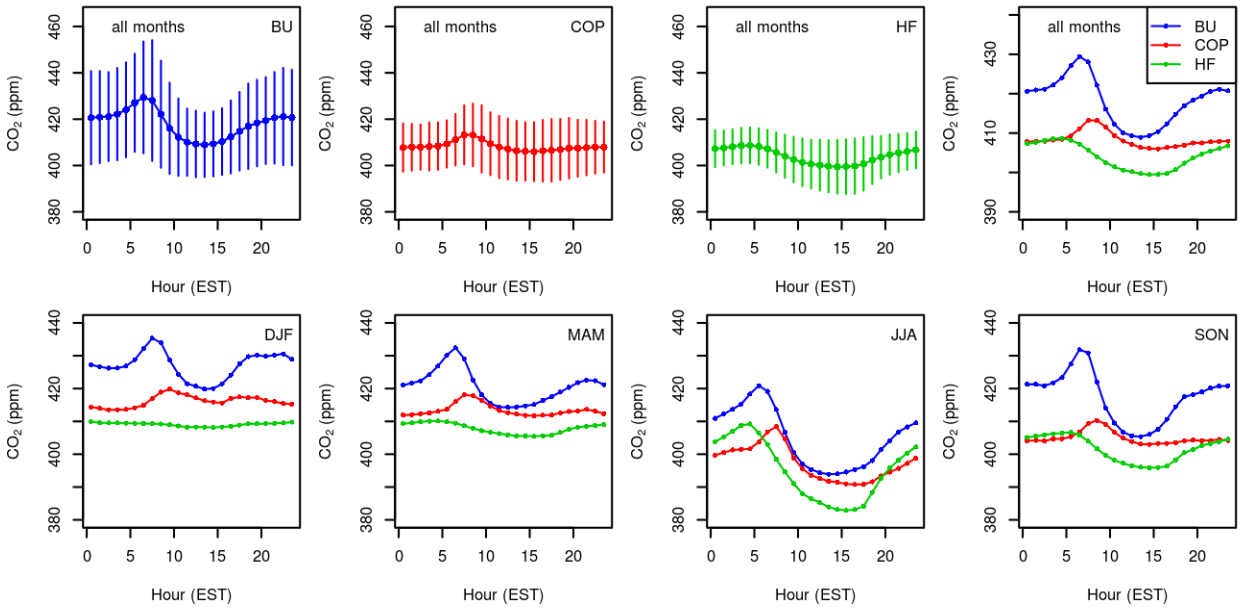

Figure 2-31. Average CO_2 by hour of the day from the BU, COP, and HF measurement sites from all months (top row) and by season (bottom row) for the full August, 2012 through April, 2015 measurement period. Error bars are ±1σ.

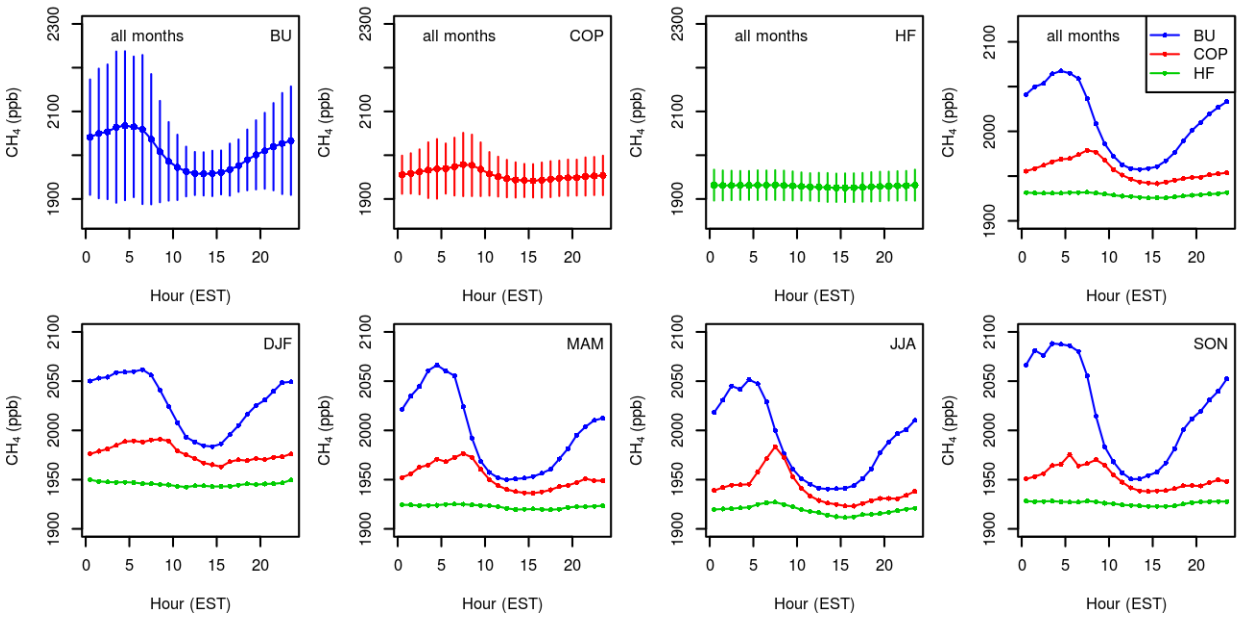

Figure 2-32. Average CH_4 by hour of the day from the BU, COP, and HF measurement sites from all months (top row) and by season (bottom row) for the full August, 2012 through April, 2015 measurement period. Error bars are ±1σ.

Acknowledgements

John Budney made significant contributions to the design and maintenance of the Boston measurement network. Bruce Daube offered helpful suggestions and advice on the network design, instrument operation, and troubleshooting problems throughout the duration of the project. Maryann Sargent ran the water-correction experiment and computed the results. Many members of the Wofsy group, including Jasna Pittman, Rachel Chang, Elaine Gottlieb, Roisin Commane, Jakob Lindaas, and Conner Daube, helped with calibrations and field work. Bill Munger provided access to and ongoing information about the HF site. Access and accommodations were provided by George McNaughton and Deborah Warren at the NHT site, Brian Swett, Dan Shanahan, and Joe Bertoni at the COP site, Lucy Hutyra at the BU site, Crystal Schaff and Francesco Peri at the UMB site, and by Nate Puritz and Arthur Pearson at the THI site. Nathan Phillips, Lucy Hutyra, and Crystal Schaff contributed analyzers to the project.

References

Chen H, Winderlich J, Gerbig C, Hoefer A, Rella CW, Crosson ER, Van Pelt AD, Steinback J, Kolle O, Beck V, Daube BC, Gottlieb EW, Chow VY, Santoni GW, Wofsy SC (2010) High-accuracy continuous airborne measurements of greenhouse gases (CO2 and CH4) using the cavity ring-down spectroscopy (CRDS) technique, Atmospheric Measurement Techniques, 3: 375-386.

Crosson ER (2008) A cavity ring-down analyzer for measuring atmospheric levels of methane, carbon dioxide, and water vapor, Applied Physics B, 92: 403-408.

Daube BC, Boering KA, Andrews AE, Wofsy SC (2002) A high-precision fast-response airborne CO_2 analyzer for in situ sampling from the surface to the middle stratosphere, Journal of Atmospheric and Oceanic Technology, 19: 1532-1543.

Meredith LK, Commane R, Munger JW, Dunn A, Tang J, Wofsy SC, Prinn RG (2014) Ecosystem fluxes of hydrogen: a comparison of flux-gradient methods, Atmospheric Measurement Techniques, 7: 2787-2805.

Nara H, Tanimoto H, Tohjima Y, Mukai H, Nojiri Y, Katsumata K, Rella CW (2012) Effect of air composition (N_2, O_2, Ar, and H_2O) on CO_2 and CH_4 measurement by wavelength-scanned cavity ring-down spectroscopy: calibration and measurement strategy, Atmospheric Measurement Techniques, 5: 2689-2701.

Prasad K, Bova A, Whetstone JR, Novakovskaia E (2013) Greenhouse gas emissions and dispersion 1. Optimum placement of gas inlets on a building rooftop for the measurement of greenhouse gas concentration, NIST Special Publication 1158, http://nvlpubs.nist.gov/nistpubs/SpecialPublications/NIST.SP.1158.pdf.

Rella CW (2012) Accurate stable carbon isotope ratio measurements in humid gas streams using the Picarro $\delta^{13}CO_2$ G2101-i gas analyzer, White Paper of Picarro Inc (Sunnyvale, CA) www.picarro.com/assets/docs/White_Paper_G2101-i_Water_Correction_.pdf.

Rella CW, Chen H, Andrews AE, Filges A, Gerbig C, Hatakka J, Karion A, Miles NL, Richardson SJ, Steinbacher M, Sweeney C, Wastine B, Zellweger C (2013) High-accuracy measurements of dry mole fractions of carbon dioxide and methane in humid air, Atmospheric Measurement Techniques, 6: 837-860

Richardson SJ, Miles NL, Davis KJ, Crosson ER, Rella CW, Andrews AE (2012) Field testing of cavity ring-down spectroscopy analyzers measuring carbon dioxide and water vapor, Journal of Atmospheric and Oceanic Technology, 29: 397-406.

Ross C (2015 Jan 14) Developer breaking ground on Boston's tallest new skyscraper, Boston Globe, Construction is expected to be completed in 2017, www.bostonglobe.com/business/2015/01/14/developer-breaking-ground-boston-tallest-new-skyscraper-years/WZxaUtPZFdAovNazZAsPaM/story.html.

Urbanski S, Barford C, Wofsy S, Kucharik C, Pyle E, Budney J, McKain K, Fitzjarrald D, Czikowsky M, Munger JW (2007) Factors controlling CO_2 exchange on timescales from hourly to decadal at Harvard Forest, Journal of Geophysical Research, 112: G02020.

World Meteorological Organization (2014) 17th WMO/IAEA Meeting of Experts on Carbon Dioxide, Other Greenhouse Gases and Related Tracers Measurement Techniques (Beijing, China, 10-13 June 2013). GAW Report No. 213.

Chapter 3

Methane emissions from natural gas infrastructure and use in the urban region of Boston, Massachusetts

Abstract

Methane emissions from natural gas delivery and end use must be quantified to evaluate the environmental impacts of natural gas and to develop and assess the efficacy of emission reduction strategies. We report natural gas emission rates for one year in the urban region of Boston, using a comprehensive atmospheric measurement and modeling framework. Continuous methane observations from four stations are combined with a high-resolution transport model to quantify the regional average emission flux, 18.5 ± 3.7 (95% confidence interval) g $CH_4 \cdot m^{-2} \cdot y^{-1}$. Simultaneous observations of atmospheric ethane, compared with the ethane-to-methane ratio in the pipeline gas delivered to the region, demonstrate that natural gas accounted for ~60–100% of methane emissions, depending on season. Using government statistics and geospatial data on natural gas use, we find the average fractional loss rate to the atmosphere from all downstream components of the natural gas system, including transmission, distribution, and end use, was 2.7 ± 0.6% in the Boston urban region, with little seasonal variability. This fraction is notably higher than the 1.1% implied by the most closely comparable emission inventory.

Introduction

Atmospheric methane (CH_4) is an important greenhouse gas (Myhre et al. 2013) and major contributor to elevated surface ozone concentrations worldwide (Fiore et al. 2002). Current atmospheric CH_4 concentrations are 2.5 times greater than preindustrial levels due to anthropogenic emissions from both biological and fossil fuel sources. The growth rate of CH_4 in the atmosphere slowed beginning in the mid-1980s and plateaued in the mid-2000s, but growth has resumed since 2007. The factors responsible for the observed global increase and interannual trends, and the spatiotemporal distribution of sources, remain uncertain (Ciais et al. 2013).

Losses of natural gas (NG) to the atmosphere are a significant component of anthropogenic CH_4 emissions (Ciais et al. 2013), with important implications for resource use efficiency, worker and public safety, air pollution, and human health (West et al. 2006), and for the climate impact of NG as a large and growing source of energy. A major focus area of the US Climate Action Plan is reduction of CH_4 emissions (The White House 2014), but implementation requires identification of dominant source types, locations, and magnitudes. A recent review and synthesis of CH_4 emission measurements in North America, spanning scales of individual components to the continent, found that inventory methods consistently underestimate CH_4 emissions, that fossil fuels are likely responsible for a large portion of the underestimate, and that significant fugitive emissions may be occurring from all segments of the NG system (Brandt et al. 2014).

The present study quantifies CH_4 fluxes from NG in the urbanized region centered on Boston. Elevated CH_4 concentrations in urban environments have been documented around the world for decades (Blake et al. 1984) (Table 3-1) and attributed to a variety of anthropogenic source types. Recent studies of urbanized regions in California, using diverse atmospheric

observing and modeling approaches, consistently found that CH_4 emission rates were larger than those estimated by regional bottom-up inventories (Wunch et al. 2009, Hsu et al. 2010, Wennberg et al. 2012, Peischl et al. 2013, Santoni et al. 2013). In Boston, elevated CH_4 concentrations have been observed at street level and attributed to >3,000 NG pipeline leaks from antiquated infrastructure (Phillips et al. 2013), but associated CH_4 emission rates were not quantitatively assessed.

Table 3-1. Methane emissions in urban areas from atmosphere-based ("top-down") studies. Only studies that reported emission rates averaged in time and space are listed.

Study	**Location**	**Measurement year**	**Emission rate (g CH_4 m^{-2} yr^{-1})**
Moriizumi et al. 1996	Nagoya, Japan	1990-91	7
Lamb et al. 1995	Midwest town, USA	1991	55
Shorter et al. 1996	Two towns in East Germany	1992	12, 60
Fowler et al. 1996	North Britain	1994	28 – 56
Levin et al. 1999	Heidelberg, Germany	1995-97	8 ± 2
Kuc et al. 2003	Krakow, Poland	1996-97	20
Zinchenko et al. 2002	St. Petersburg, Russia	1996-2000	32 ±9
Su et al. 2003	Beijing, China	2000	50
Hsu et al. 2010	Los Angeles County, CA, USA	2007-08	205 ± 6*
Wunch et al. 2009	South Coast Air Basin, CA, USA	2007-08	228 ± 38*
Mays et al. 2009	Indianapolis, IN, USA	2008	71 ± 50
Wennberg et al. 2012	South Coast Air Basin, CA, USA	2010	167 ± 57*
Peischl et al. 2003	South Coast Air Basin, CA, USA	2010	156 ± 14*
Santoni 2013	South Coast Air Basin, CA, USA	2010	127 ± 21*
Wecht et al. 2014†	South Coast Air Basin, CA, USA	2010	160 ± 30*
Wecht et al. 2014‡	South Coast Air Basin, CA, USA	2010	118 ± 30*
Gioli et al. 2012	Florence, Italy	2011	58
O'Shea et al. 2014	London, UK	2012	66 ± 10

*Basin-total fluxes reported in the California studies were converted to average area fluxes using areas from the California Air Resources Board Almanac, Appendix D (2005).
†Aircraft observations
‡Satellite observations

In this study, we combine four key quantities in an atmosphere-based analytical framework: (i) atmospheric CH_4 enhancements above background (ΔCH_4) were determined from

measurements at a network of continuous monitoring stations, inside and upwind of the urban core, for 12 months in 2012–2013; (ii) total CH_4 emissions were derived from an atmospheric transport model, which quantitatively links surface fluxes with observed ΔCH_4 using assimilated meteorology; (iii) the contribution of NG to CH_4 emissions was quantified for cool and warm seasons by measuring atmospheric ethane (C_2H_6), a tracer of thermogenic CH_4, and comparing ratios of C_2H_6 and CH_4 in the atmosphere and in the pipeline gas flowing through the region; and (iv) the fraction of delivered NG lost to the atmosphere was estimated by comparing CH_4 emissions to spatially explicit data on NG consumption. The result encompasses NG losses from the entire urbanized region, including emissions from NG transmission, storage, distribution, end use, and liquefied NG importation.

Methane concentrations in the Boston atmosphere

Atmospheric CH_4 concentrations were measured continuously from September 2012 through August 2013 at two locations near the urban center [Boston University (BU) and Copley Square (COP)] and two locations outside of Boston [Harvard Forest (HF) and Nahant (NHT)] (Figure 3-1, Table 3-2). Distributions of possible background concentrations in air flowing into the city were estimated by randomly sampling each day from a range (5th to 35^{th}) of lower percentiles of CH_4 measurements from two upwind stations (HF or NHT, depending on the direction of simulated air trajectories), averaged over a 48-hour moving window (Figure 3-2). The lower percentile and moving window approach was employed to capture synoptic-scale variability and because near-surface nighttime observations are often affected by small nearby sources due to stratification of the nocturnal boundary layer which traps emissions near the ground. Values of ΔCH_4 were calculated by subtracting background from urban concentrations.

Hourly average ΔCH_4 data were aggregated into daily afternoon (11–16 h EST, 16–21 h UTC) (Figure 3-3) means to remove autocovariance and focus the analysis on periods of well-mixed atmospheric conditions.

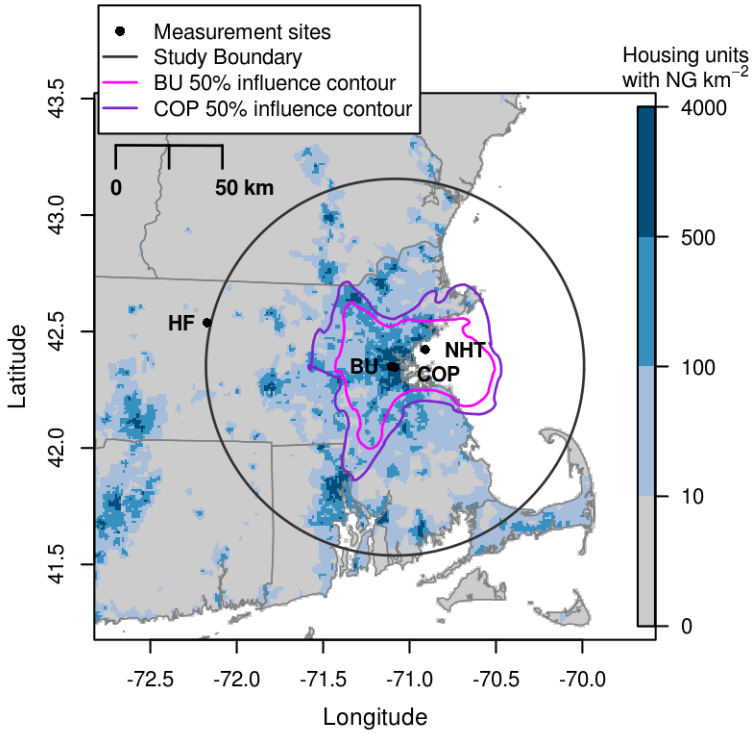

Figure 3-1. Location of two city [Boston University (BU), 29-m height; Copley Square (COP), 215-m height] and two peripheral [Harvard Forest (HF); Nahant (NHT)] measurement stations (black points) in Boston, and the surrounding area, overlaid on a map of the number of housing units with NG per square kilometer (US Census Bureau 2012a). The 90-km radius circle delineates the ~18,000 km^2 land area for which CH_4 emissions and the NG loss rate were calculated. The magenta and purple contours enclose 50% of the average footprint (sensitivity area) of the BU and COP afternoon measurements, respectively. The two city sites are difficult to distinguish at this scale because the horizontal distance between them is ~2 km. The influence area is ~80% larger for COP than BU because the former station is higher.

Table 3-2. Locations of the four measurement sites.

Site	**Longitude, °**	**Latitude, °**	**Height, m above ground**
Boston University (BU)	-71.10	42.35	29
Copley Square (COP)	-71.08	42.35	215
Harvard Forest (HF)	-72.17	42.54	29
Nahant (NHT)	-70.91	42.42	16

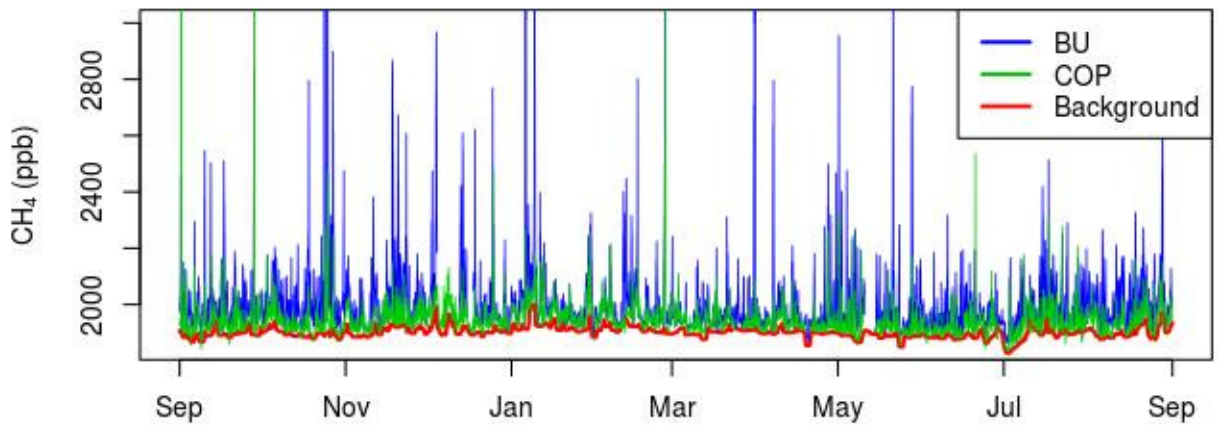

Figure 3-2. Mean hourly CH_4 concentrations in the empirical background and measured at BU and COP from September 1, 2012 through August 31, 2013.

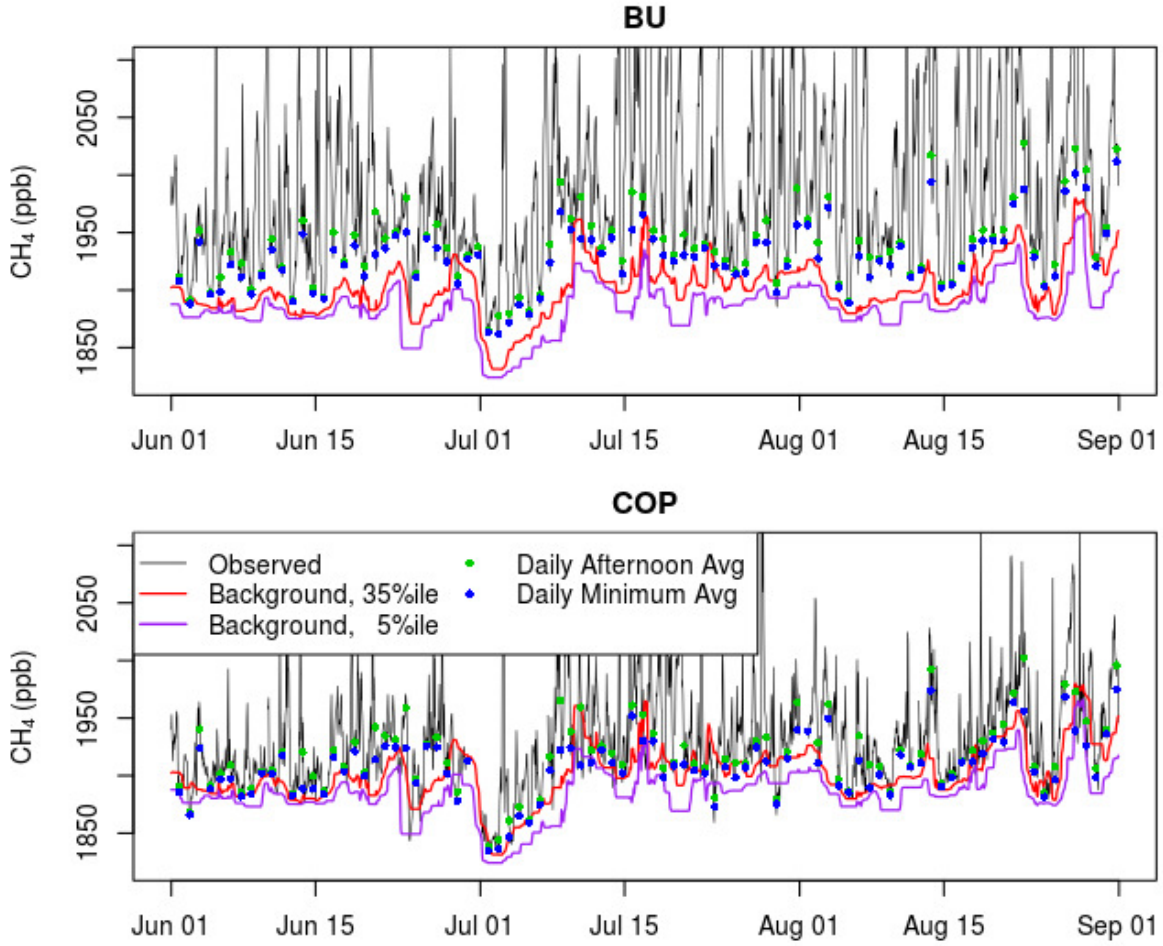

Figure 3-3. Mean hourly measured CH_4 concentrations (black lines), the range of empirical background concentrations from upwind stations (red and purple lines), and the daily afternoon average (green) and minimum (blue) points that represent mean enhancements at BU and COP, from an example period of three months in 2013.

Methane concentrations in Boston were consistently elevated over background (Figures 3-2 – 3-4) and followed a distinct daily pattern (Figure 3-15), associated with growth and decay of the planetary boundary layer. Concentrations fluctuated over short timescales (Figure 3-2) due to small-scale atmospheric circulations and heterogeneous sources in the urban environment. Methane concentrations were higher in winter than the other seasons at both sites, but ΔCH_4 varied less with season (Figure 3-4). The average annual afternoon values of ΔCH_4 at BU and COP were 45.9 (37.3, 58.5) ppb and 30.5 (23.6, 39.3) ppb, respectively (Figure 3-4), reflecting different sampling altitudes (30 and 215 m, respectively; Table 3-2). All errors reported throughout the paper are 95% confidence intervals. Uncertainties in ΔCH_4 (Figure 3-4) were calculated through a bootstrap analysis that included background concentrations and afternoon hourly, daily, and seasonally averaged CH_4 measurements.

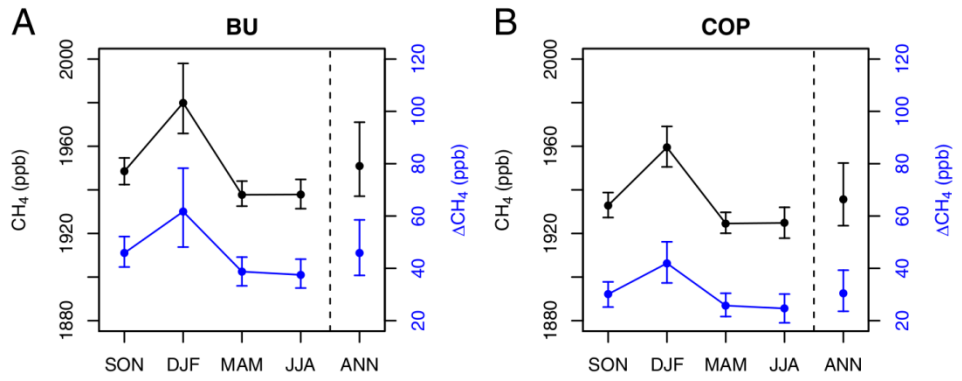

Figure 3-4. Average (±95% confidence intervals) afternoon (11–16 h EST) CH_4 (black; left y-axis) and ΔCH_4 (blue; right y-axis) by season and for the whole year at (A) BU and (B) COP.

Modeling framework

Atmospheric transport model

Methane enhancements were modeled at BU and COP with the Stochastic Time-Inverted Lagrangian Transport model (STILT, v656, Lin et al. 2003), driven with customized meteorological

fields from the advanced research version of the Weather Research and Forecasting meso-scale meteorological model (WRF, v3.4.1, Skamarock and Klemp 2008) run at 1-km^2 grid resolution (WRF-STILT) (Nehrkorn et al. 2010). Meteorological fields were generated at four gridded horizontal resolutions (1, 3, 9, and 27 km) in a two-way nested arrangement centered on Boston (Figure 3-5). All WRF domains had 42 vertical levels. Initial and lateral boundary conditions were provided by the North American Regional Reanalysis (Mesinger et al. 2006). Overlapping 30-hour forecasts were initialized every 24 hours, at 00 UTC, and the first 6 hours of each forecast were discarded to allow for spinup. Grid nudging was used in the outer-most domain only and not within the planetary boundary layer (PBL). Additional details of the WRF configuration used in this study are given in Nehrkorn et al. (2013, case "Turb-U").

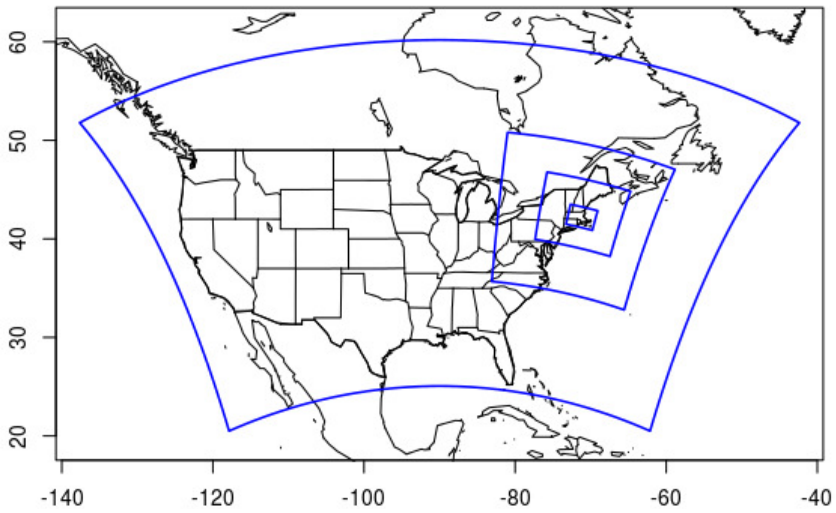

Figure 3-5. Location of the four nested WRF domains. The horizontal resolutions of the largest to smallest domains are 27, 9, 3, and 1 km.

WRF-simulated meteorological fields were compared against available meteorological measurements at National Weather Service observing sites (NCEP 2004) using the Model Evaluation Tools verification software from the National Center for Atmospheric Research

(2013). Figure 3-6 shows summary statistics of average near-surface temperature and wind speed biases and errors for the simulated year at each surface station used in the verification. For most land-based stations, WRF wind speeds were biased slightly high and temperatures were biased slightly low. Examination of the average diurnal cycle (Figure 3-7) reveals that the wind speed bias is present at all hours of the day, whereas the temperature bias is due largely to stronger than observed nocturnal cooling.

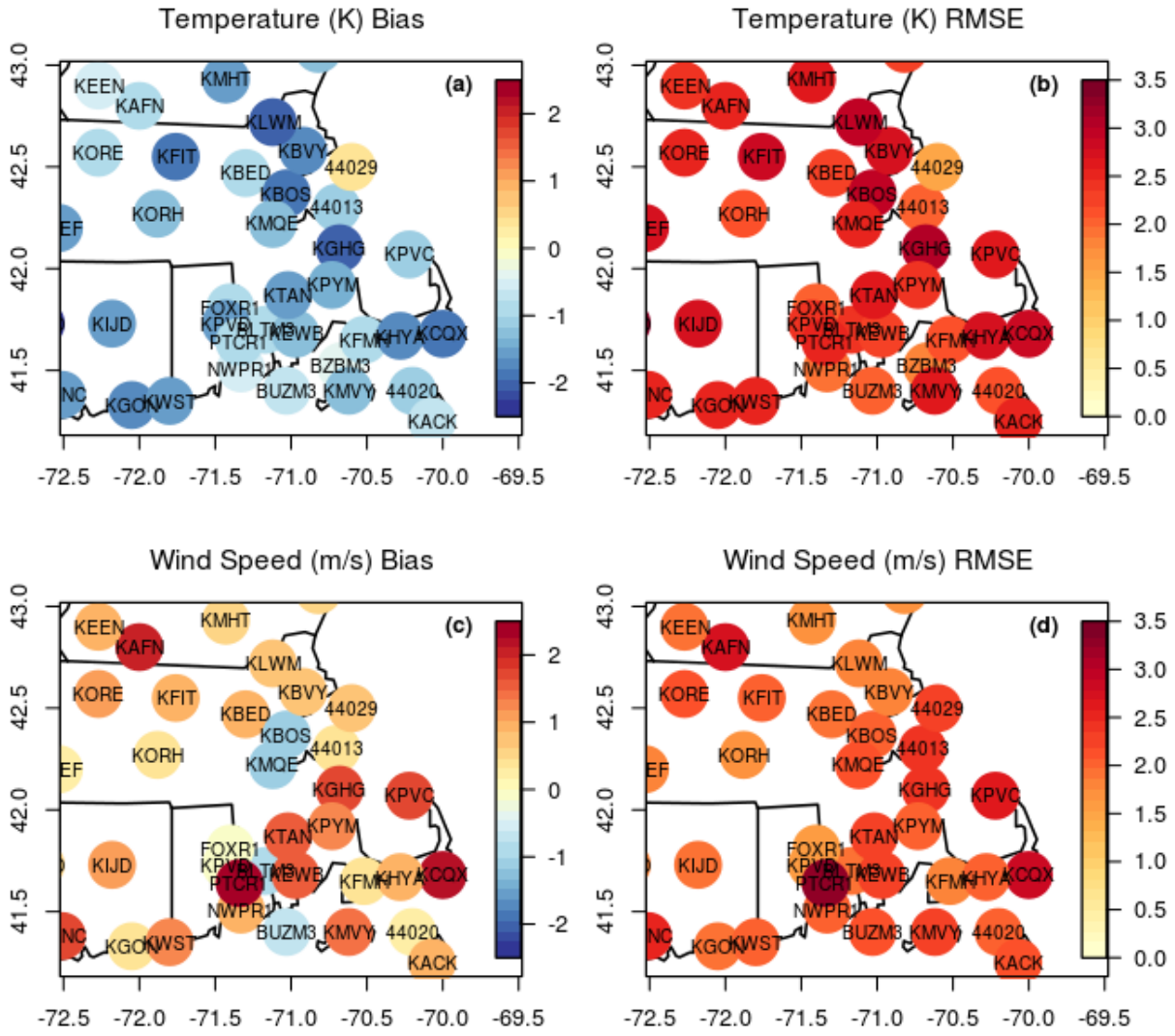

Figure 3-6. Average (A,C) bias and (B,D) root mean square error (RMSE) of WRF-simulated (A,B) near-surface temperature and (C,D) wind speed for National Weather Service stations (NCEP 2004) in the innermost WRF domain.

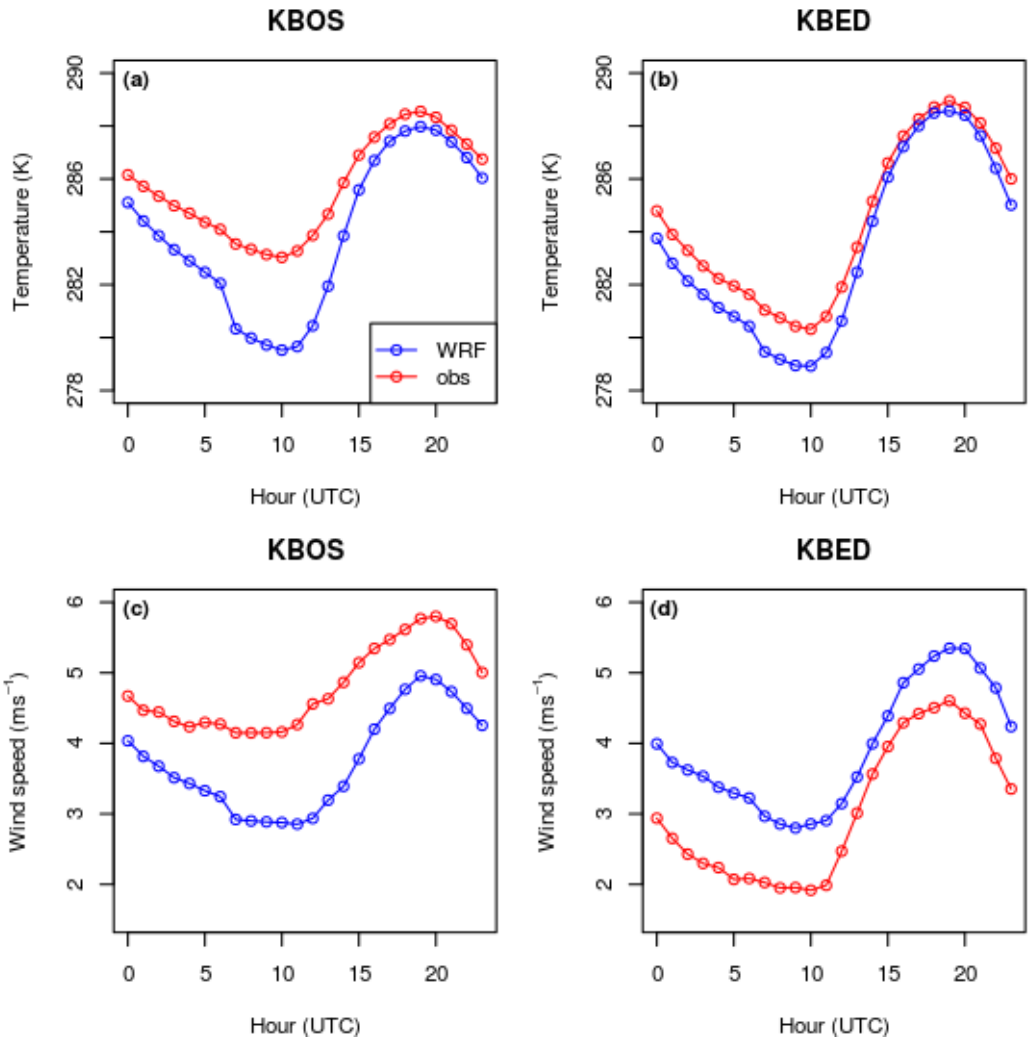

Figure 3-7. Observed (red) and WRF-simulated (blue) near-surface (A,B) temperature (C,D) and wind speed, averaged by hour (UTC) for one year and stations (A,C) KBOS (at Boston Logan airport) and (B,D) KBED (northwest of Boston). See Figure 3-6 for station locations.

STILT was run in time-reverse mode in which an ensemble of 500 particles was released every hour from each of the urban measurement sites and transported backward in time for 10 days according to the WRF meteorology. The majority of particles reached the study boundary (Figure 3-1) in < 8 hours and the median travel time was < 3 hours. Background values generated from NHT measurements were assigned to particles that exited the coastal portion (at 20-140°) of circular boundary (~22% of particles) and background values from HF were

assigned to all other particles. WRF-STILT generates footprints (with units ΔCH_4 per unit surface flux [ppm/(μmole m^{-2} s^{-1})]), which represent the sensitivity of each measurement point in space and time to upwind surface fluxes. Both urban measurement sites were sensitive to emissions from the greater Boston region, with COP sensitive to a larger area than BU due to its higher altitude (Figure 3-1 and Table 3-2).

Prior flux fields

WRF-STILT footprints were combined with spatially-resolved prior models of CH_4 emissions to generate a set of simulated ΔCH_4 values for each hour at each measurement station. Two CH_4 emission priors, EDGAR v4.2 FT2010 (European Commission 2013) and one created for this study (Table 3-3), were tested as inputs to the modeling framework. EDGAR is a global product that uses simplified methods (e.g. scaling by population density) to spatially disaggregate emissions. To take advantage of locally available data and knowledge, a customized emission prior with five anthropogenic and biogenic source categories (described in detail below) and 1 km^2 spatial resolution was developed for the study domain (Figure 3-8). The custom prior was not meant to be exhaustive, but rather was created to provide detailed emission estimates for key sectors with improved spatial resolution and accuracy. Both priors were adopted as temporally invariant. Emission results using the customized prior are presented as the main results and results using EDGAR are presented in a sensitivity analysis of modeling-framework variants.

Table 3-3. Average CH_4 emission in Massachusetts and in the 90-km radius study area (Figure 3-1) by sector and in total from three emissions inventories – the custom inventory, EDGAR (European Commission 2013), and the state GHG inventory (MA DEP 2014). The MA inventory was not tested in the modeling framework because it is not spatially resolved.

			Average Emissions ($g\ CH_4\ m^{-2}\ yr^{-1}$) (% of total)	
Inventory	**Sector**		**Massachusetts**	**Study Area**
Custom*	Wetlands		0.93 (16%)	1.02 (14%)
	Enteric Fermentation		0.25 (4%)	0.22 (3%)
	Transportation		0.05 (1%)	0.06 (1%)
	Large Point Sources (Power plants, Industrial, Landfills, Wastewater)		1.13 (19%)	1.43 (20%)
	Natural Gas		3.56 (60%)	4.49 (62%)
	Total		5.92	7.22
EDGAR (2010)	Energy production (1A1_1A2)		0.17 (2%)	0.23 (2%)
	Non-road Transportation (1A3a_c_d_e)		0	
	Road Transportation (1A3b)		0.05 (1%)	0.06 (1%)
	Stationary Combustion (1A4)		0.28 (4%)	0.38 (4%)
	Fugitive from Solid Fuels (1B1)		0	
	Oil Production & Refining (1B2a)		0.12 (2%)	0.15 (2%)
	Natural Gas Production & Distribution (1B2b)		3.50 (46%)	4.76 (59%)
	Industrial (2)		0.03	0.04
	Enteric Fermentation (4A)		0.15 (2%)	0.14 (1%)
	Manure Management (4B)		0.05 (1%)	0.05
	Agricultural Soils (4C_4D)		0	0
	Agricultural Waste Burning (4F)		0	0
	Solid Waste Disposal (6A_6C)		2.13 (28%)	2.44 (35%)
	Waste Water (6B)		1.04 (13%)	1.44 (15%)
	Fossil Fuel Fires (7A)		0	0
	Total		7.52	9.69
Massachusetts State (2011)	Stationary Combustion	Residential	0.19 (2%)	
		Commercial	0.05 (1%)	
		Industrial	0.01	
		Electric Power	0.01	
	Mobile		0.30 (3%)	
	Natural Gas Transmission & Distribution		3.73 (42%)	
	Enteric Fermentation		0.18 (2%)	
	Manure Management		0.05 (1%)	
	Landfills & Waste Combustion		3.49 (39%)	
	Wastewater		0.95 (11%)	
	Total		8.96	

*The custom prior emissions model covers the majority, but not the entire state of Massachusetts (Figure 3-8), so the average emissions rate for Massachusetts was calculated from the area of the state that is covered by the inventory.

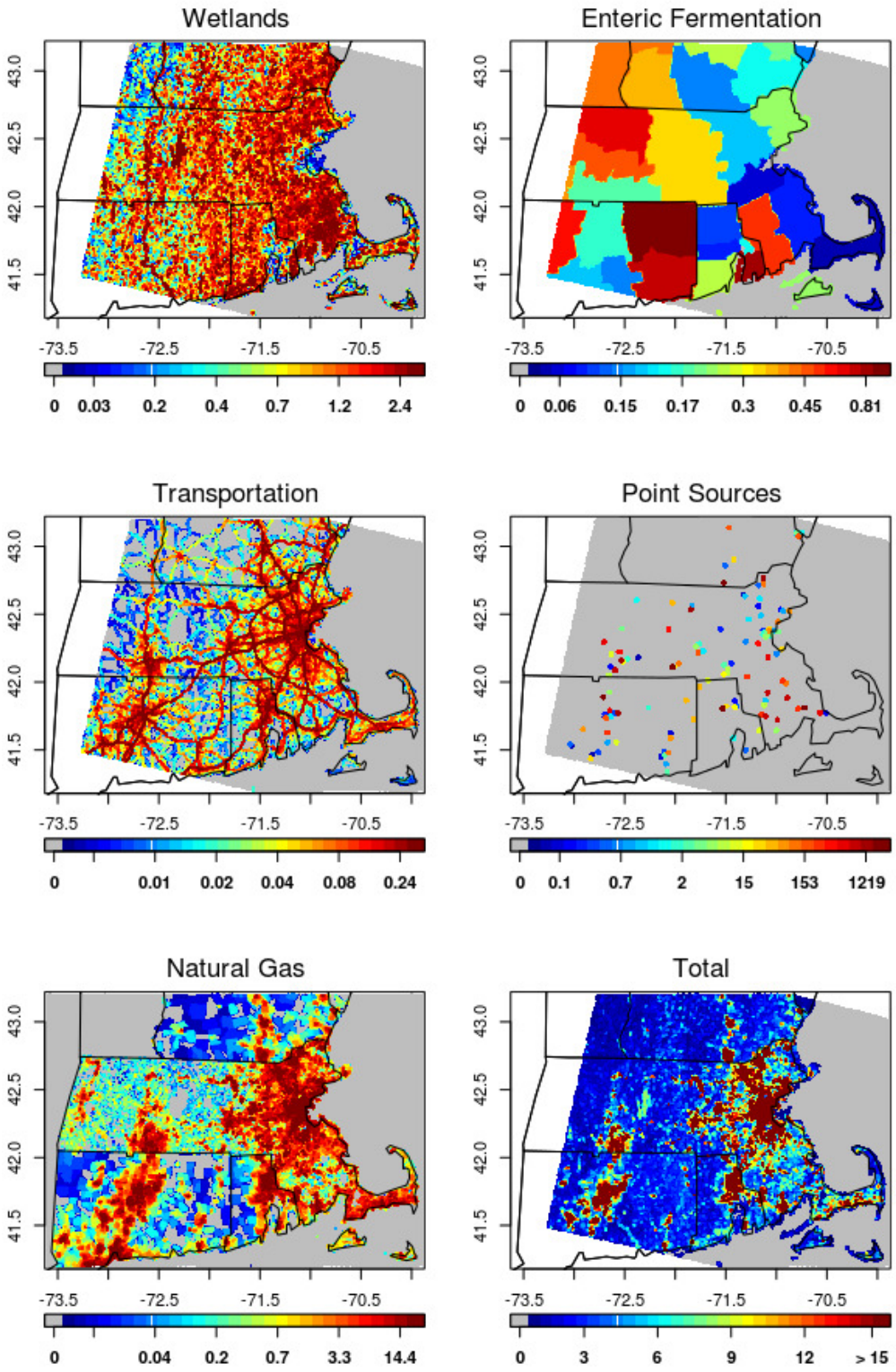

Figure 3-8. Maps of prior Emissions (g CH_4 m^{-2} yr^{-1}) by source type and in total on a 1 km^2 grid from the inventory constructed for this study. Scale bars for individual sectors are not linear and were set to have an equal sample size in each bin in order to better render spatial patterns. The scale bar for total emissions is linear.

Wetlands. Data on wetlands' location, size, and type were obtained from the National Wetlands Inventory (US Fish and Wildlife Service 2013) for the four states in the study region. These wetland inventories are based on aerial photography and have a mapping unit of 0.4 – 1.2 hectares. Average CH_4 emission rates for each type were taken from Bridgham et al. (2007), which calculated mean emission rates from > 100 studies. An average emission rate of 7.6 g CH_4 m^{-2} yr^{-1} was applied to the freshwater wetlands (emergent and forested/shrub) and an emission rate of 1.3 g CH_4 m^{-2} yr^{-1} was applied to saltwater wetlands (estuarine and marine). Areas of open water (rivers, lakes, deepwater marine) were not included in the wetlands emission layer due to a lack of emissions data from these areas. The total wetland area in the study domain of the prior was 1,900 km^2, ~11% of the land area.

Enteric fermentation. Methane emissions from ruminant livestock were spatially allocated to counties according to county-level headcounts of cattle and calves from the USDA 2007 Agricultural Census (2009). An emission factor of 117 kg CH_4 $head^{-1}$ yr^{-1}, the Environmental Protection Agency (EPA, 1998) emission factor for mature dairy cattle in the North Atlantic Region, was multiplied by the cattle count in each county to yield a total average emission rate. Emissions from animals other than cattle were not included because cattle accounted for the majority of livestock emissions in the study area.

Transportation. Methane emissions from transportation were estimated using per-mile emission factors by vehicle type and model year (US EPA 2008, 2014c), state-level data on vehicle fleet composition (Federal Highway Administration 2012), and a database of vehicle miles traveled per road (Gately et al. 2013). A complete methodological description for an analogous emissions model for CO_2 is provided in Gately et al. 2013.

Point-sources. Annual facility-level data reported to the EPA GHG Reporting Program (2014a) were used to represent CH_4 emissions from the largest point sources, including landfills, waste combustion, and waste water treatment plants. Data from 2012 and 2013 were weighted according to the study time period (25% in 2012 and 75% in 2013). Emissions from NG distribution companies were not included because they were not considered point sources and were conceptually accounted for in the NG losses layer (described next).

Natural gas losses. Methane emissions from NG losses were spatially allocated according to the areas of residential and commercial NG consumption (as described in the next section) and scaled so total emissions from NG in Massachusetts was equal to the state inventory estimate for 2012 (Massachusetts DEP 2014, Table 3-3). The prior flux fields were not used to determine the fractional contribution of the NG, nor any other, source sector, to total CH_4 emissions because atmospheric C_2H_6 measurements provided definitive attribution of CH_4 emissions from NG.

Natural gas consumption

In order to understand emissions results as a fractional loss rate of NG delivered within the modeling framework, it was necessary to create a spatially explicit map of NG consumption (Figure 3-9). Consumption is an appropriate estimator of net gas flows through the study area because all of the pipelines entering the study area terminate inside or very near the study area boundary (Figure 3-10). Reports of NG consumption by state, month, and sector were obtained from the Energy Information Administration (US EIA, 2014b) for the study area and time period. Volumes of NG were converted to masses of CH_4 using the ideal gas law by assuming industry standard temperature and pressure (60 ℉ and 1 atm) and 97% CH_4 content, based on gas quality data reported by transmission pipeline companies serving the region (Algonquin Gas

Transmission 2014, Tennessee Gas Pipeline Company 2014, Figure 3-10), giving 1 scf NG = 1.16 moles CH_4 = 18.6 grams CH_4.

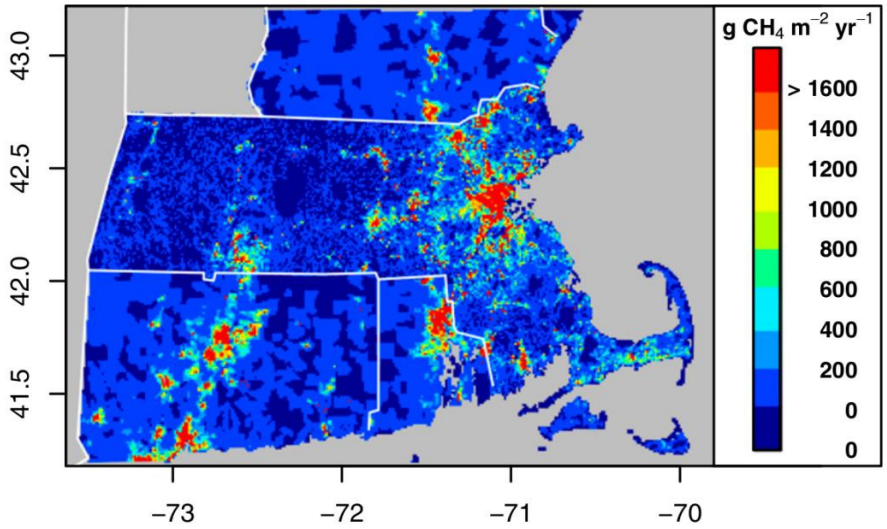

Figure 3-9. Reconstructed geographical distribution of NG consumption, in units of CH_4 mass flux, during September 2012 through August 2013 for the four states included in the study region.

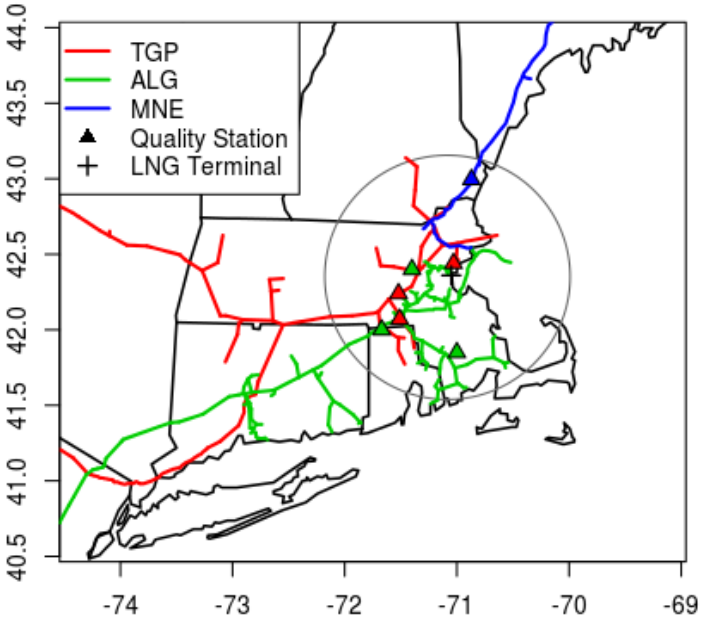

Figure 3-10. Approximate locations of the three interstate gas pipelines (Tennessee – TGP, Algonquin – ALG, and Maritimes and Northeast – MNE) (US EIA 2008) serving Boston and the surrounding area, the gas quality measurement stations used in this study, and the LNG import terminal. The gray circle is the study area boundary.

Natural gas consumption in electric power, residential, commercial, industrial, vehicle fuel, and pipeline and distribution use sectors (US EIA, 2014b), were all included in the consumption estimate because we were not able to distinguish emissions from individual sectors with the atmospheric data. Monthly and state consumption by the entire electric power sector and portions of the industrial and commercial sectors (17% and 6%, respectively) was spatially allocated to individual power production facilities based on each facility's monthly NG use (US EIA 2013-14, Figure 3-11). A small number of plants had missing values in 2013, which were filled according to each plant's relative consumption of the state, sector, and monthly total in 2012. Filled values accounted for 1.5% of the total consumption by power production facilities.

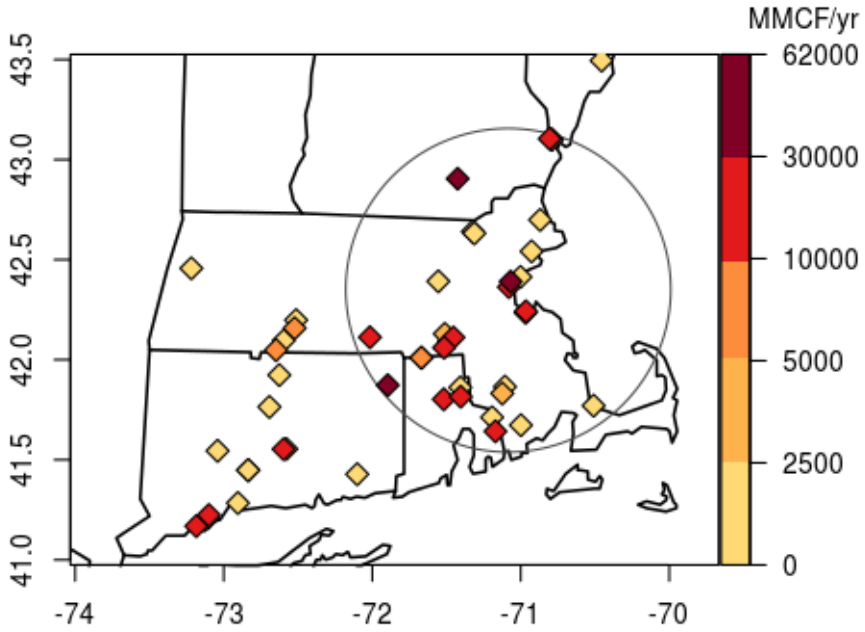

Figure 3-11. Location and gas consumption (units: 10^6 scf yr^{-1}) during the study year of each NG-fueled power plant (US EIA 2013-14) and CNG or LNG vehicle fueling station (US DOE 2014) in the four states included in the study area, delineated by the gray circle.

Consumption by the residential and commercial sectors (excluding the portion accounted for by individual electric power production facilities) was spatially allocated using a parcel-level

database for Massachusetts of residential and commercial building square footage and the fuel type used in each building for space and water heating (The Warren Group 2010). This dataset was constructed from multiple state and local government data sources such as Registry of Deeds, Land Court data, Town Clerk data and tax assessor information. Vehicle fuel consumption was spatially allocated equally among compressed natural gas (CNG) and LNG fueling station locations (US DOE 2014). Industrial sector consumption (excluding the portion accounted for by individual power production facilities) and pipeline and distribution use was spatially allocated using commercial building square footage data.

For the study area outside of Massachusetts, census data on the number of housing units with NG at the blockgroup scale (US Census Bureau 2012a) were used in place of the building square footage database, which was only available for Massachusetts. Within Massachusetts, the R^2 value for the 1 km^2 gridded census and square footage datasets was 0.8 for residential buildings and 0.7 for residential and commercial buildings together, demonstrating that the census dataset was a reasonable substitute for the square footage dataset where the former was not available. Figure 3-12 gives monthly average NG consumption by sector for Massachusetts and for the 90-km radius study area, as spatially allocated using the methods described above.

Uncertainty estimates for state monthly NG consumption are supplied by the US EIA (2012-13). Monthly standard errors for total consumption in Massachusetts are available for 6 of the 12 months in the study period, with NAs reported for the remaining months, and range from ± 0.4 to 1.1 %. Using the largest monthly standard error value, multiplying by 1.96 to estimate the 95% confidence interval, and summing them in quadrature, leads to 95% confidence interval estimates of ± 3.7 % for three-month seasonal totals and ± 7.4 % for the annual total. We did not estimate uncertainties in the spatial allocation of state total consumption to the study area, or

uncertainties in spatial distribution within the study area, because no independent dataset is available for comparison and because it is unknown how well the spatial distribution of consumption approximated the spatial distribution of emissions.

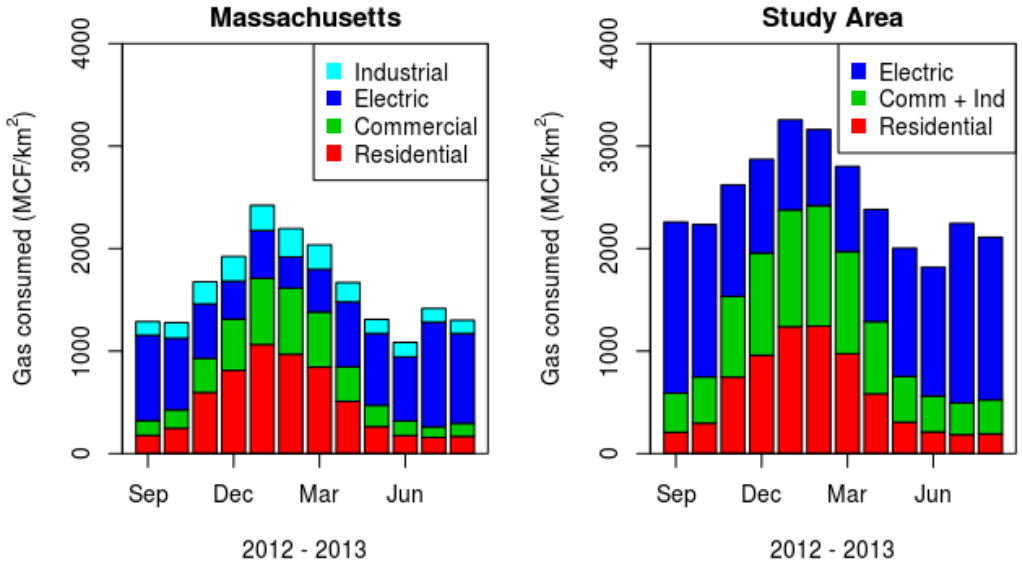

Figure 3-12. Average monthly NG consumption by sector in Massachusetts (US EIA 2014b) and the study area, spatially allocated using the methods described above. The "Ind & Other" category includes industrial, vehicle fuel, and pipeline and distribution use.

Optimization approach

The custom prior model of CH_4 emissions (Figure 3-8) was combined with WRF-STILT footprints to generate a set of simulated ΔCH_4 values for each hour at the two urban measurement stations. Means and 95% confidence intervals on all reported seasonal and annual CH_4 fluxes were generated through an end-to-end bootstrap analysis with the following steps. Background distributions were randomly sampled each day to calculate $\Delta CH_{4,obs}$. Average hourly afternoon (11–16 h EST, 16-21 h UTC) $CH_{4,obs}$ and $\Delta CH_{4,mod}$ values were randomly sampled separately for each day to generate average daily values of observed and modeled ΔCH_4 for the two urban sites. Daily average ΔCH_4 values were randomly sampled to generate seasonal

average ΔCH_4 (Figure 4-4). The emission inventory was scaled for each season to equalize mean afternoon modeled and observed ΔCH_4 for the two urban sites together, providing optimized CH_4 emission rates for the region. Daily afternoon data points with model-data residuals > 3σ of the residual distribution (< 5% of points for any individual site and season) were excluded from the emissions optimization calculation. Lastly, seasonal average ΔCH_4 and CH_4 emissions were randomly sampled to generate annual averages of each. Each of these steps was performed 1,000 times and means and confidence intervals were calculated from the resulting distributions.

Methane emissions in greater Boston

The mean annual optimized emission rate for the study area was 18.5 ± 3.7 g $CH_4 \cdot m^{-2} \cdot y^{-1}$ from all sources (Figure 3-13). Seasonal variations of total CH_4 emissions were modest, with fluxes in spring and summer marginally higher than in fall at the 95% confidence level (Figure 3-13).

Observation-model comparisons are shown in Figures 3-14 and 3-15. The over-prediction of nighttime CH_4 concentrations at BU, typically located below the nocturnal boundary layer, and the modest under-prediction of nighttime concentrations at COP (Figure 3-15), which was often above the nocturnal boundary layer is consistent with overestimated nocturnal low-level stability, possibly due to the low nocturnal temperature bias in WRF (Figure 3-7). The emissions estimate was derived from afternoon data only and thus was not affected by this model bias.

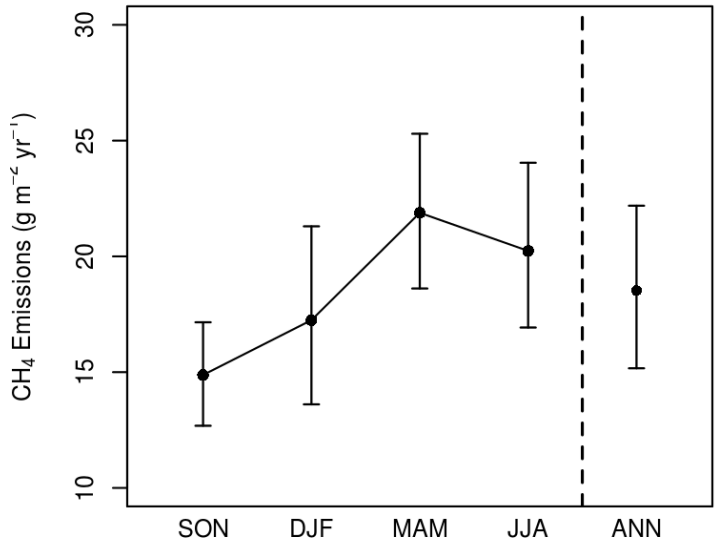

Figure 3-13. Seasonal and annual average (±95% confidence intervals) optimized CH_4 emissions in the Boston urban study region.

Sensitivity of emission results to modeling framework variants

The sensitivity of the emissions result was tested against several variants of the modeling framework (Figure 3-16). Hourly average values of ΔCH_4 were aggregated into daily points by taking afternoon (11-16 h EST) averages. This method of data aggregation was tested by averaging the four lowest hourly observations and model enhancements in the period of 9-18 h EST each day (Figure 3-3). Both of these approaches to data selection and aggregation aim to focus the analysis on periods when the atmosphere is well-mixed and when the data are less variable, which maximizes the areal representativeness of the results and minimizes the influence of a possible model biases in boundary layer height. Both aggregation methods yielded comparable results (Figure 3-16, pt 2).

Optimized emissions resulting from the use of EDGAR and the custom prior flux model at a coarser spatial resolution were not significantly different than the main result which used the custom emission inventory (Figure 3-16 pts. 3-4). We also tested the null hypothesis for spatial

variation of sources, using a model of uniform, constant flux over land and zero flux over water. This variant resulted in similar model-data correlations as the spatially-varying flux prior (Figure 3-13), but mean footprint-weighted, optimized emission fluxes were significantly different for the two sites. (The larger footprint from the COP site gave rise to smaller optimized fluxes). In contrast, results using our custom prior flux model yielded optimized fluxes that were statistically indistinguishable at the two sites (Figure 3-16, pts 6-7), despite the large differences in ΔCH_4 (Figure 3-4) and modeled footprints (Figure 3-1) between the two sites. Therefore, we rejected the null hypothesis of no significant spatial variation in emissions and adopted the custom prior flux model instead.

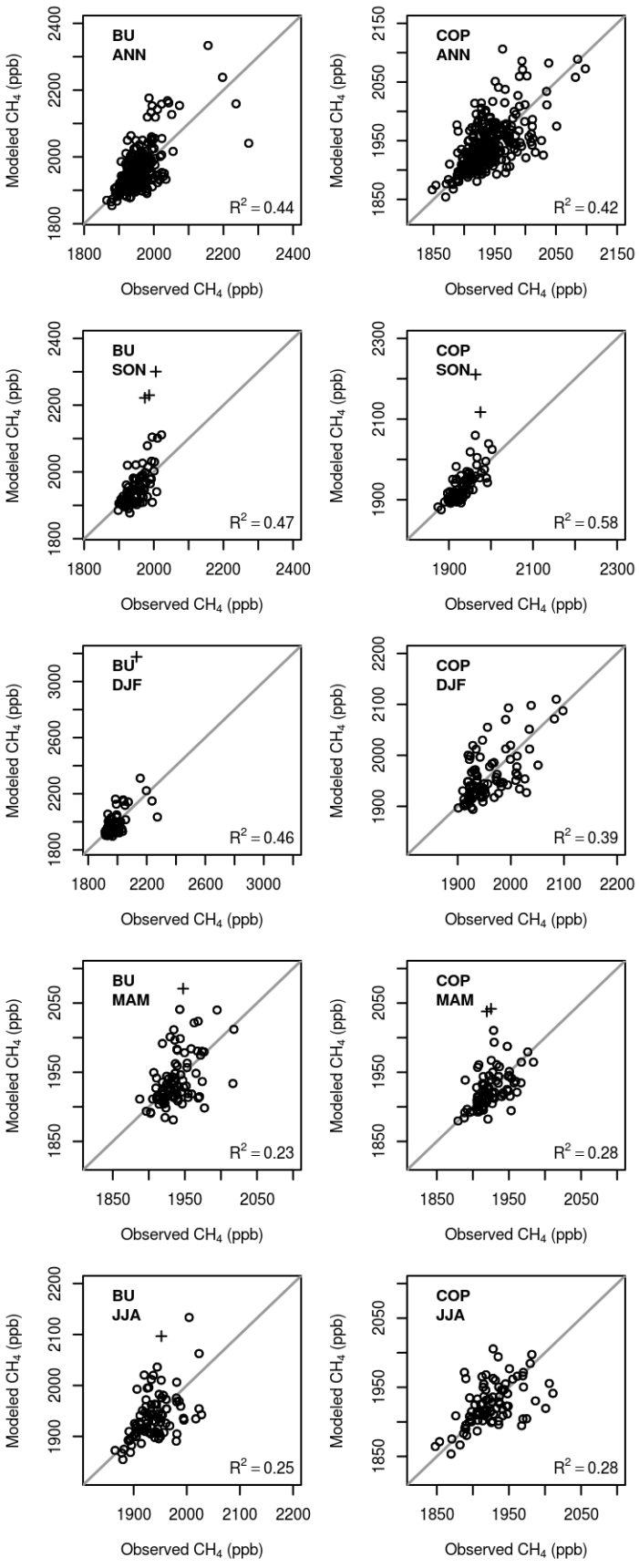

Figure 3-14. Optimized modeled versus observed daily average afternoon CH_4 concentrations for the two sites, one year, and four seasons. The gray line is the one-to- one line. Outlying points marked by crosses were excluded from model optimization.

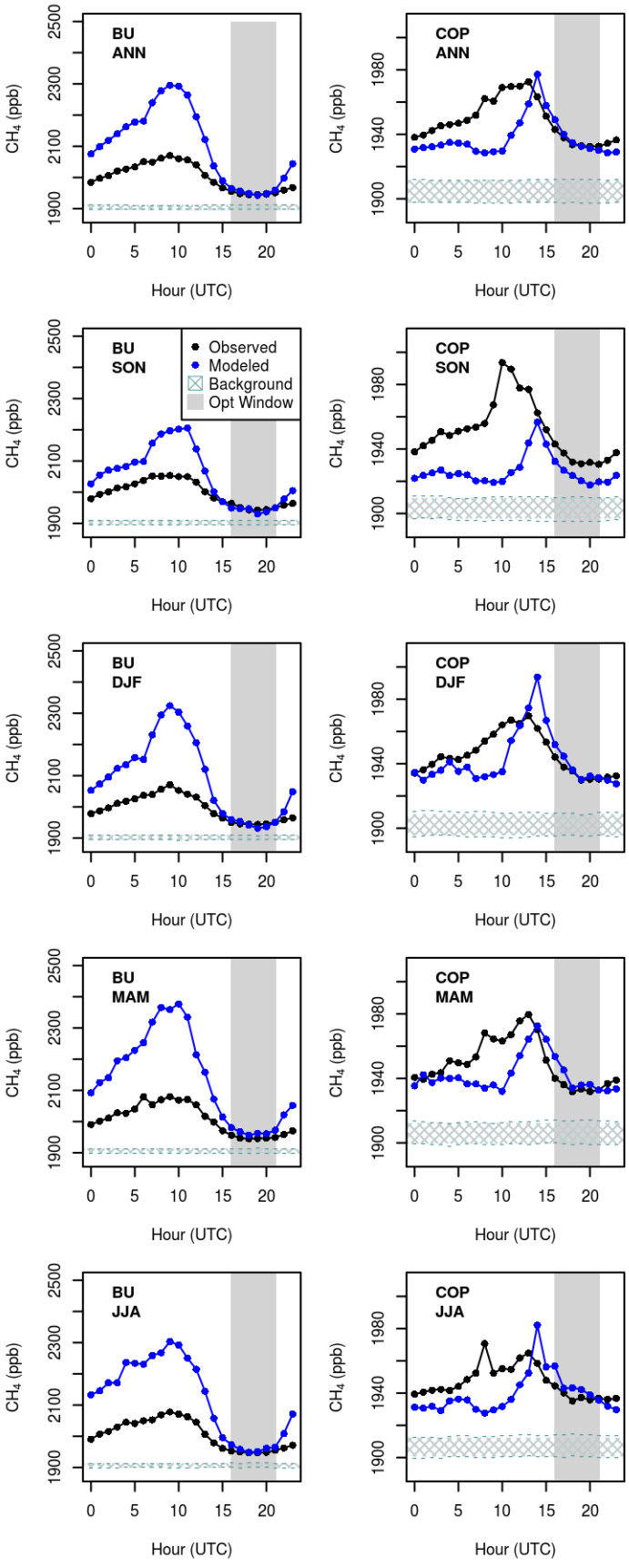

Figure 3-15. Observed, optimized modeled, and background CH_4 concentrations averaged by hour of the day for the two sites, one year, and four seasons. The horizontal hatched area shows the average range of sampled background concentrations, derived from 5-35th percentiles of the background station data. The gray vertical shaded area indicates the afternoon model optimization period, 11-16 h EST (16-21 h UTC). Although both high and low biases exist in the nighttime model data, modeled and observed data from the afternoon optimization window are in good agreement.

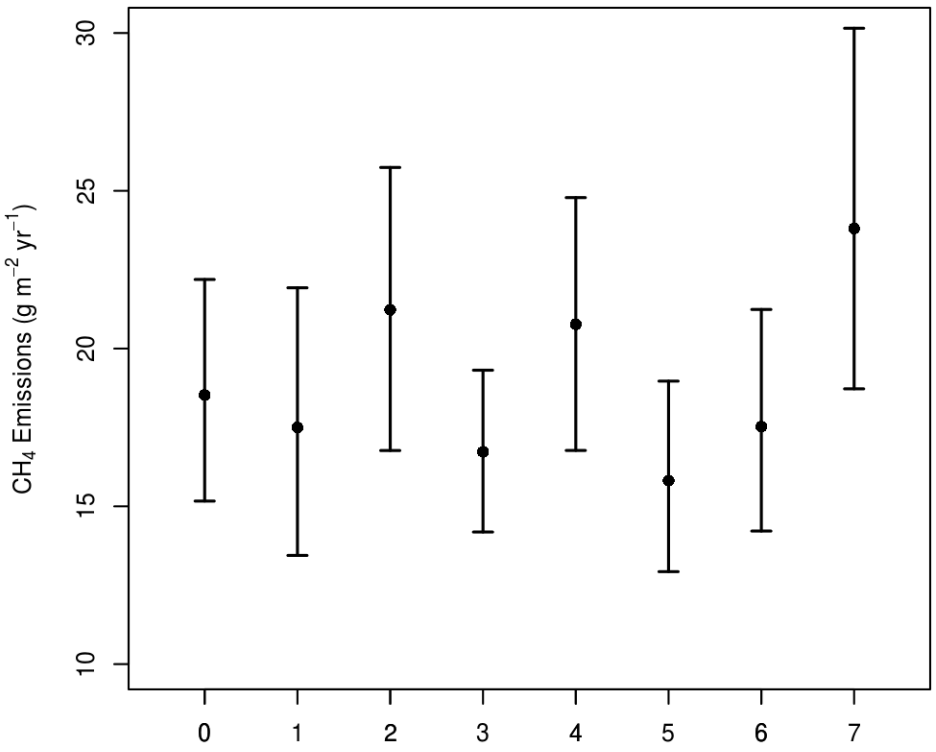

Figure 3-16. Mean annual emission results from the main configuration (point 0) and several variants of the modeling and analysis framework (points 1-7). The emission estimate presented in the main text (point 0) resulted from the custom emission inventory at 1 km^2 spatial resolution, data aggregation into daily afternoon (11-16 h EST) points, removal of extreme outliers, and from the analysis of both urban sites together. Point 1 shows the emission results when outliers were not removed. Point 2 shows the emission result from aggregating the four lowest hourly observed concentrations and model enhancements in the period of 9-18 h EST each day instead of afternoon hours (Figure 3-3). Point 3 shows the emission result from EDGAR instead of the custom emissions model. Point 4 shows the result when the custom emissions model was aggregated to a coarser spatial resolution. Point 5 shows the result when the NG emissions layer in the custom prior was scaled to contribute 80% of the total emissions (~2.2 times larger than in the main configuration), to be approximately consistent with the attribution results from ethane data (described in the next section). Points 6 and 7 show the results from the BU and COP sites analyzed separately.

Contribution of natural gas to methane emissions

To quantify the fraction of the observed ΔCH_4 and computed CH_4 emissions that was due to NG emissions, we compared ratios of C_2H_6 and CH_4 measured in the atmosphere and NG pipelines serving the region. Ethane is a significant component of NG, whereas microbial CH_4 sources, such as landfills, sewage, and wetlands, produce little or no C_2H_6 (Yacovitch et al. 2014). Because Boston has no geologic CH_4 seeps, no oil and gas production or refining, and

low rates of biomass burning, there are no known significant sources of C_2H_6 in the region other than NG.

Atmospheric ethane-methane ratio

Ethane concentrations were measured with a laser spectrometer (Yacovitch et al. 2014) at BU for three months in the fall and winter of 2012–13 and one month in the late spring of 2014 (Figure 3-17). To quantify the relationship between the atmospheric C_2H_6 and CH_4 measurements, we used χ^2 minimization (Press et al. 2002, Equation 3-1) of a straight-line fit (b=slope, a=intercept) to 5-minute medians of 1 hertz data points (Figure 3-18, x and y), with errors in each variable at each time point (i=1:N) characterized by the standard error of the mean (σ).

$$\chi^2(a,b) = \sum_{i=1}^{N} \frac{(y_i - a - bx_i)^2}{\sigma_{yi}^2 + b^2\sigma_{xi}^2} \quad (3\text{-}1)$$

Slopes from the χ^2 optimization were 10-15% larger than those obtained from an ordinary least squared regression because variance in the CH_4 measurements cannot be neglected.

For the 2012-13 period, data from afternoon (11-17 h EST) hours only were used, but for the 2014 period, data from all hours were used because the C_2H_6 signal-to-noise ratio was smaller for the spring measurements (Figure 3-17). We used daily fits to 5-minute intervals to calculate the average ratio in order to limit the influence of possible autocorrelation between points from individual hours or days. 95% confidence intervals were calculated by bootstrapping daily fit slopes with 1,000 iterations and sampling with replacement. The median of the daily slopes of atmospheric C_2H_6 versus CH_4 was 2.6 (2.5, 2.8) % during the cool season and 1.6 (1.4, 1.7) % during the warm season (Figure 3-18).

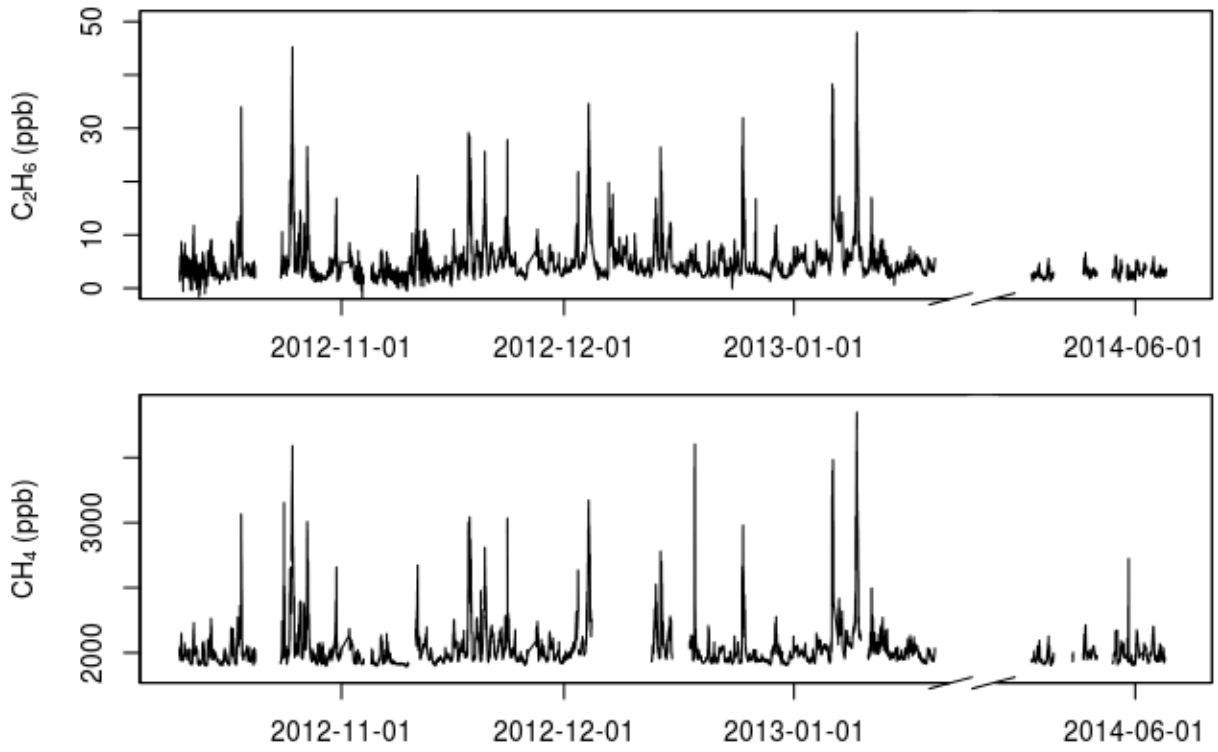

Figure 3-17. Five-minute median C_2H_6 and CH_4 measurements from BU.

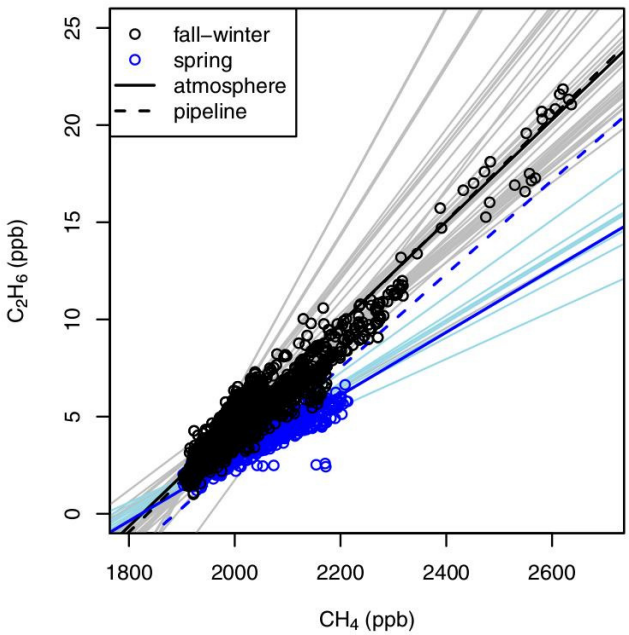

Figure 3-18. Five-minute median atmospheric C_2H_6 and CH_4 measurement points at BU in fall and winter of 2012–2013 (black) and spring of 2014 (blue), χ^2 optimization lines fit to each day (light lines), average fit lines for both seasons from all days with $R^2 > 0.75$ (bold solid lines), and lines with slopes of pipeline C_2H_6/CH_4 (dashed lines).

Quantification of covariance (slope of the regression line) between C_2H_6 and CH_4 measurements from each day using short (5-minute) intervals was adopted to eliminate any potential influence of building emissions and because C_2H_6 measurements were not available at the background stations. If background C_2H_6 measurements had been available, then quantification of the atmospheric C_2H_6 to CH_4 covariance using longer intervals, and optimization of C_2H_6 emissions in an inversion framework, may have been possible. The current framework assumes that background concentrations did not vary substantially during individual days, supported by the tight correlation between observed C_2H_6 and CH_4 on most days. Days with large shifts in wind direction sometimes did not have consistent C_2H_6/CH_4 and were rejected by a $R^2 > 0.75$ criterion (~50% of the days).

Results for the central C_2H_6/CH_4 values in the atmosphere by season were insensitive to our specific choices for treating and filtering the atmospheric data. Five-minute means instead of medians, a less stringent R^2 cutoff, and data from all hours instead of afternoon hours yielded both larger and smaller ratios that varied by < 10% and were not significantly different from the results reported above.

Pipeline ethane-methane ratio

Hourly gas quality data were collected from the informational postings of the three major pipeline companies that serve the region, Tennessee (TGP), Algonquin (ALG), and Maritimes and Northeast (MNE) (Figure 3-10, Tennessee Gas Pipeline Company 2014, Algonquin Gas Transmission LLC 2014). Daily median C_2H_6 and CH_4 ratios were calculated for each pipeline using hourly data (Figure 3-19) from the gas quality measurement stations closest to Boston (Figure 3-10). The three pipelines delivered the following fractions of NG consumed in Massachusetts in 2012: 65% TGP, 30% ALG, and 5% MNE (US EIA 2014a). Seasonal average

pipeline C_2H_6 and CH_4 ratios were calculated for the same time period as the atmospheric ratios using the daily median pipeline ratios, weighted by the fractional contributions of each pipeline. The average C_2H_6 and CH_4 ratio in the NG flowing into the region during the two atmospheric measurement periods was 2.7 ± 0.0% in the fall and winter of 2012–2013 and 2.4 ± 0.1% in the spring of 2014, (Figure 3-19). 95% confidence intervals were estimated by bootstrapping daily weighted median ratios with1,000 iterations and sampling with replacement.

Gas composition in the pipelines is measured using industry standard methods (Gas Processing Association 2013, ASTM 2010), but uncertainties due to sampling and measurement error are not reported. Furthermore, we have no way to estimate the relative sensitivity of the atmospheric measurements to the three pipelines and individual gas quality measurement locations, nor the representativeness of the measured relative to the lost gas. We tested the sensitivity of the computed seasonal average pipeline C_2H_6 and CH_4 ratios to assumptions about the relative contribution of the three pipelines by also calculating the pipeline ratio using equal contributions from TGP and ALG, and no contribution from MNE; the results were not significantly different than the ratios reported above. In general, our approach to estimate the mean pipeline C_2H_6 and CH_4 ratio was intended to yield an aggregate estimate that is robust to sporadic erroneous and/or unrepresentative measurements.

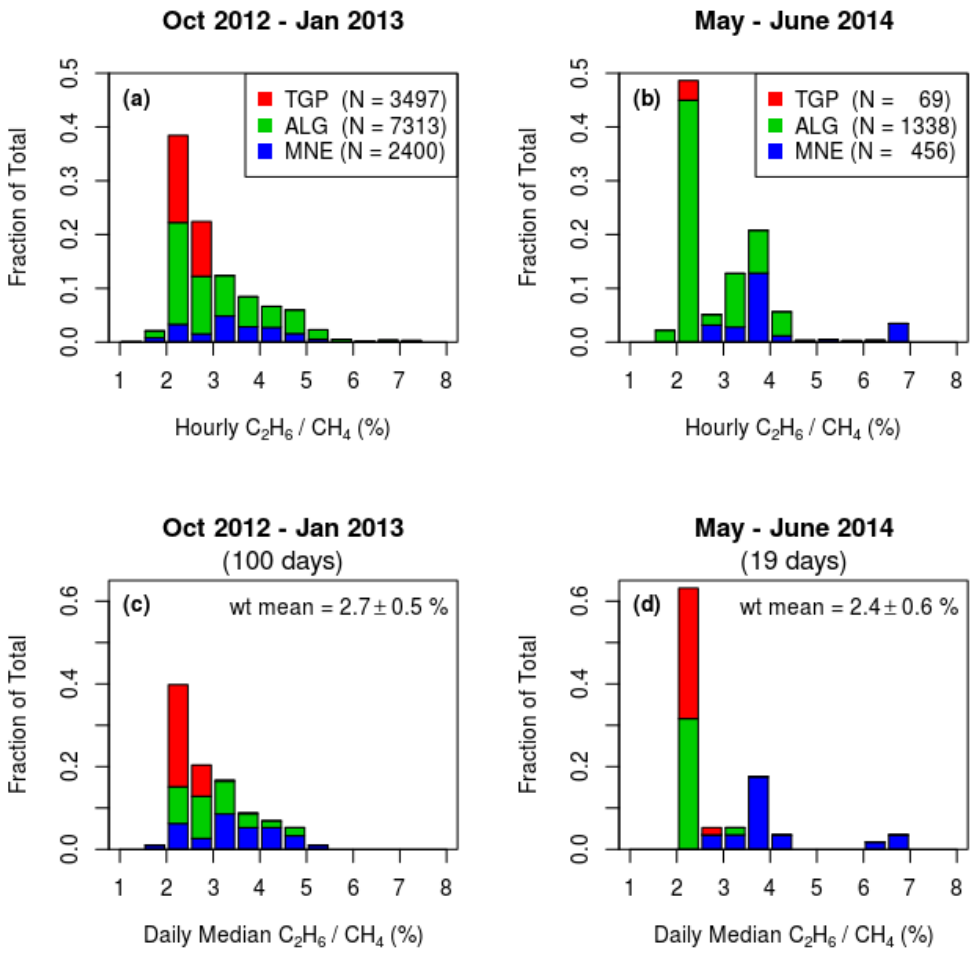

Figure 3-19. Stacked histograms of (ab) hourly and (cd) daily median ratios of C_2H_6 and CH_4 in the pipeline gas during the two time periods of the atmospheric C_2H_6 measurements (Figure- 3-17). (ab) Hourly data were obtained from the three pipelines (Tennessee – TGP, Algonquin – ALG, and Maritimes and Northeast – MNE) (Tennessee Gas Pipeline Company 2014, Algonquin Gas Transmission LLC 2014) for the stations shown in Figure 3-10. (cd) Daily median ratios for each pipeline were used to estimate a mean ratio for each of the two time periods, weighted by the volumes delivered by each pipeline to Massachusetts. Each of the three pipelines is equally represented in the daily median plots, but not the hourly plots because hourly data coverage varied between stations.

Attribution of total methane emissions to natural gas

The quotient of the C_2H_6 and CH_4 ratios in the atmosphere and pipeline demonstrates that NG contributed 98 (92, 105) and 67 (59, 72) % of the ΔCH_4 in Boston in the cool and warm seasons, respectively. We believe the relative contribution of NG to CH_4 emissions observed in the late spring of 2014 can be applied to the spring and summer months of the year prior because

the average air temperature and observed ΔCH_4 in May-June were very similar between 2013 and 2014 and because the observation interval approximates the midpoint of the March-August period for which we adopted the observed NG fraction. The weak seasonality of observed ΔCH_4 (Figure 3-4) and the CH_4 flux rate (Figure 3-13) is consistent with the finding that most of the emissions are from thermogenic gas, rather than biological processes, which would likely depend more strongly on season (van Hulzen et al. 1999, Spokas et al. 2011). The high correlation between atmospheric C_2H_6 and CH_4 (Figure 3-18), and the close correspondence of the atmospheric and pipeline gas ratios, support the finding that NG was the major source of enhancements for both gases.

Natural gas loss rate in greater Boston

The fraction of delivered NG that was emitted to the atmosphere was estimated by multiplying optimized emissions by the fractional contribution of NG to the atmospheric signal (Figure 3-20A), as indicated by the ethane tracer data, and dividing by the mean NG consumption in the study region (Figure 3-20B), as estimated through the spatial disaggregation of state-level data (Figure 3-9). The inferred mean annual NG loss rate in the study area was 2.7 ± 0.6% of the total delivered gas in 2012–2013, with little seasonal dependence (Fig. 3-20C). Uncertainties in the average loss rates were calculated by summing in quadrature the relative errors for the average emissions, atmospheric NG fraction, and NG consumption terms.

The modest seasonality of the inferred NG loss rate (Fig. 3-20C) is driven by the small seasonal variability in total NG consumption (Fig. 3-20B). Our analysis makes no assumptions about the relative contribution to emissions of specific NG-consuming sectors or emission processes, which could individually have very different loss rates than the aggregate estimate generated by this study. Our finding that the regional average NG emission rate was seasonally

invariant may indicate that it does not strongly depend on the seasonally varying components of the NG system, or could result from multiple compensating processes.

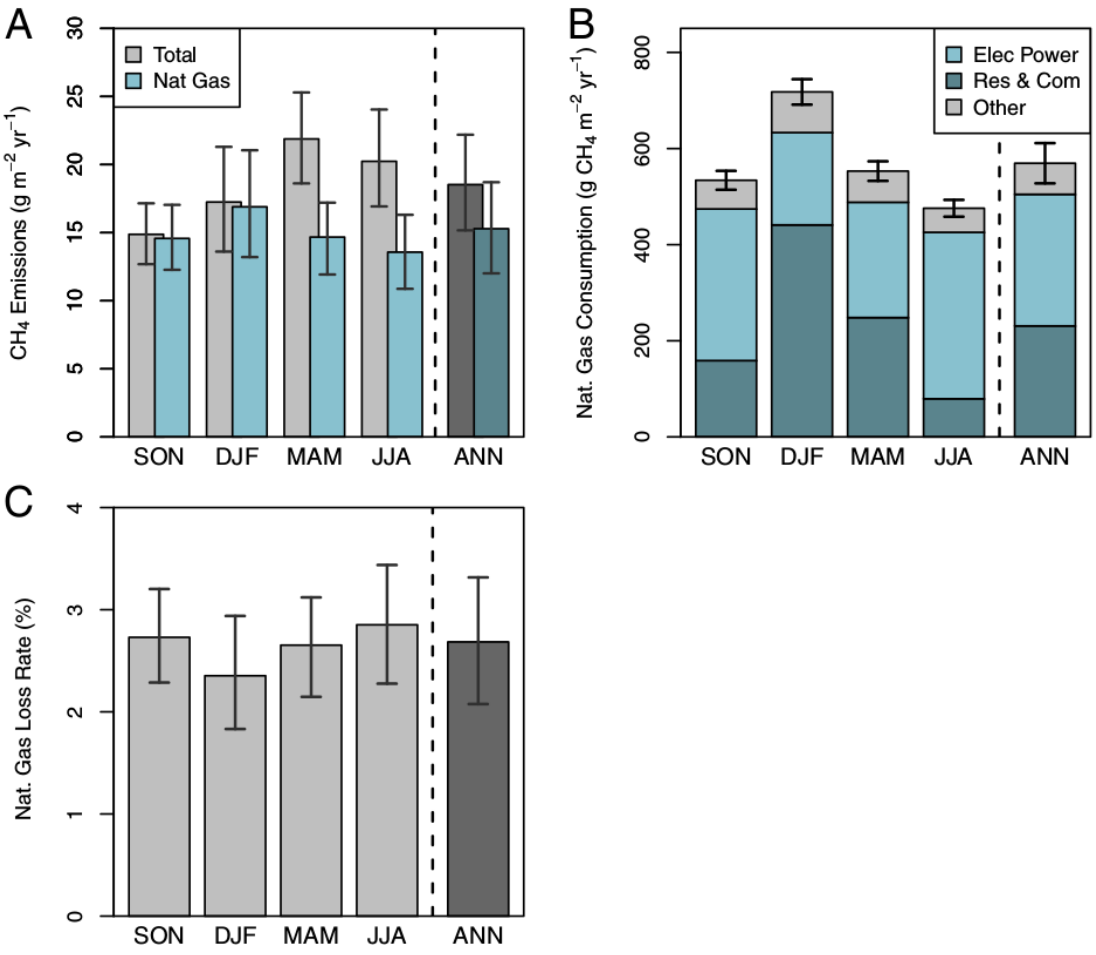

Figure 3-20. Seasonal and annual average (±95% confidence intervals) (A) optimized CH_4 emissions in total (Figure 3-13) and from NG, (B) NG consumption by sector, and (C) NG loss rates. (B) Consumption categories are electric power, residential and commercial, and other, which is comprised of industrial, vehicle fuel, and pipeline and distribution use (Figure 3-12).

Comparison with atmospheric studies and inventories

Two recent studies in Los Angeles covering ~2 months provide the only previous atmosphere-based ("top-down") estimates of emissions from NG in an urban area, 1–2% (0.7–3% when accounting for the error ranges) of total NG consumed in the basin (Wennberg et al.

2012, Peischl et al. 2013). However, attribution of CH_4 emissions to pipeline gas in Los Angeles is complicated by the presence of current and abandoned oil and gas wells, refinery operations, and natural CH_4 seeps, in addition to NG consumption. Other studies have estimated total CH_4 emission fluxes from a number of urban areas around the world (Table 3-1), using atmospheric data-model frameworks of varying sophistication, but have not quantitatively attributed fluxes to NG. Our value for total CH_4 emissions in Boston is at the low end of the overall range of fluxes reported for other urban areas (Table 3-1), suggesting that total CH_4 emission rates in Boston are not anomalous.

The US greenhouse gas (GHG) inventory (US EPA 2014c) attributes 3,302 Gg of CH_4 emissions to NG transmission, storage, and distribution in 2012, equal to ~0.7% of the NG delivered to consumers (US EIA 2014b). The key input data for NG distribution systems in the national inventory are emissions factors developed from industry measurements (US EPA/GRI 1996) and activity data on miles of pipeline by material and counts of metering and regulating stations, customer meters, and pipeline maintenance events and mishaps (US EPA 2014c). Emissions of NG in our study area are equal to ~8% of US emissions attributed to distribution, transport, and storage, and ~23% of national emissions from distribution alone, a notably higher fraction than the ~3% of US residential and commercial gas consumed in the study region. More detailed comparison of our results for the Boston urban region to the US GHG inventory is not possible because the inventory is not spatially disaggregated.

Massachusetts has compiled a state GHG inventory (MA DEP 2014a) (Table 3-3) using the same methods as the national inventory with state-level data, where available, and reports CH_4 emissions from NG systems equal to ~1.1% of NG consumed in the state. The larger loss fraction implied by the Massachusetts (~1.1%) versus the national (~0.7%) inventory is likely

due to larger proportions of cast iron and bare steel pipelines (US DOT 2014), which have higher emission factors (US EPA 2014c). Because most (68%) of our study region lies in Massachusetts, and most (88%) of the NG delivered in Massachusetts is consumed in the region, this value approximates the result that would be obtained by down-scaling the national inventory to the study region. Our result for the NG loss fraction is approximately two to three times larger than that implied by the state inventory (although no uncertainty range is reported for the latter).

NG companies also report their GHG emissions and NG losses to public agencies. Methane emission and NG delivery data reported to both the US EPA (2014a) and Massachusetts GHG Reporting Programs (MA DEP 2014b) show NG loss rates of 0.4–1.6% among individual NG distribution companies in Massachusetts in 2012 and 2013, with an average of 0.6%, weighted by delivered NG volumes. Data reported to the US EIA (2014a) for "losses from leaks, damage, accidents, migration and/or blow down" indicate loss rates of 0–1.1%, with a weighted average of 0.4%, among Massachusetts NG distribution companies in 2012 and 2013.

Policy analyses of NG distribution emissions (Cleveland 2012, Markey 2013) sometimes use reported quantities of "lost and unaccounted-for" (LAUF) gas, an accounting term and cost-recovery mechanism reported by utilities to public utility commissions. LAUF fractions reported by individual distribution companies in Massachusetts in 2012 and 2013 were 0–4.6%, with a weighted average of 2.7% (US DOT 2013). However, LAUF encompasses leaks, metering and accounting inaccuracies, and theft (Costello 2013), and hence the relationship between LAUF and NG emissions is unknown.

Deficiencies in existing estimates

Several possible reasons may explain why existing methodologies predict lower CH_4 emissions from NG than we observe in the Boston urban region.

i) Not all emission sources are inventoried. The US and Massachusetts inventories (US EPA 2014c, MA DEP 2014a) do not include NG losses occurring downstream of customer meters, neither at large industrial facilities, nor in residential and commercial settings.

ii) Leak surveys are not comprehensive. Leak surveys (e.g., Phillips et al. 2013, US Code of Federal Regulations 2013) are based on detection of discrete, highly elevated atmospheric signals, expressed at accessible locations. Numerous small leaks can occur without posing a safety hazard while still contributing significantly to the total CH_4 source, and would require sensitive and accurate measurements for detection and quantification. Some NG leaks may be emerging in locations that are difficult to access (e.g., indoors, on private property, through sewers or subway tunnels) with conventional surveys.

iii) Sampling protocols used to calculate emission factors have significant limitations. Due to practical constraints, NG emission factors are calculated from very small samples relative to the population they are intended to represent, and measurements are obtained from short-duration, non-repeated campaigns in a limited number of locations (US EPA/GRI 1996). These limitations can lead to under-sampling of infrequent, high-emission events (Brandt et al. 2014). Measurement of emissions from individual components requires access to restricted, privately owned facilities, which could lead to sample bias (Brandt et al. 2014), whether intentional or not. Inaccurate device and activity counts (Brandt et al. 2014), and incomplete understanding of controlling variables, may lead to inappropriate extrapolation of emission factors in space and

time. Data collected through new reporting requirements (US EPA 2014b) may help address some of these limitations for particular devices and processes.

These issues arise from our fundamental lack of knowledge about the specific sources and processes responsible for the discrepancies found in this and other studies (Brandt et al. 2014), and about the requirements for designing and testing a statistically rigorous accounting of emissions from the NG supply chain. Both high-emission events and diffuse low-emission sources need to be sampled continuously or repeatedly to gain understanding of the true distribution of NG emissions. In addition to emission data, improved quantification of the fractional NG loss rate requires the compilation and availability of more rigorous, standardized, and detailed data on NG flows. Datasets should be spatially explicit to facilitate collation of disparate datasets and analysis of specific areas. Closer cooperation in data sharing and synthesis and wide data dissemination are needed to better constrain CH_4 emissions from NG and to provide the information needed to reduce those emissions.

Significance of natural gas emissions

This study used one year of atmospheric CH_4 measurements from a network of observing stations, a high-resolution modeling framework, atmospheric measurements of C_2H_6, a tracer for NG emissions, and statistics on NG composition and consumption to quantify the NG emission rate for the Boston urban area as 2.7 ± 0.6% (95% confidence interval) of consumed NG, approximately two to three times higher than that given by the most applicable (state) GHG inventory. The total volume of emitted gas in the study area over one year was ~15 billion standard cubic feet (scf), valued conservatively at ~$90 million [using 2012 and 2013

Massachusetts city gate prices (US EIA 2014c)], equal to ~6 scf·person^{-1}·d^{-1} [using the study area population of ~7.2 million (US Census Bureau 2012b)].

The US President's Methane Strategy (The White House 2014) for reducing downstream NG emissions describes state and utility programs to accelerate infrastructure replacement, but offers no new federal initiatives for the distribution sector (US EPA OIG 2014). A new Massachusetts law (2014) is intended to improve the classification, reporting, and repair of NG leaks. The current study provides an example of a measurement-model framework that can be used to evaluate the effectiveness of programs aimed at reducing NG distribution emissions. More detailed measurements and accounting, following a more rigorous statistical design, are needed to fully characterize and prioritize the components, geographic areas, and supply chain sectors that are contributing the most emissions. The full environmental benefits of using NG in place of other fossil fuels will only be realized through active measures to decrease direct losses to the atmosphere, including in receiving areas such as the Boston urbanized region.

Acknowledgements

We thank Bruce Daube, Jasna Pittman, Bill Munger, Maryann Sargent, Elaine Gottlieb, Rachel Chang, Greg Santoni, Roisin Commane, Ben Lee, Brittain Briber, Ryan McGovern, and Tara Yacovitch, for help with the measurements; Jennifer Hegarty, Marikate Mountain, John Henderson, and the late Janusz Eluszkiewicz for their contributions to the WRF-STILT modeling; Conor Gately, Xiaojing Tang, and Robert Kaufmann for assisting with the customized emission inventory; George McNaughton, Deborah Warren, Brian Swett, and Joel Sparks for providing access to measurement sites; Robert Harriss, Steven Hamburg, Brian Lamb, Thomas Ferrara, Peter Huybers, Melissa Weitz, Mark de Figueiredo, Bill Irving, Sue Fleck, and Thomas Rogers, for helpful discussion; and the Barr Foundation for lending spectrometers. Funding for this study was provided by the TomKat Charitable Trust via the Harvard School of Engineering and Applied Science Dean's Innovation Fund, Boston University College of the Arts and Sciences, the National Science Foundation through Major Research Instrumentation Award 1337512 and Collaborative Research Awards 1265614, 1302902, and 0948819; the National Aeronautics and Space Administration through the Earth and Space Science Graduate Research Fellowship NNX14AK87H, Interdisciplinary Science Award NNX12AM82G, Carbon Monitoring System Award NNH13CK02C, and Carbon Cycle Science Award NNX11AG47G; and Environmental Defense Fund (EDF) Award 0146-10100. Funding for EDF's methane research series was provided by Fiona and Stan Druckenmiller, the Heising–Simons Foundation, Bill and Susan Oberndorf, Betsy and Sam Reeves, the Robertson Foundation, the Alfred P. Sloan Foundation, the TomKat Charitable Trust, and The Walton Family Foundation.

References

Algonquin Gas Transmission, LLC (2014) Link System Informational Postings, Gas Quality, Hourly Chromatograph Postings (Spectra Energy, Houston TX). Available at infopost.spectraenergy.com/infopost. Accessed July 9, 2014.

ASTM International (2010) Standard test method for analysis of natural gas by gas chromatography, ASTM D1945, www.astm.org/Standards/D1945.htm.

Blake DR, Woo VH, Tyler SC, Rowland FS (1984) Methane concentrations and source strengths in urban locations, Geophysical Research Letters, 11 (12) :1211–1214.

Brandt AR, Heath GA, Kort EA, O'Sullivan F, Petron G, Jordaan SM, Tans P, Wilcox J, Gopstein AM, Arent D, Wofsy S, Brown NJ, Bradley R, Stucky GD, Eardley D, Harriss R (2014) Energy and environment. Methane leaks from North American natural gas systems, Science, 343 (6172): 733–735.

Bridgham SD, Megonigal JP, Keller JK, Bliss NB, Trettin C (2007) Wetlands – Supplemental Materials. The First State of the Carbon Cycle Report (SOCCR): The North American Carbon Budget and Implications for the Global Carbon Cycle. A Report by the U.S. Climate Change Science Program and the Subcommittee on Global Change Research, eds AW King, et al., pp 177-192, http://cdiac.ornl.gov/SOCCR.

Ciais P, Sabine C, Bala G, Bopp L, Brovkin V, Canadell J, Chhabra A, DeFries R, Galloway J, Heimann M, Jones C, Le Quéré C, Myneni RB, Piao S, Thornton P (2013) Carbon and other biogeochemical cycles. Climate Change 2013: The Physical Science Basis. Contribution of Working Group I to the Fifth Assessment Report of the Intergovernmental Panel on Climate Change, eds Stocker TF, Qin D, Plattner G-K, Tignor M, Allen SK, Boschung J, Nauels A, Xia Y, Bex V, Midgley PM (Cambridge University Press, Cambridge, United Kingdom and New York, NY, USA), pp 465–570.

Cleveland S (2012) Into Thin Air (Conservation Law Foundation). Available at www.clf.org/static/natural-gas-leaks/WhitePaper_Final_lowres.pdf. Accessed February 28, 2013.

Costello K (2013) Lost and Unaccounted-for Gas: Practices of State Utility Commissions (National Regulatory Research Institute, Silver Spring, MD) Report No. 13-16.

European Commission, Joint Research Centre (JRC)/Netherlands Environmental Assessment Agency (PBL) (2013) Emission Database for Global Atmospheric Research (EDGAR), release version 4.2 FT2010, edgar.jrc.ec.europa.eu

Federal Highway Administration (2012), Highway Statistics Series, Highway Statistics 2012, Table VM-4, www.fhwa.dot.gov/policyinformation/statistics/2012.

Fiore AM, Jacob DJ, Field BD, Streets DG, Fernandes SD (2002) Linking ozone pollution and climate change: The case for controlling methane, Geophysical Research Letters, 29 (19): 25-1–25-4.

Fowler D, Hargreaves KJ, Choularton TW, Gallagher M, Simpxon T, Kaye A (1996) Measurements of regional CH_4 emissions in the UK using boundary layer budget methods. Energy Conversion and Management, 37: 769-775.

Gas Processing Association (2013) Analysis for natural gas and similar gaseous mixtures by gas chromatography, GPA 2261,www.gpaglobal.org/publications/view/id/3583.

Gately CK, Hutyra LR, Wing IS, Brondfield MN (2013) A bottom up approach to on-road CO_2 emissions estimates: improved spatial accuracy and applications for regional planning, Environmental Science and Technology, 47: 2423-2430.

Gioli B, Toscano P, Lugato E, Matese A, Miglietta F, Zaldei A, Vaccari FP (2012) Methane and carbon dioxide fluxes and source partitioning in urban areas: the case study of Florence, Italy, Environmental Pollution, 164: 125-131.

Hsu YK, VanCuren T, Park S, Jakober C, Herner J, FitzGibbon M, Blake DR, Parrish DD (2010) Methane emissions inventory verification in southern California, Atmospheric Environment, 44: 1–7.

Kuc T, Rozanski K, Zimnoch M, Necki JM, Korus A (2003) Anthropogenic emissions of CO_2 and CH_4 in an urban environment, Applied Energy, 75: 193-2003.

Lamb BK, McManus JB, Shorter JH, Kolb CE, Mosher B, Harriss RC, Allwine E, Blaha D, Howard T, Guenther A, Lott RA, Siverson R, Westburg H, Zimmerman P (1995) Development of atmospheric tracer methods to measure methane emissions from natural gas facilities and urban areas, Environmental Science and Technology, 29: 1468-1479.

Levin I, Glatzel-Mattheier H, Marik T, Cuntz M, Schmidt M, Worthy DE (1999) Verification of German methane emission inventories and their recent changes based on atmospheric observations, Journal of Geophysical Research, 104 (D3): 3447-3456.

Lin JC, Gerbic C, Wofsy SC, Andrews AE, Daube BC, Davis KJ, Grainger CA (2003) A near-field tool or simulating the upstream influence of atmospheric observations: The Stochastic Time-Inverted Lagrangian Transport (STILT) model, Journal of Geophysical Research, 108: 4493–4510.

Markey EJ (2013) America Pays for Gas Leaks. A Report Prepared for Senator Markey by the House Natural Resources Committee Democratic Staff and Senator Markey's Staff. Available at www.markey.senate.gov/documents/markey_lost_gas_report.pdf. Accessed August 7, 2013.

Massachusetts Department of Environmental Protection (2014a) Massachusetts Annual Greenhouse Gas Emissions Inventory: 1990 through 2011, with Partial 2012 Data. Available at www.mass.gov/eea/docs/dep/air/climate/maghginv.xls. Accessed December 27, 2014.

Massachusetts Department of Environmental Protection (2014b) MassDEP GHG Reporting Program Summary Report and Facility List, Emissions Year 2012 and 2013. Available at www.mass.gov/eea/agencies/massdep/climate-energy/climate/approvals/ma-greenhousegas-emissions-reporting-program.html. Accessed December 26, 2014.

Massachusetts Laws (2014) An Act Relative to Natural Gas Leaks. Available at malegislature.gov/Laws/SessionLaws/Acts/2014/Chapter149. Accessed June 27, 2014.

Mays KL, Shepson PB, Stirm BH, Karion A, Sweeney C, Gurney KR (2009) Aircraft-based measurements of the carbon footprint of Indianapolis, Environmental Science and Technology, 43: 7816-7823.

Mesinger F, DiMego G, Kalanay E, Mitchell K, Shafran PC, Ebisuzaki W, Jovic D, Woollen J, Rogers E, Berbery EH, Ek MB, Fan Y, Grubine R, Higgins W, Li H, Lin Y, Mankin G, Parrish D, Shi W (2006) North American regional reanalysis, Bulletin of the American Meteorological Society, 87 (3): 343-360.

Moriizumi J, NagamineK , Iida T, Ikebe Y (1996) Methane in an urban area of Nagoya, Japan, inferred from atmospheric radon-222 data, Atmospheric Environment, 30: 1543-1549.

Myhre G, Shindell D, Bréon F-M, Collins W, Fuglestvedt J, Huang J, Koch D, Lamarque J-F, Lee D, Mendoza B, Nakajima T, Robock A, Stephens G, Takemura T, Zhang H (2013) Anthropogenic and natural radiative forcing. Climate Change 2013: The Physical Science Basis. Contribution of Working Group I to the Fifth Assessment Report of the Intergovernmental Panel on Climate Change, eds Stocker TF, Qin D, Plattner G-K, Tignor M, Allen SK, Boschung J, Nauels A, Xia Y, Bex V, Midgley PM (Cambridge University Press, Cambridge, United Kingdom and New York, NY, USA), pp 659–740.

National Center for Atmospheric Research, Developmental Testbed Center (2013) Model Evaluation Tools, v4.1, www.dtcenter.org/met/users.

National Centers for Environmental Prediction/National Weather Service/NOAA/U.S. Department of Commerce (2004) NCEP ADP Global Surface Observational Weather Data, October 1999 – continuing, Research Data Archive at the National Center for Atmospheric Research, Computational and Information Systems Laboratory, http://rda.ucar.edu/datasets/ds461.0/

Nehrkorn T, Eluszkiewicz J, Wofsy SC, Lin JC, Gerbig C, Marcos L, Freitas S (2010) Coupled weather research and forecasting-stochastic time inverted Lagrangian transport (WRF-STILT) model, Meteorology and Atmospheric Physics, 107: 51–64.

Nehrkorn T, Henderson J, Leidner M, Mountain M, Eluszkiewicz J, McKain K, Wofsy S (2013) WRF simulations of the urban circulation in the Salt Lake City area for CO_2 modeling, Journal of Applied Meteorology and Climatology, 52: 323-340.

O'Shea SJ, Allen G, Fleming ZL, Bauguitte SJB, Percival CJ, Gallagher MW, Lee J, Helfter C, Nemitz E (2014) Area fluxes of carbon dioxide, methane, and carbon monoxide derived from airborne measurements around Greater London: A case study during summer 2012, Journal of Geophysical Research, 119 (8): 4940-4952.

Peischl J, Ryerson TB, Brioude J, Aikin KC, Andrews AE, Atlas E, Blake D, Daube BC, de Gouwhel JA, Dlugokencky E, Frost GJ, Gentner DR, Gilman JB, Goldstein AH, Harley RA, Holloway JS, Kofler J, Kuster WC, Lang PM, Novelli PC, Santoni GW, Trainer M, Wofsy SC, Parrish DD (2013) Quantifying sources of methane using light alkanes in the Los Angeles basin, California, Journal of Geophysical Research – Atmospheres, 118: 1–17.

Phillips NG, Ackley R, Crosson ER, Down A, Hutyra LR, Bronfield M, Karr JD, Zhao K, Jackson RB (2013) Mapping urban pipeline leaks: Methane leaks across Boston, Environmental Pollution, 173: 1–4.

Press WH, Teukolsky SA, Vetterling WT, Flannery BP (2002) Modeling of data. Numerical Recipes in FORTRAN: The Art of Scientific Computing (Cambridge University Press, New York, NY, USA), 2nd Ed, Chap 15.

Santoni GW (2013) Fluxes of atmospheric methane using novel instruments, field measurements, and inverse modeling, PhD thesis (Harvard University, Cambridge, MA, USA).

Shorter JH, McManus JB, Kolb CE, Allwine EJ, Lamb BK, Mosher BW, Harriss RC, Partchatka U, Fischer H, Harris GW, Crutzen PJ, Karbach HJ (1996) Methane emission measurements in urban areas in eastern Germany, Journal of Atmospheric Chemistry, 24: 121-140.

Skamarock WC, Klemp JB (2008) A time-split nonhydrostatic atmospheric model for weather research and forecasting applications, Journal of Computational Physics, 227: 3465-3485.

Spokas K, Bogner J, Chanton J (2011) A process-based inventory model for landfill CH_4 emissions inclusive of seasonal soil microclimate and CH_4 oxidation, Journal of Geophysical Research: Biogeosciences, 116: G04017.

Su F, Shao M, Cai X, Zeng L, Zhu T (2003) Estimates of methane emissions in Beijing using a backward trajectory inversion model, Chemical Speciation and Bioavailability, 14: 43-48.

Tennessee Gas Pipeline Company, LLC (2014) Informational Postings, Gas Quality, Hourly Gas Quality Data (Kinder Morgan, Houston, TX). Available at webapps.elpaso. com/PortalUI/DefaultKM.aspx?TSP=TGPD. Accessed November 28, 2012 through July 9, 2014.

US Census Bureau (2012a) 2010 American Community Survey 5-Year Estimates. Available at www.census.gov. Accessed September 30, 2013.

US Census Bureau (2012b) 2010 Decennial Census. Available at www.census.gov. Accessed June 25, 2014.

US Code of Federal Regulations (2013) Title 49, Subtitle B, Chapter 1, Subchapter D, Part 192, Section 192.723, Distribution systems: Leakage surveys. Available at www.gpo.gov/fdsys/pkg/CFR-2013-title49-vol3/xml/CFR-2013-title49-vol3-sec192-723.xml.

US Department of Agriculture (2009), 2007 Census of Agriculture, www.agcensus.usda.gov.

US Department of Energy (2014) Alternative Fuel Station Locator, www.afdc.energy.gov/locator/stations.

US Department of Transportation, Pipeline and Hazardous Materials Safety Administration (2013) Distribution Annual Data. Available at www.phmsa.dot.gov/staticfiles/PHMSA/DownloadableFiles/Pipeline2data/annual_gas_distribution_2013.zip. Accessed December 27, 2014.

US Department of Transportation, Pipeline Hazardous Materials Safety Administration (2014) Pipeline Replacement Updates. Available at opsweb.phmsa.dot.gov/pipeline_replacement. Accessed December 27, 2014.

US Energy Information Administration (2008), www.eia.gov/maps/map_data/EIA_NaturalGas_InterIntrastate_Pipelines_US.zip.

US Energy Information Administration (2012-2013) Natural Gas Monthly, Table C1, Standard Error for Natural Gas Deliveries and Price by Consumers, by State, www.eia.gov/naturalgas/monthly/archive.

US Energy Information Administration (2013-2014) 2012 and 2013 Annual Electric Utility Data, Form EIA-923, www.eia.gov/electricity/data/eia923

US Energy Information Administration (2014a) Natural Gas Annual Respondent Query System, Annual Report on Natural and Supplemental Gas Supply and Disposition. Available at www.eia.gov/cfapps/ngqs/ngqs.cfm?f_report=RP1. Accessed December 26, 2014.

US Energy Information Administration (2014b) Natural Gas Consumption by End Use. Available at www.eia.gov/dnav/ng/ng_cons_sum_dcu_nus_a.htm. Accessed December 26, 2014.

US Energy Information Administration (2014c) Natural Gas Prices. Available at www.eia.gov/dnav/ng/ng_pri_sum_dcu_nus_a.htm. Accessed December 27, 2014.

US Environmental Protection Agency/Gas Research Institute (1996) Methane Emissions from the Natural Gas Industry, eds Harrison M, Shires T, Wessels J, Cowgill R (Radian International LLC for National Risk Management Research Laboratory, Research Triangle Park, NC, USA).

US Environmental Protection Agency (1998) AP 42, 5th edition, volume 1, Compilation of Air Pollutant Emission Factors, Chapter 14, Greenhouse Gas Biogenic Sources, Section 4, Enteric Fermentation, www.epa.gov/ttn/chief/ap42/ch14/index.html.

US Environmental Protection Agency (2008) Greenhouse Gas Inventory Protocol Core Module Guidance – Direct Emissions from Mobile Combustion Sources, EPA Climate Leaders, Tables 3, A-6, and A-7.

US Environmental Protection Agency, Office of Inspector General (2014) Improvements Needed in EPA Efforts to Address Methane Emissions From Natural Gas Distribution Pipelines, Report No. 14-P-0324. Available at www.epa.gov/oig/reports/2014/20140729-14-P-0325.pdf. Accessed July 28, 2014.

US Environmental Protection Agency (2014a) 2012 and 2013 Greenhouse Gas Emissions from Large Facilities. Available at ghgdata.epa.gov/ghgp. Accessed December 26, 2014.

US Environmental Protection Agency (2014b) Greenhouse Gas Reporting Program, Subpart W, Petroleum and Natural Gas Systems Subpart W Rulemaking Resources. Available at www.epa.gov/ghgreporting/reporters/subpart/w-regdocs.html. Accessed December 27, 2014.

US Environmental Protection Agency (2014c) Inventory of U.S. Greenhouse Gas Emissions and Sinks: 1990–2012, EPA-430-R-14-003. Available at www.epa.gov/climatechange/ghgemissions/usinventoryreport.html. Accessed June 1, 2014.

US Fish and Wildlife Service (2013) National Wetlands Inventory, www.fws.gov/wetlands.

Van Hulzen JB, Segers R, van Bodegom PM, Leffelaar PA (1999) Temperature effects on soil methane production: An explanation for observed variability, Soil Biology and Biochemistry, 31 (14): 1919–1926.

The Warren Group, Inc. (2010) Boston, MA, www.thewarrengroup.com.

Wecht KJ, Jacob DJ, Sulprizio MP, Santoni GW, Wofsy SC, Parker R, Bosch H, Worden J (2014) Spatially resolving methane emissions in California: constraints from CalNex aircraft campaign and from present (GOSAT, TES) and future (TROPOMI, geostationary) satellite observations, Atmospheric Chemistry and Physics, 14: 8173-8184.

Wennberg PO, Mui W, Wunch D, Kort EA, Blake DR, Atlas EL, Santoni GW, Wofsy SC, Diskin GS, Jeong S, Fischer ML (2012) On the sources of methane to the Los Angeles atmosphere, Environmental Science and Technology, 46 (17): 9282–9289.

West JJ, Fiore AM, Horowitz LW, Mauzerall DL (2006) Global health benefits of mitigating ozone pollution with methane emission controls, Proceedings of the National Academy of Sciences of the United States of America, 103 (11): 3988–3993.

The White House (2014) Climate Action Plan: Strategy to Reduce Methane Emissions. Available at www.whitehouse.gov/sites/default/files/strategy_to_reduce_methane_emissions_2014-03-28_final.pdf. Accessed March 28, 2014.

Wunch D, Wennberg PO, Toon GC, Keppel-Aleks G, Yavin YG (2009) Emissions of greenhouse gases from a North American megacity, Geophysical Research Letters, 36 :L15810.

Yacovitch TI, Herndon SC, Roscioli JR, Floerchinger C, McGovern RM, Agnese M, Petron G, Kofler J, Sweeney C, Karion A, Conley SA, Kort EA, Nahle L, Fischer M, Hildebrandt L, Koeth J, McManus JB, Nelson DD, Zahniser MS, Kolb CE (2014) Demonstration of an ethane spectrometer for methane source identification, Environmental Science and Technology, 48 (14): 8028–8034.

Zinchenko AV, Paramonova NN, Privalov VI, Reshetnikov AI (2002) Estimation of methane emissions in the St. Petersburg, Russia, region: An atmospheric nocturnal boundary layer budget approach, Journal of Geophysical Research, 107: 4416.